Radar Studies of Small-Scale E-Region Plasma Irregularities

Thesis submitted for the degree of
Doctor of Philosophy
at the University of Leicester

Paul Eglitis
Department of Physics and Astronomy
University of Leicester

February 1994

ProQuest LLC
789 East Eisenhower Parkway
P.O. Box 1346
Ann Arbor, MI 48106-1346

Dedicated to Mum, Dad, Helen and Aunty Cath.

RADAR STUDIES OF SMALL-SCALE E-REGION PLASMA IRREGULARITIES

Paul Eglitis

ABSTRACT

Coherent scatter radars are extensively employed in the study of important geophysical processes in the Earth's upper atmosphere and magnetosphere. The science relies on the ability of coherent scatter radars to detect plasma irregularities in the Earth's ionosphere and relate their properties to the geophysical process under consideration. This thesis is concerned with the physical characteristics of the plasma irregularities deduced from coherent scatter radar observations. Data from three coherent scatter radar systems, PACE, SABRE and COSCAT, each sensitive to a different irregularity wavelength, are analysed. Statistics for the backscatter power, phase speed and spectral width at each wavelength are calculated and compared. Furthermore, the functional dependence of the irregularity parameters on each other has been investigated. Strong relationships between the spectral width and irregularity phase speed and the spectral width and backscatter power are identified. The spectral widths tend to exhibit a minimum at phase speeds close to the ion-acoustic speed. There is a decrease in the average backscatter power as the spectral width increases. A new measurement of the dependence of the spectral width on the irregularity wave number is deduced. These results have important significance for the general interpretation of coherent scatter radar measurements.

Special experimental campaigns with SABRE and COSCAT in conjunction with EISCAT have been undertaken to enable the irregularity phase speed and the plasma drift speed to be compared. This is a very important relationship since the plasma drift speed is routinely estimated from the irregularity phase speed. The analysis confirms the non-linear behaviour of the relationship between these two parameters. Similar results are obtained for COSCAT and SABRE. Differences can be attributed to the expected variations with wave number and to variations in the height of the observed irregularities, consistent with the kinetic theory of Robinson and Honary (1990).

Acknowledgements

For making this thesis possible and for sustaining me throughout its construction thanks are given to:

Professor Tudor Jones for his stewardship as head of the Ionospheric Physics Group and his constructive remarks regarding the final manuscript.

Dr. Terry Robinson for his supervision and an eternal supply of good suggestions.

Dr. Alan Rodger for his supervision and asking me the most pertinent questions.

British Antarctic Survey (BAS) for results from the PACE radar.

For their geophysical knowledge Dr. Mark Lester and Dr. Tim Yeoman.

A plethora of scientists for their helpful discussions; Dr. Ian McCrea for COSCAT and ion-energy balance, Nick Mattin for PACE data and irregularities, Dr. Mike Pinnock for spectral widths and radar systems.

Nigel Wade, Dr. Chris Thomas, Andrew 'Grit' Stone, Alistair Kershaw and Mehbub Ashraf for help with computing of all types.

Generations of the workshop for building radars, their wry observations, wit and encouragement; Peter Chapman, Warren Smith, Mick Parsons, Stuart Crooks, Lynda Forsyth and Martin Hollingshead.

Everyone else who I had the fortune to work with or just know in the ionospheric physics group, including: Martin Popple (irrepressible), Paul Rylah (space), Dr. Alan Stocker (samosas), Dr. Farideh Honary (kinetic chocolate), Dr. Bob Cherry (think about the future), Dr. Eric Bradshaw (lungs on legs), Dr. Stuart Kelly (*space*), Steve Milan (maximum information in minimum space) Jackie Davies (EISCAT help), John Taylor (cultural pipeline), Dr. Awni Abdulahad (unstoppable), Julian Thornhill (digital guru), Kathleen (all those fiddly forms), Dr. Thomas Smid for always opening ones mind from a new side, countless denizens of RSL (once RPL never forgotten), the new vanguard: Brian Shand(man), Mark II Ransom, Dr. Richard 'Mongoose' Beard, Dr. Neil 'The Terminator' Arnold, Zou Li, Darren Wright and all those to come.....

The SERC who funded this work with a CASE research studentship in collaboration with BAS (NERC), the Max Planck Institut für Aeronomie and Uppsala ionospheric Observatory for the operation of the Swedish radar of SABRE, Dr. K. Schlegel and Dr. T. Nygrén for their collaboration in the COSCAT experiment and the EISCAT scientific association for EISCAT.

TABLE OF CONTENTS

Chapter One

INTRODUCTION

An important consequence of the impact of the sun's radiation on the Earth's atmosphere is the ionisation of neutral gas particles. Between altitudes of 60 and 600km the ionisation is of sufficient magnitude that the plasma density has a strong effect on the propagation of radio waves, e.g. Budden (1966). This region is called the ionosphere. The physics of the ionosphere has been studied for the greater part of this century. Basic texts on the subject include Rishbeth and Garriott (1969) and Ratcliffe (1972). In the context of the present study, the ionosphere constitutes a vast laboratory containing a wealth of natural plasma phenomena. The area of plasma physics to be investigated here is concerned with the generation, growth and decay of irregularities in the plasma density. Before this subject is expanded upon, it is necessary to describe briefly the relevant properties of the ionosphere. This includes the nature and distribution of the ionospheric plasma, the origin of electric fields and neutral winds that affect the motion of plasma particles and the diurnal patterns of this plasma motion. The discussion will focus on the high latitude ionosphere where the observations in this study were made.

1.1 Ionospheric plasma

Less than 1% of the ionosphere is ionised. The ionospheric plasma is quasi-neutral. It is dominated by free electrons and the molecular ions NO^+ and O_2^+ below approximately 250km and free electrons and O^+ ions above this level. Due to the combination of production, loss and transport processes, the plasma density is non-uniform with altitude. The plasma densities will vary at a given point as a function of the relative position of the sun to the zenith, leading to strong diurnal and seasonal variations. Figure 1.1 is a height profile of the electron density for both night and day. Early ionosonde studies (Breit and Tuve, 1926) of the ionosphere revealed it to be a stratified medium with respect to the variation of plasma density with altitude. The strata have been assigned names D, E and F as illustrated in Figure 1.1.

1.2 Neutral winds

Since the ionosphere is chiefly populated with neutral particles, it is imperative to mention the motion of these particles, as they can become coupled to the charged

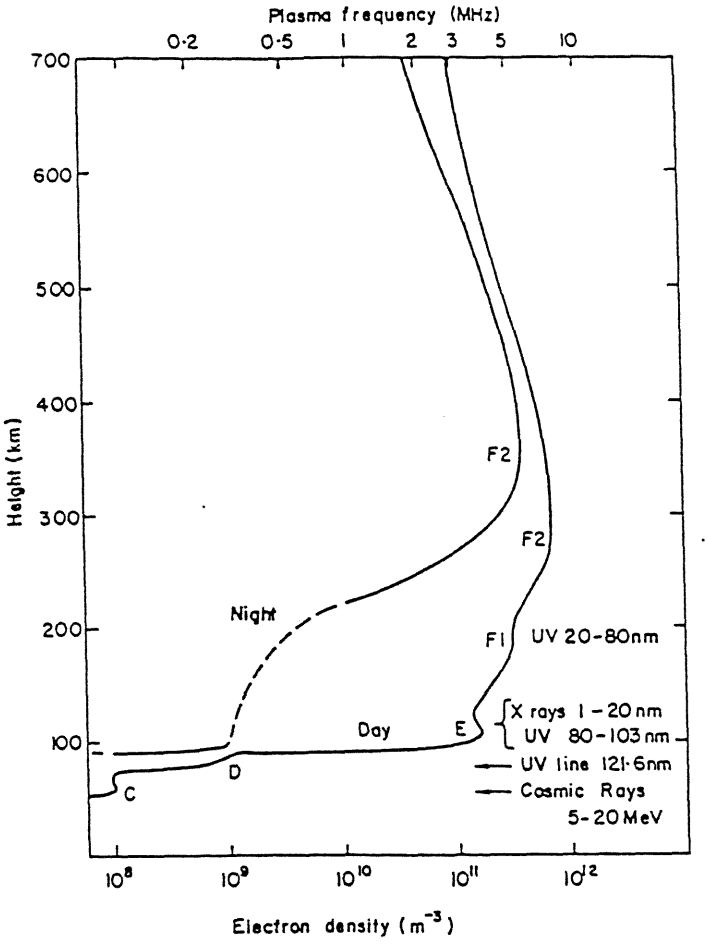

Figure 1.1 Height profile (night and day) of the electron density in the Earth's atmosphere. Marked are the main ionospheric layers and the radiations causing the ionisation (after Rishbeth (1988)).

species through collisions. Neutral particle motions arise due to global temperature variations. The atmosphere is chiefly heated by solar radiation but processes such as particle precipitation and frictional heating between particles also make a contribution. The resulting temperature variations give rise to pressure gradients that drive winds. The exact pattern of neutral winds is determined by a combination of these pressure gradients with the Coriolis force arising from the Earth's rotation, molecular viscosity and ion drag.

1.3 Electromagnetic influences

Much of the shape and behaviour of the Earth's near-space environment has its origin in the sun. The sun emits a continuous stream of cold (~10^5K) and dense (10 cm^{-3}) plasma, travelling outwards at velocities of about 450kms^{-1}. Frozen into this solar wind is the sun's magnetic field that sweeps out into space forming the interplanetary magnetic field (IMF).

The magnetic field of the Earth, at its simplest, can be represented as a dipole field inclined by 12° to the Earth's axis. The flux density at high latitudes (e.g. 70°) at altitudes of 300km above the Earth's surface is 50μT. At further distances from the Earth (~10 Earth radii) the geomagnetic field becomes distorted by the influence of the solar wind. The effect on the geomagnetic field is to compress it on the dayside and stretch it out into a long tail (250+ Earth radii) on the nightside. The cavity so formed, containing the deformed geomagnetic field, is called the magnetosphere. Magnetospheric physics is a very large subject (see Ratcliffe, 1972, Nishida et al., 1982). It is inappropriate to present a detailed discussion of magnetospheric physics here other than to point out that the interaction of the solar wind with the magnetosphere gives rise to plasma motion in the ionosphere through the action of imposed electric fields. Details of early mechanisms for this coupling can be found in Dungey (1961) and Axford and Hines (1961). Kamide and Baumjohann (1993) give a current and detailed discussion of the subject. Further electric fields are generated in the ionosphere by a dynamo effect, involving neutral winds forcing charged particles across the Earth's magnetic field.

1.4 Charged particle motions

The motion of a charged particle in a magnetic field under the action of an applied force is a subject well explained in most elementary texts on electromagnetism, e.g. Bleaney and Bleaney (1976). In the ionosphere electromagnetic forces and collisions

dominate charged particle motion. For a given particle of species 'x' charge 'q_x' and mass 'm_x', a simplified equation of motion is:

$$\frac{dV_x}{dt} = \frac{q_x}{m_x}\mathbf{E} + \mathbf{V_x} \times \Omega_x + \upsilon_x(\mathbf{V_n} - \mathbf{V_x}) \qquad (1.1)$$

where $\mathbf{V_n}$ is the neutral velocity, υ_x is the x-neutral collision frequency and Ω_x is the gyrofrequency of species x. If $\upsilon_x < \Omega_x$ the charged particles are strongly magnetised and move at the Hall drift velocity $\mathbf{ExB}/B^2$ (hereafter referred to as the **ExB** drift). A neutral wind will only move each particle parallel to **B**. If $\upsilon_x > \Omega_x$ the charged particles are dominated by collisions with the neutrals. A wind will move the particles with its own velocity. An applied electric field will force the particles parallel to **E** but at low speeds due to the numerous collisions with neutrals.

Currents will flow in the ionosphere if the electron and ion drift velocities are different. If conditions are such that both species move at the **ExB** drift their velocities are almost the same and any current is small, this situation arises in the F-region of the ionosphere. In contrast, in the E-region the ions are collision dominated and the electrons moves with the **ExB** drift. Under these conditions large currents are possible.

1.5 High latitude plasma convection

Observations of the plasma motion, e.g. Heelis and Hanson (1976), indicate that typical high latitude plasma flows consist of two cells as illustrated in Figure 1.2. The specific morphology of these flows is determined by the orientation of the IMF with respect to the geomagnetic field. General features are that there is flow of plasma away from sun across the polar cap and return flow, towards the sun, at lower latitudes. Since the convection pattern is fixed relative to the sun, an observer at a point P on the Earth will move under this convection pattern as the Earth rotates. From around magnetic midnight to late morning (~10.00 MLT) the observer will see predominantly eastward flows (dawn convection cell). From near magnetic noon to ~23.00 MLT the flows are westward (dusk convection cell).

1.6 Aims of current research

The above brief description presents a picture of the plasma drifting through the atmosphere in a well behaved manner under the action of electric, magnetic and neutral wind fields, with smooth temporal and spatial variations in density. In reality, there are

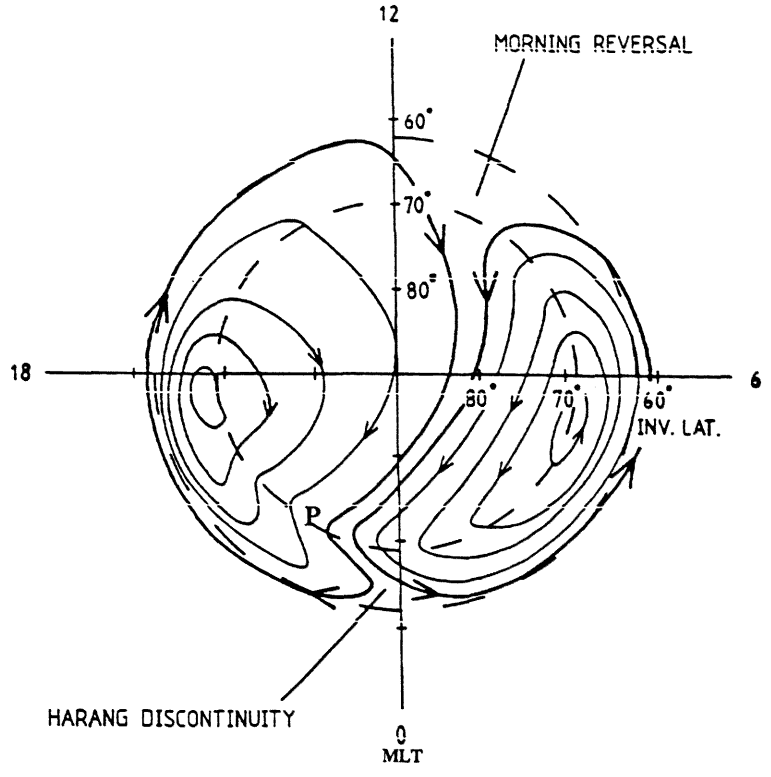

Figure 1.2 High latitude plasma convection

continuous perturbations in the density of plasma due to thermal fluctuations. It is possible to amplify these fluctuations through certain plasma instabilities. The free energy associated with an ionospheric current can feed collective fluctuations of scale sizes above the plasma Debye length and coherent wave-like structures (or irregularities) can occur. It is the characteristics of these irregularities, observed by radars in the E-region of the ionosphere, that is the subject of this investigation. In the next chapter the historical development of irregularity studies and a synopsis of current theory are presented. An explanation of how radar can be utilised to detect irregularities will be the subject of Chapter 3 and Chapter 4 will describe the radar systems employed in this work. Finally the results of the radar observations and their interpretation are presented.

It is the aim of this research to undertake a statistical study of irregularities at a number of irregularity wavelengths, to analyse the relationship between different irregularity parameters at a fixed wavelength and compare the results obtained at different wavelengths. The behaviour of the irregularities will also be studied in comparison with other plasma parameters. This is important since irregularity characteristics are applied to the diagnosis of a large number of geophysical parameters, involved in the study of large-scale waves, plasma convection flows, pulsations and substorms, to give a few examples. These phenomena affect the ionospheric plasma and in turn alter the behaviour of the irregularities. If all of these geophysical phenomena are to be understood it is imperative that a better understanding of irregularities and the means by which they are measured is produced.

Chapter Two

THE OBSERVATION AND THEORY OF IRREGULARITIES

2.1 Introduction

Ionospheric plasma irregularities, which give rise to coherent radar backscatter, are identified with inhomogeneities in the ionospheric plasma which have electron density fluctuation amplitudes greater than those due to random thermal motion. Such inhomogeneities affect the propagation of radio waves of frequencies well above the critical plasma frequency. A comprehensive review of the theoretical and experimental study of ionospheric irregularities has been carried out by Fejer and Kelley (1980). The work which will be presented here is concerned with small-scale irregularities (~ scale sizes < 100m) observed in the E-region of the Earth's ionosphere. The observation and physical characteristics of these small-scale phenomena are now reviewed.

2.2 First detection

Amateur radio operators in the 1930's were probably the first inadvertent observers of irregularities. At times, propagation paths over abnormally long distances were achieved with the best results being obtained with directional antennas pointed North. This propagation phenomenon was thought to be linked with visible aurora. Moore (1951) studied the statistical occurrence of such early observations. The first E-region data originated from experimental work conducted by Harang and Stoffregen on December 16th 1938 at Tromsø. With a broad beam vertical antenna they detected low power echoes from an equivalent height of 400-800km. It is now thought that these returns were due to backscatter from irregularities at low elevation angles. Their work was first reported in Nature, Harang and Stoffregen (1938).

The early observations were motivated by a strong belief that there was a relationship between the radio echoes and visible aurora. For this reason, the observations were often termed radio aurora. However, it was later found that radio and visible aurora were distinct phenomena. Dyce (1955) made observations at 51.9MHz from Point Barrow 900km north of the auroral zone. He employed a continuously rotating antenna and found that 90% of the echoes originated from north of the radar site. The experiment also indicated, that an important factor in the observation of these echoes, was the need to look at low elevation angles. Such

elevation angles provide look directions that are close to perpendicular to the Earth's magnetic field. Chapman (1952) determined the geometry for these observations and found it was necessary for the probing radar direction vector to be perpendicular to the magnetic field. To account for this aspect sensitivity, Booker et al. (1955) proposed that the radio aurora was due to signal returned from columns of ionisation parallel to the magnetic field.

Meanwhile, related research was being conducted at equatorial latitudes. Peculiar echoes were manifest in ionosonde data that were coined 'equatorial sporadic-E'. The first observations were reported in Berkner and Wells (1937) at Huancayo on the geomagnetic equator. The peculiar ionosonde signature of equatorial sporadic-E was strictly a daytime phenomenon. Its behaviour was different from sporadic-E observed at other latitudes. In particular, Matsushita (1951) noted that the critical frequency was related to the strength of the equatorial electrojet. An extensive study of this equatorial sporadic-E was conducted during the International Geophysical Year (1957-58), reported by Bowles and Cohen (1962). The study involved trans-equatorial radio propagation experiments and radar observations at 50MHz from Huancayo. Conclusions of this research were that Equatorial Sporadic-E phenomena were produced by irregularities in the equatorial electrojet, elongated along the magnetic field. Egan (1960) suggested that these equatorial E-region irregularities were similar to those observed with backscatter techniques in the auroral zone. Important work continued at Huancayo and at Lima (Jicamarca) in Peru with backscatter radars operating at 50MHz.

Having set the historical background to the first detection of irregularities, it is now appropriate to describe the properties of the E-region plasma irregularities responsible for these signal returns. The theoretical frameworks that have been constructed to account for the observations will be discussed and the current areas of research and points of intellectual conflict described.

2.3 Properties of E-region irregularities

All E-region irregularity data presented in this work have been derived from coherent scatter radar observations and the details of the experimental technique will be described in the next chapter. Alternative measurements are possible by, for example *in-situ* probes carried through the ionospheric plasma on rockets. Such probes can be constructed to determine electron density fluctuations, electric fields and particle drift velocities. Fejer and Kelley (1980) includes a description of these techniques. Other experimental techniques can determine related plasma parameters such as ion and

electron temperatures and electric fields. Knowledge of these parameters can be of great assistance in irregularity studies. One such technique is incoherent scatter radar and this is also described in the next chapter.

Observations of full backscatter power spectra (for early spectral observations see Bowles, 1954, McNamara, 1955) quickly established that the irregularities did not all share common properties, but that it was possible to identify groups of different type. The observations in Peru led to the definition of Type (I) (Bowles et al., 1960) and Type (II) (Cohen and Bowles, 1967) irregularities. Later observations provoked the introduction of Type (III), first recognised by Fejer et al. (1984), and of Type (IV) first observed by Haldoupis and Sofko (1979) but the terminology was first adopted by Fejer et al. (1986).

Illustrations of these spectral types are given in Figure 2.1, where parts (a) to (d) correspond to Type (I) to Type (IV) irregularities respectively. The typical Type (I) irregularity presents a narrow backscatter spectrum. The width of the spectrum is less than the mean Doppler shift. The spectrum shape is skewed towards lower Doppler shifts. The sense of the Doppler shift is always in the direction of the plasma flow component along the radar line-of-sight. The equatorial observations indicated that the mean Doppler shift was usually about 300-400m/s, which is of the order of the ion-acoustic speed. This phase speed was constant over all elevation angles when looking east or west. In an equatorial geometry this corresponds to looking at different angles with respect to the plasma flow direction. Auroral observations presented similar findings. The auroral spectra have the same distinctive shape, but the mean Doppler shift is often larger than the values observed in equatorial experiments. Measurements of the plasma drift velocity in conjunction with Type (I) irregularities, indicated that the irregularities were only generated when the plasma drift speed was equal to or greater than a threshold speed identified as approximately the local ion acoustic speed (e.g. Nielsen and Schlegel, 1983, Kofman and Nielsen, 1990).

Type (II) irregularities, Figure 2.1(b), appear as broad spectra, peaked at small Doppler shifts. The spectral width is of the same order or greater than the mean Doppler shift. Their spectral shape is not noted for any systematic skewness. The phase velocity is proportional to the plasma drift velocity and also varies as a function of the angle between the plasma drift velocity and the direction of irregularity propagation.

The two other, more recent classifications, of irregularities have only been observed in high latitude experiments. Type (III) spectra are characterised by narrow spectra at phase speeds below the ion acoustic speed. Type (IV) spectra are also narrow but at

(a)

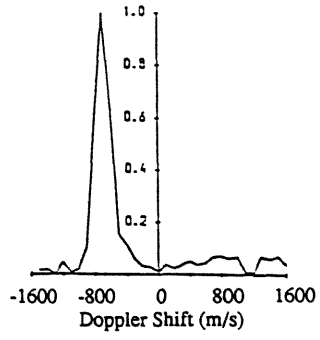

(b)

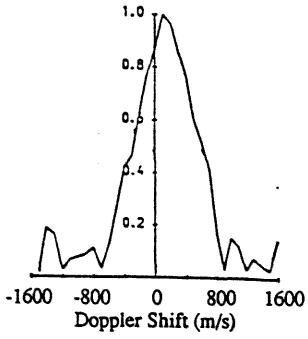

(c)

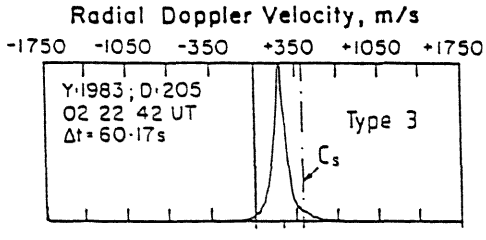

adapted from Haldoupis et al.(1985)

(d)

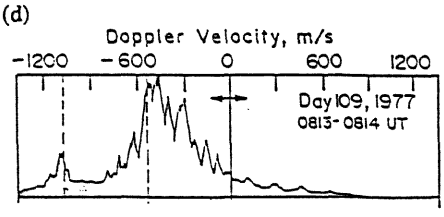

adapted from Haldoupis and Sofko (1979)

Figure 2.1 Examples of spectral types; (a) Type (I), (b) Type (II), (c) Type (III) and (d) Type (IV).

high Doppler shifts, of the order of 1000m/s. They tend to appear only for periods of short duration and often in conjunction with a second peak in the backscatter spectrum at a smaller phase speed that has the characteristics of a Type (II) irregularity.

2.4 The theory of E-region irregularities

The existence of radar echoes and their aspect sensitivity provided impetus to the development of theory. Early ideas involved a link with visible aurora. To account for the poleward pointing directions and the low elevations that were required to observe irregularities at high latitudes a number of ideas were suggested. Harang and Landmark (1954) proposed the echoes were ground scatter, propagated by a smooth bottomed sporadic layer and hence could only be observed at low elevations. Currie et al. (1953) conjectured that the echoes originated from ionisation of a configuration that matched the auroral forms. In this model, no backscatter was observed at high elevations since at these angles a lot of absorption occurred in lower regions of the aurora. It was Booker et al. (1955) and Moore (1952) who suggested that the backscatter was due to columns of ionisation aligned parallel to the Earth's magnetic field. Later Booker (1956) developed a theory that the irregularities were generated due to non-isotropic turbulence. It predicted that the irregularities are always elongated along the magnetic field with correlation distances of 5-10m while perpendicular to the magnetic field the correlation distance is less than 1m. The theory was able to account for the echo strength and aspect sensitivity but was unable to explain the observed Doppler shift (Bowles, 1954) of the returned signal relative to the transmitted frequency. Moore (1952) suggested the precipitation of high energy protons down magnetic field lines might give rise to columns of ionisation similar to meteor trails. This idea floundered when radar echoes were observed in conjunction with homogeneous auroral structures and also because Booker (1956) had established that the columns of ionisation were only of the order of 10m long. In turn, Booker's generation mechanism was questioned because it would produce irregularities with correlation distances that were larger perpendicular to the field than they were parallel to it. However, it was the development of further theories regarding turbulence and the operation of certain plasma instabilities in the ionosphere that were able to begin to take account of the observations.

2.4.1 Instabilities in the plasma

The ionospheric plasma is in continuous random thermal fluctuation. The random fluctuations can be represented as the superposition of sinusoidal perturbations in the plasma density through all wave vectors **k**. Under appropriate conditions, the plasma can become unstable and the growth of density perturbations occurs, resulting in the

generation of plasma waves. These plasma waves are electrostatic and longitudinal in nature. Their phase fronts align almost exactly parallel to the magnetic field, since the electrons are free to move in this direction and not perpendicular to the field. Also, the growth of the smallest scale waves propagating parallel to B is restrained by strong Landau damping. This results in ionised structures parallel to B similar to that postulated by Booker at al. (1955). Furthermore, since the waves are periodic density structures, a radar oriented to look perpendicular to the magnetic field will receive constructive interference from planes of ionisation spaced at $\lambda/2$ intervals, where λ is the radar wavelength. This process is analogous to Bragg scatter in a crystal. For a simple continuous wave experiment, the power in the signal will be related to the scatter cross-section of the irregularity and Doppler shifts of the signal will result from the phase propagation of the irregularity.

Important plasma instabilities are the two-stream and gradient-drift instabilities, which in the ionosphere have been associated with Type (I) and Type (II) waves respectively. The theory developed to describe these plasma instabilities will be discussed in the following sections. The origins of Type (III) and Type (IV) irregularities are not unequivocally established, possible mechanisms for their generation will also be discussed.

2.4.2 Instability mechanisms

The two stream instability arises if there is a significant differential flow between the ions and electrons, in excess of the local ion-acoustic speed. This is possible in the E-region since at these altitudes the ions are collision dominated with the neutrals up to around 120km and thus to first order stationary, while the electrons move at the ExB drift. The gradient drift instability requires a gradient in the background electron density of suitable orientation and a drift between the ions and electrons.

Dispersion relations for the plasma waves resulting from the plasma instabilities are readily derived by applying either kinetic or fluid plasma theory. The pertinent details of this will be presented in the next section. The conditions of excitation and physical properties of the stabilised irregularities can be predicted from the dispersion relation. To give a physical description of the action of the instabilities to produce a plasma wave and then their subsequent evolution is difficult and not necessarily worthwhile. The problem is more eloquently phrased in mathematics. A good description of the gradient drift mechanism can be found in Ossakow and Chaturvedi (1979). Kelly (1989) describes the nature of the two-stream instability. In generalised terms, the plasma irregularity will grow if the original density perturbation is augmented in some manner.

More energy must enter the wave than leaves it through the operative damping mechanisms.

2.4.3 Linear Theory

Linear dispersion relations for the plasma waves can be derived by fluid e.g. Buneman (1963) or kinetic e.g. Farley (1963) means (kinetic methods must be applied if the sampling wavelength is of the same order or less than the ion mean-free-path). It is conventional to represent the amplitude (Φ) of the plasma wave in terms of an exponential function containing a time (t) varying and space (**r**) varying part as:

$$\Phi(\mathbf{r},t) = \Phi_0 e^{-i(\omega+i\gamma)t} e^{i\mathbf{k}.\mathbf{r}} \qquad (2.1)$$

Where ω and γ are the real and imaginary parts of the wave frequency, i.e. the angular frequency and the growth rate respectively and **k** is the wave vector. Linear theory e.g. Sudan et al. (1973) finds expressions for these important parameters of:

$$\omega = \frac{\mathbf{k}.\mathbf{V_D}}{(1 + \Psi)} \qquad (2.2)$$

$$\gamma = \frac{\Psi}{(1 + \Psi)}\left(\frac{\omega^2 - k^2C_s^2}{\upsilon_i} + \frac{\omega\Omega_e}{kL\upsilon_e}\right) \qquad (2.3)$$

where

$$\Psi = \frac{\upsilon_e\upsilon_i}{\Omega_e\Omega_i}\left(1 + \frac{\Omega_e^2\sin^2\delta}{\upsilon_e^2}\right) \qquad (2.4)$$

The symbols have the following meanings:

$\mathbf{V_D}$	plasma drift velocity
C_s	ion-acoustic speed
υ_x	frequency of collisions between species x and neutral particles
W_x	gyrofrequency of species x
δ	angle between the irregularity wave vector and the direction of the magnetic field (magnetic aspect angle)
L	gradient scale length

with the subscripts 'i' and 'e' referring to ions and electrons respectively.

Equations 2.2 and 2.3 incorporate the description of both two-stream and gradient drift waves. The angular frequency ω is the same in each case. Equation 2.2 states that

the irregularity phase speed (ω/k) is equal to the component of the drift velocity in the direction of the radar line of sight, modified by a factor $(1+\Psi)^{-1}$. Thus the phase speed is always a little smaller than the drift speed of the plasma, even for those irregularities that propagate in the direction of the plasma flow. From the phase velocity measured by coherent backscatter radar, this relationship enables the plasma drift velocity to be estimated and hence the E-region electric fields can be calculated (Ecklund et al., 1977, Tsunoda, 1975). An important parameter in Equation 2.3 is the ion-acoustic speed C_s which is a function of both the ion and electron temperature (T_i, T_e) and the mean ion mass $<m_i>$,

$$C_s = \sqrt{\frac{k_B(\gamma_i T_i + \gamma_e T_e)}{<m_i>}} \qquad (2.5)$$

where γ_x is the specific heat ratio of species 'x' and k_B the Boltzmann constant.

There are a number of observational characteristics that linear theory cannot account for. Linear theory predicts that there should be no generation of Type (II) irregularities of a wave number $k > k_c$ where

$$k_c \approx \left(\frac{\Omega_e \upsilon_i V_D}{(1+\Psi)\upsilon_e L C_s^2}\right)^{\frac{1}{2}} \qquad (2.6)$$

However, Type (II) waves have been observed at wavelengths that do not comply with this condition, e.g. Balsley and Farley (1973).

Linear theory also predicts that two stream irregularities will be generated at phase speeds close to the ion acoustic speed when the plasma drift speed satisfies the relation:

$$V_D \cos\vartheta > (1+\Psi)C_s \qquad (2.7)$$

where ϑ is the angle between the plasma drift velocity and the direction of propagation of the irregularity. Above this threshold the irregularity phase speed will vary as described by Equation 2.2. Observations confirmed a threshold speed for two-stream irregularity excitation but the phase speeds were then observed to saturate at close to the threshold speed (e.g. Bowles et al., 1963, Abel and Newell, 1969). The linear theory is unable to account for this.

2.4.4 Non-linear theory

To explain the observation of short wavelength gradient drift waves, the plasma must become turbulent with energy being transferred to small scale waves from larger waves. This occurs through the non-linear interaction of three waves k, k′ and k″. With

$$|\mathbf{k}| \sim |\mathbf{k}'| \sim |\mathbf{k}''| \text{ and } \mathbf{k} = \mathbf{k}' + \mathbf{k}'' \qquad (2.8)$$

Further to this, Sudan et al. (1973) adopting an equatorial geometry, calculated that the horizontal gradients of plasma density and vertical electron drifts associated with large ($\lambda \sim 50$ to 100m) scale irregularities were sufficient to excite both gradient drift and two-stream waves propagating perpendicular to the plasma drift.

The derivation of a non-linear dispersion relation was required to account for the saturation of Type (I) phase speeds near the ion acoustic speed. There were a number of theories presented throughout the mid-seventies to account for the observations, a description of these can be found in Fejer and Kelley (1980). Much of this theory addressed the problem by focusing on Type (I) irregularities alone. Sudan (1983) developed a unified theory of Type (I) and Type (II) irregularities (in an equatorial context) incorporating suitable plasma turbulence theory. The theory was able to predict the power spectrum of Type (I) and Type (II) irregularities both in absolute magnitude and wave number variation, describe the width of Type (II) irregularities and the limitation in the Type (I) phase speeds. Following Dupree (1966), Sudan (1983) suggested that a wave-particle interaction was capable of transferring momentum from short wavelength waves to the electrons. This resulted in cross-field particle diffusion and the stabilisation of the two-stream waves.

The non-linear dispersion relation results from replacing υ_e by $\upsilon_e + \upsilon_e^*$ where υ_e^* is the anomalous electron collision frequency resulting from the interaction between the electrons and waves. Thus the only change in the dispersion relation comes in Ψ which is replaced by $\Psi + \Psi^*$ as follows:

$$\omega = \frac{\mathbf{k}.\mathbf{V_D}}{(1 + \Psi + \Psi^*)} \qquad (2.9)$$

$$\gamma = \frac{\Psi + \Psi^*}{(1 + \Psi + \Psi^*)}\left(\frac{\omega^2 - k^2C_s^2}{\upsilon_i} + \frac{\omega\Omega_e}{kL\upsilon_e}\right) \qquad (2.10)$$

υ_e^* is defined in terms of an anomalous diffusion constant D*, the details of which can be found in Sudan (1983).

Now as the wave grows the Ψ^* term increases reducing the growth rate to zero and causing a shift in the phase velocity to keep it at C_s. Thus whenever the threshold condition 2.7 is satisfied, irregularities are generated with wave vectors perpendicular to the magnetic field in a fan of angle ϑ_m about the plasma flow direction. ϑ_m is the solution of condition 2.7 when the left-hand-side is set equal to the right-hand-side. The two-stream waves generated propagate at close to the ion acoustic speed over all directions in which they are excited. Waves propagating with small k-parallel components will also exist, becoming more strongly damped as the magnetic aspect angle (δ) decreases from 90°.

2.4.5 Application of theory to auroral irregularities

The majority of the early theory was developed to explain observations of irregularities in the equatorial electrojet, predominantly at 50MHz. Extensions of the theory were later applied to explain irregularities observed at auroral latitudes. Fejer et al. (1984) first pointed out that there were important differences between the equatorial and auroral regions which limited the application of the former theories to the latter. Ion gyrofrequencies are twice as large at auroral latitudes and the plasma drift velocities can be significantly larger. The fluid theories also had the limitation of being inapplicable for wavelengths < 1m since k^{-1} ~ the ion mean free path and kinetic calculations need to be adopted. Schlegel (1983) developed a full kinetic theory and applied it to the auroral E-region, in order to help interpret observations from the Scandinavian Twin Auroral Radar Experiment (STARE) of 1m wavelength irregularities.

Observations of electron temperatures of more than twice the neutral or ion temperatures in the auroral E-region (e.g. Schlegel and St-Maurice, 1981) and in earlier work at equatorial latitudes (e.g. Weinstock and Sleeper, 1972), prompted the idea that unstable waves driven by large plasma drifts were able to heat the plasma. Robinson (1986) developed a theory that included wave enhanced diffusion in a situation where wave heating was important. This was achieved by modifying the electron energy balance equation to include terms describing the anomalous diffusion. An important aspect of the theory is that as the plasma drift increases the wave heating increases and the electron temperature is raised. This results in an elevation of the ion acoustic speed and so the Type (I) irregularities become stabilised at a higher phase speed. Figure 2.2 is a plot of C_s against electron drift taken from Robinson (1986). This clearly

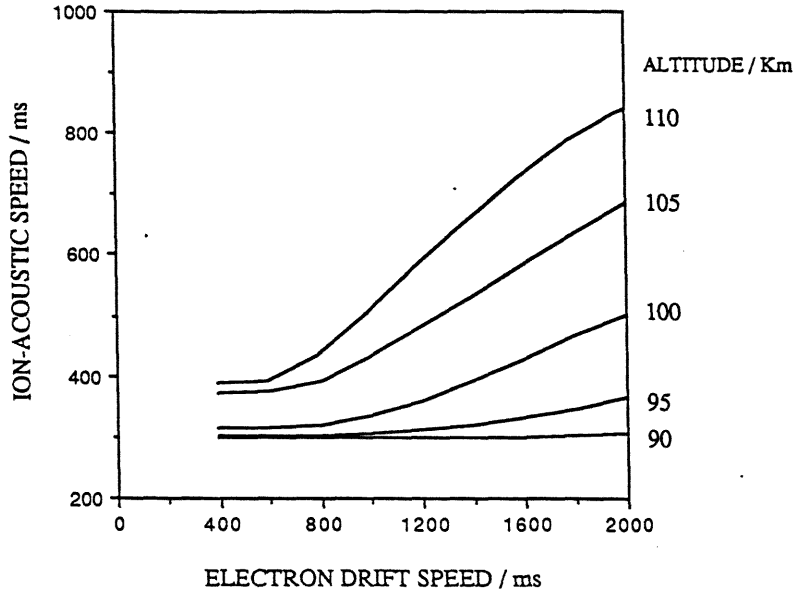

Figure 2.2 Theoretical curves of the variation of the ion acoustic speed with the electron drift speed. The relationship has been calculated for five altitudes from the fluid theory of Robinson (1986).

emphasises an important point, that the ion acoustic speed is a strong function of the altitude in the scattering layer. The theory has been applied successfully to account for the STARE observations of Nielsen and Schlegel (1985) and Williams et al. (1992) has applied it successfully to observations of electron temperatures with EISCAT. Robinson and Honary (1990) extended Robinson's (1986) paper to a full kinetic theory and investigated the variation of the irregularity phase speed with wavelength, aspect angle and flow angle.

2.4.6 Theories behind other spectra

The above theories do not readily account for Type (III) and Type (IV) spectra. In response to Type (III) observations at Ithaca with a 50MHz radar, Fejer et al. (1984) postulated that the irregularities occurred due to ion cyclotron waves generated by field-aligned currents. Haldoupis et al. (1985) and Prikryl et al. (1987) demonstrated that the Type (III) phase speeds correspond to angular frequencies close to the gyro-frequencies of O^+ and NO^+. However, reservations about this mechanism soon developed. The observation of Type (III) echoes was very sporadic, whereas field-aligned currents are usually present during active geophysical conditions. Furthermore, theoretical studies indicated that the electron drifts required to drive the instability had to be of the order of 100s of kms^{-1} (Seyler and Providakes, 1987). A more recent suggestion, Haldoupis et al. (1992), is that Type (III) are just Type (I) irregularities excited under conditions where the threshold drift velocity has been lowered. Such conditions may arise in the presence of intense sporadic E. This would provide a strong destabilising gradient and a lowering in the ion-acoustic speed due to the presence of heavy ions like Fe^+.

Similarly, Type (IV) waves were first suggested to be Type (I) irregularities occurring at an increased threshold speed. Under strongly driven conditions, the plasma waves reach large amplitudes and there is strong heating of the electrons. This increases the local electron temperature and thus the ion-acoustic speed (Fejer et al., 1986). Alternatively, Zarnitskiy (1989) postulated that the irregularities are in fact plasma waves with phase speeds close to the true ExB drift speed. Haldoupis et al. (1991) proposed that Type (IV) waves exhibit preferential phase speeds at twice the ion-acoustic speed. The generating mechanism would then involve two Type (I) waves pumping energy into the amplification of a Type (IV) wave.

2.5 The interpretation of spectra

The theoretical ideas presented above are able to account for many aspects of the observations. However, this does not imply that all the problems regarding the

understanding of irregularities have been resolved. The origin of Type (III) and Type (IV) spectra is still an open question, which requires improved measurements to resolve. Characterising irregularities in terms of a strict Type (I) to (IV) nomenclature may preclude the best description and understanding of ionospheric irregularities, since many spectra have a combination of characteristics and cannot be readily identified as corresponding to a particular type. Furthermore, the typing of spectra is dependent on the irregularity exhibiting characteristics specific to the generated plasma instability. The spectrum can also be affected by limitations of the radar system and other properties of and influences on the probed plasma.

The majority of past work has concentrated on the interpretation of power and phase speed measurements. The width and degree of symmetry of spectra are further quantities that may have significant physical meaning but are currently not well understood. Spectral width observations will be of particular interest in this work therefore their interpretation is now reviewed.

2.5.1 Spectral widths

The broadening of a coherent scatter spectrum may occur due to the growth or decay of the observed irregularities, random turbulence in the plasma motion that modulate the irregularity phase speeds or from differential changes† between stable patches of irregularities in the scattering volume. If the irregularities were long-lived waves that remained fixed relative to each other and persisted without decay for the duration of the integration time of the received radar signal, their spectra would be delta functions at a Doppler shift equal to the phase speed of the propagating wave. This is not what is observed.

If an irregularity is defined as in Equation 2.1 the form of the frequency spectrum can be established by taking the Fourier transform of 2.1, i.e.:

$$F(\omega') = \Phi_o \frac{2\gamma}{(\omega - \omega')^2 + \gamma^2} \qquad (2.11)$$

Equation 2.11 describes a symmetric spectrum about ω of full width at half maximum of 2γ. This implies the spectral width is directly proportional to the irregularity growth rate. There are a number of problems with this model. Typically, the observed spectra are not symmetric. For two-stream waves that saturate at the ion-

† Such changes may occur if the background plasma is modulated, for example, by a large scale gravity wave. This may induce periodic changes in the plasma density and plasma drift velocity.

acoustic speed the growth rate is zero and this would result in no spectral width. Equation 2.11 does not take any account of the simultaneous observation of irregularities with different phase speeds, growth rates and amplitudes.

Hanuise et al. (1993) have conducted important work on how the correlation length of plasma motion affects the observed coherent scatter spectrum. These authors utilised scattering theory relevant to a non-uniform plasma following Holzhauer and Massig (1978). They derived two forms of coherent scatter spectrum; a Gaussian Doppler spectrum resulting from velocity dispersion and a Lorentzian spectrum, arising if the scattering wavelength was longer than the correlation length of the plasma motion. Data analysis techniques have taken account of such different spectral forms, e.g. Villain et al. (1987).

Each type of spectral shape exhibits different variations in the spectral width as a function of the wave number. Gaussian spectral widths are proportional to k^1 while Lorentzian widths vary as k^2. An alternative theory for the origin of the spectral width for two-stream irregularities was formulated by Sudan (1983). Sudan proposed that the spectrum was broadened due to the presence of random turbulence in the electron drift due to a background of Type (II) irregularities. This theory predicts that the spectral width is proportional to $k^{2/3}$.

2.6 Summary

This review has described the historical development of the theory of coherent scatter and established the current theoretical description of ionospheric irregularities. In later chapters these theoretical ideas will be employed in the interpretation of experimental observations. In other cases, the experimental data will pinpoint shortcomings in current theory and areas where improvement is necessary will be suggested.

Chapter Three

EXPERIMENTAL TECHNIQUES

3.1 Introduction

The experimental observations of plasma irregularities to be presented in later chapters were obtained with coherent scatter radars. Supporting these observations, incoherent scatter radar measurements have provided important information regarding background plasma parameters. These radar techniques are now described.

3.2 Coherent backscatter radar

3.2.1 Geometrical considerations

As described in Section 2.4.1, the plasma irregularities are aligned parallel to the Earth's magnetic field (**B**). Consequently, the propagation direction of the transmitted radio waves has to be perpendicular to the direction of the magnetic field to obtain the largest backscatter cross-section. This determines the observing geometry for a particular radar frequency.

The propagation of radio waves of frequency equal or greater to VHF (30-300MHz) is essentially rectilinear in the ionospheric plasma. Refraction of waves at these frequencies will only occur during large and rapid changes in refractive index such as in the presence of strong auroral arcs, e.g. Prikryl and Cogger (1992). In order to obtain orthogonality at equatorial latitudes, a VHF radar is restricted to looking only at elevations in an east-west magnetic plane, Figure 3.1(a). Observations both in the E-region and F-region are possible. At auroral latitudes, VHF radar are limited to only E-region measurements. This is achieved by looking polewards at low elevations. Azimuthal variations of the order of $\pm 10^{\circ}$ are also possible while still maintaining the necessary condition of orthogonality, Figure 3.1(b).

HF (3-30MHz) radars have extra flexibility because refraction of these waves in the ionosphere allows orthogonality to be achieved in the E and F-regions at auroral latitudes. Figure 3.1(c) illustrates refraction in a vertical plane which allows the radar to be located equatorward or poleward of the scattering region. In addition, refraction in an azimuthal plane is possible. The benefits of HF refraction also present a problem.

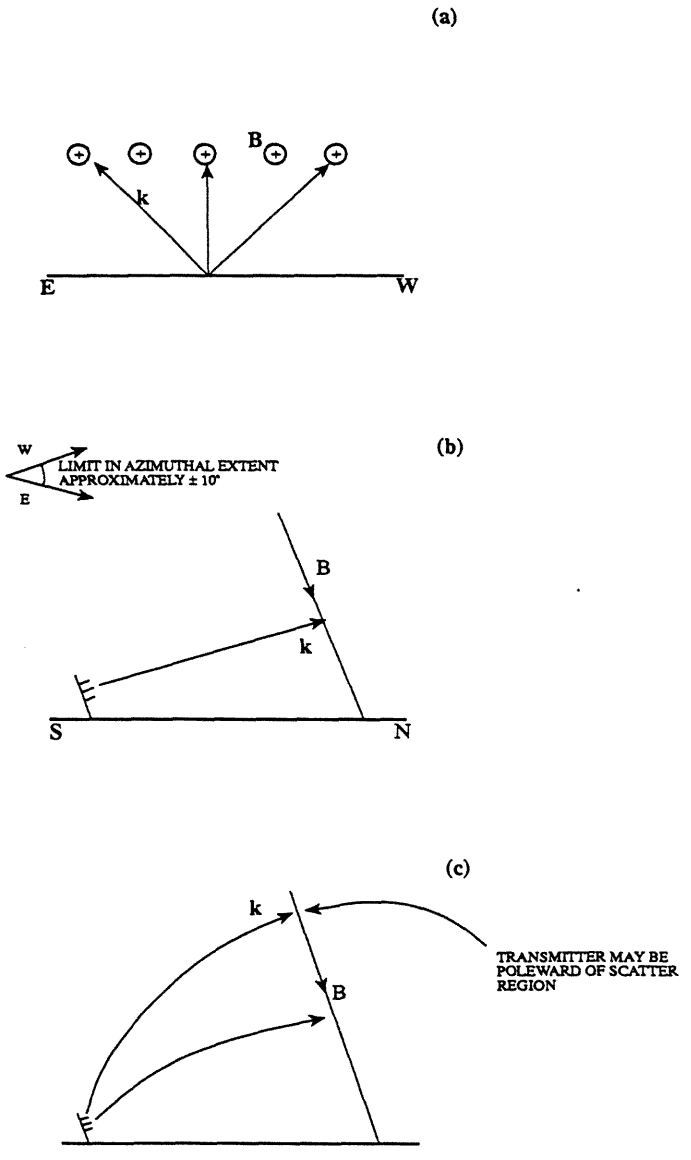

Figure 3.1 Radar geometries for observing irregularities. (a) equatorial location, (b) auroral VHF observation of E-region and (c) auroral HF observation of E and F region. Radar wavevector k.

The refraction leads to less certainty in the position from where the backscatter originates. This problem can be overcome, to some extent, by having local plasma density information and applying ray tracing techniques to determine the ray trajectories, e.g. Villain et al (1984).

3.2.2 Measurement principles

Coherent scatter radars rely on scatter from enhanced non-thermal plasma density fluctuations. The radar will detect irregularities of a wave number k:

$$k_{irreg} = 2k_{radar}\cos(\alpha/2) \qquad (3.1)$$

where α is the angle between the transmitted and the received signal. The phase of the transmitted signal is preserved in a reference signal and is compared with the received signal, allowing the characteristics of the irregularities to be deduced. This is illustrated in Figure 3.2. Often the transmitter and receiver are co-located and the angle α is then 0° and the radar detects direct backscatter. More than one radar can be positioned to observe the same scattering volume from separate locations. This gives information about irregularities propagating in different directions. Thus radar systems are described as monostatic (single-station), bistatic and so on depending on the number of component radars.

To explain the principle of coherent detection let the received signal be of the form:

$$r_1(t) = A(t)e^{i(\xi t+\phi)} \qquad (3.2)$$

where ϕ is the change in phase angle of the received signal relative to that transmitted and ξ is the angular frequency of the radar signal. Combining Equation 3.2 with the reference signal, which can be taken as

$$r_0(t) = e^{i\xi t} \qquad (3.3)$$

the result is:

$$\langle r_0^* r_1\rangle = A(t)\cos\phi + iA(t)\sin\phi \qquad (3.4a)$$

or writing the real and imaginary parts as 'x' and 'y' respectively:

$$\langle r_0^* r_1\rangle = x + iy \qquad (3.4b)$$

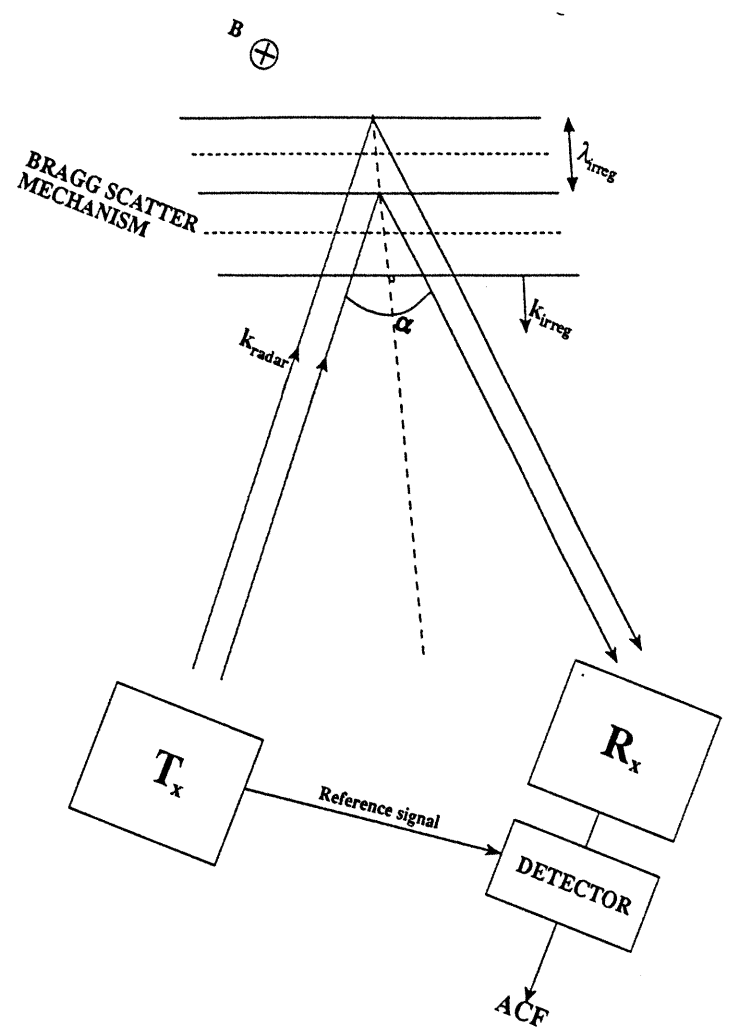

Figure 3.2 Basics of coherent radar

It is trivial to extract the real and imaginary parts from this signal. This allows the calculation of the phase change and amplitude of the returned signal that results from scatter from the irregularity.

$$\phi = \tan^{-1}\left[\frac{y}{x}\right] \qquad (3.5)$$

$$A(t) = \sqrt{x^2 + y^2} \qquad (3.6)$$

3.2.3 Single pulse

A 'simple' radar may involve the transmission of a single pulse of radiation of length τ. If the correct geometry is satisfied, some of this energy pulse will be scattered back. The phase and amplitude of the scattered pulse can be established following the practical implementation of the principle of Section 3.2.2. The measurement of a solitary phase angles gives little physical information. The amplitude of the signal is related to the irregularity backscatter cross-section through the radar equation, detailed in Section 3.2.8. Furthermore, the transmission of a pulse will give range information about the scattering objects. The time for a transmitted pulse to propagate to a scattering object and be returned (t_f : time-of-flight) is related to the range 'R' by:

$$R = \frac{ct_f}{2} \qquad (3.7)$$

Since the pulse has a finite length τ, every time the returned signal is sampled the return will contain contributions from the pulse scattered from different ranges. This imparts a resolution limit to the range measurement of $c\tau/2$. To obtain good power measurements it is often necessary to average the returned signal over a number of pulse returns. This puts a lower limit on the time between each pulse transmission, known as the inter-pulse period (IPP). The IPP is determined by the minimum and maximum range from which backscatter is expected. If the IPP is too small, returned signals from different ranges will reach the receiver at the same time, contributing to a phenomena known as cross-range noise (e.g. Whitehead, 1983). More powerful transmitters and more sensitive receivers will reduce the need for long returned signal integration times.

It is possible to obtain more information about the detected irregularities if a repeated sequence of pulses is transmitted.

3.2.4 Double pulse

Two pulses are transmitted at a temporal separation of T_p, usually some integer multiple of τ. T_p will be less than the IPP and thus will result in the introduction of cross-range noise to any measurement. Following the procedure in Section 3.2.2, the radar will be able to measure the power and phase of each pulse in the double pulse. Furthermore, the phase change $\Delta\phi$ from one pulse to the next can now be calculated. If the scattering irregularities remain correlated for longer than T_p then $\Delta\phi$ will be related to the phase speed (V_{ph}) of the observed plasma wave.

$$\Delta\phi = \frac{\text{(distance moved by phase front)}}{\lambda} 2\pi \qquad (3.8)$$

$$\Delta\phi = \frac{2T_pV_{ph}}{\lambda} 2\pi \qquad (3.9)$$

The measurement of the phase change will give the phase speed of the scattering object in the duration of observation.

3.2.5 Full spectral measurements

Transmitting a sequence of pulses and comparing each return with a reference signal will give extra information about the scattering object. This information is contained in the auto-correlation function (ACF) of the backscatter signal. To calculate the ACF products:

$$R(n,t) = \langle r^*(t)r(t+n\tau)\rangle \qquad (3.10)$$

are formed where n=0,1,2... correspond to successive lags. Typically the real and imaginary parts of this function resemble damped sinusoidal waves, Figure 3.3(a). A discrete Fourier transform of the complex ACF gives the backscatter power spectrum, Figure 3.3(b).

It is evident that the single pulse and double pulse methods provide information that is a subset of the ACF. The single pulse method is equivalent to the zeroth lag of the ACF, the double pulse method is an ACF consisting of just the zeroth and first lag.

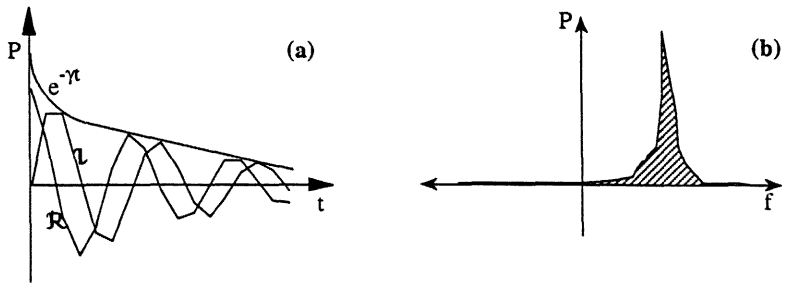

Figure 3.3 The real $\Re$ and imaginary $\Im$ parts of the backscatter autocorrelation function (ACF) (a). A Fourier transform of the ACF gives the power spectrum (b).

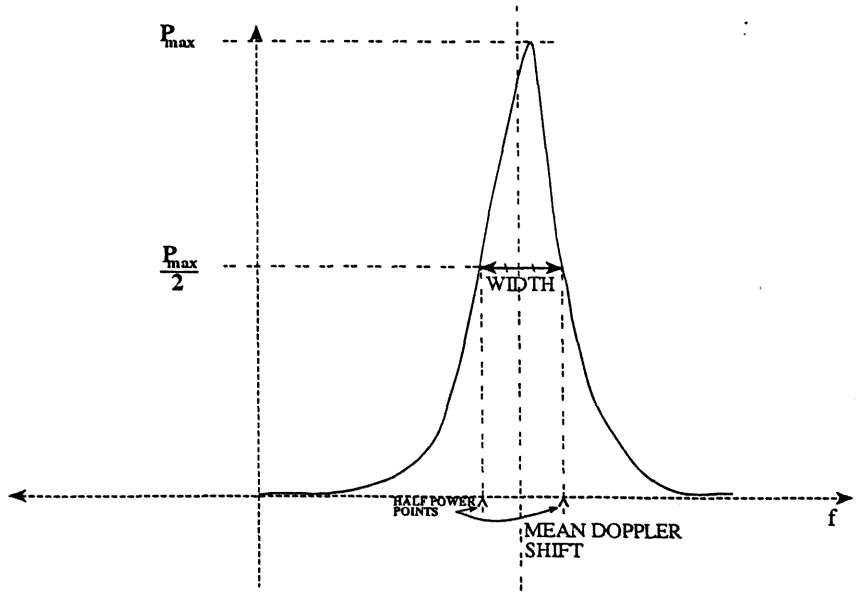

Figure 3.4 Power spectrum illustrating the estimate of the first (mean Doppler shift) and second (width) spectral moment.

3.2.6 Continuous wave (CW) methods

If the transmitter and receiver are sufficiently separated in space the radar can operate in a continuous wave transmission mode. Transmitter and receiver separation is necessary to avoid direct detection of the transmitted signal by the receiver (i.e. with a pulsed system the receiver samples during the transmitter 'off' periods). Provided the receiver and transmitter are correctly oriented to satisfy the necessary orthogonality condition then backscatter will be detected when irregularities are present. The receiver samples the continuously returned signal in whatever pattern desired, integrates for a chosen number of cycles and so constructs the ACF. This has the advantage of allowing a high time resolution. However, the lack of any definite structure in the signal means that no range information is available.

3.2.7 Deduction of irregularity parameters

The output of a coherent backscatter radar is the ACF of the backscattered signal. To illustrate how this relates to the properties of a wavelike plasma irregularity it is helpful to consider the following idealised situation. Assume that the pulse returns originate from the same plasma wave at a fixed point in space. The phase change from pulse to pulse then represents the change in phase of the wave at that point. Furthermore, the power in each successive pulse is related to the time evolution of the amplitude of the wave.

Let us consider the time variation of the irregularity to be of the form

$$\Phi = \Phi_0 e^{-i(\omega+i\gamma)t} \qquad (3.11)$$

The amplitude of this wave will exhibit a sinusoidal variation with a period of $2\pi/\omega$. The maximum amplitude will decay at a rate equal to γ. Pulses scattered from such an irregularity will contribute to an ACF mirroring the properties of this wave. The power in the zeroth lag will be related to the maximum amplitude of the wave Φ_0 i.e. at t=0. The rate of the change in phase angle of the ACF will give ω. The decay rate in the absolute power of the ACF will give the growth rate γ. Thus it is possible to establish irregularity properties from the ACF.

In practice, the radar returns are more complex. The scattered signal contains contributions from a scatter volume distributed in range, height and azimuth. The height and azimuth extent results from the finite beam-width of the radar. The scatter volume is filled with irregularities that may grow and decay at different rates, propagate at

different phase speeds with different amplitudes. All this information becomes absorbed into each radar measurement. The result is a measured ACF that does not correspond to the ideal model of Equation 3.11. To obtain the mean Doppler shift and power the procedure above will work. To estimate the decorrelation in the signal relies on choosing a function that fits the data best. The two types of function to apply (Section 2.5.1) are a Lorentzian or Gaussian decorrelation:

$$e^{-i(\omega+i\gamma)t} \text{ (Lorentzian)} \qquad (3.12a)$$

$$e^{-i\omega t-(\beta t)^2} \text{ (Gaussian)} \qquad (3.12b)$$

On occasion a combination of these functions gives the best fit.

Another approach is to obtain this information from the backscatter spectrum. The irregularity parameters are related to moments of the spectrum. The zeroth, first and second moment (M_i) are defined for a power spectrum $F(\omega)$ as follows:

$$M_0 = \int_{-\infty}^{\infty} F(\omega)d\omega \qquad (3.13a)$$

$$M_1 = \overline{\omega} = \int_{-\infty}^{\infty} \omega F(\omega)d\omega \qquad (3.13b)$$

$$M_2 = \int_{-\infty}^{\infty} (\omega - \overline{\omega})^2 F(\omega)d\omega \qquad (3.13c)$$

The zeroth moment is the area under the spectrum which is the total power scattered back to the receiver. The first moment is the mean Doppler shift, equivalent to the average phase speed of the irregularities observed. The second moment of the spectrum gives its mean square width. If a Fourier transform of Equation 3.11 is performed, the result is a Lorentzian spectrum of a full width at half maximum equal to 2γ. Thus irregularity parameters can be determined from the spectrum.

Integrating the Equations 3.13(a) to 3.13(c) numerically is a time intensive process requiring large computing resources. In practice the spectral moments are estimated by different means. Figure 3.4 illustrates how the mean Doppler shift can be estimated as the Doppler shift at the midpoint of the two half power points on the spectrum. The spectral width can be estimated as the width of the frequency spectrum at the half-

power points. To calculate power, it is simplest to take the power of the zeroth lag in the ACF.

Higher moments give further information about the shape of the spectrum. The physical meaning of the higher moments becomes increasingly obscure. For example, the third moment is the skewness of the spectrum. Skewness describes the symmetry of the spectrum about its mean Doppler shift. Both Gaussian and Lorentzian spectra, which have a physical basis as described in Section 2.5.1, have zero skewness. Values of non-zero skewness indicate deviations from either of these models. Reasons for the origin of skewness include the simultaneous observation of multiple spectra at different Doppler shifts or the phase velocity and growth rate of an irregularity may change as the irregularity evolves.

3.2.8 The radar equation

The backscatter power measured is dependent on a number of factors in addition to the irregularity cross-section. The important relationships are summarised in the radar equation:

$$P_s = \frac{P_t G_t A_r V_s \sigma}{4\pi r_1^2 r_2^2} \qquad (3.14)$$

where

P_s	power received
P_t	power transmitted
G_t	transmitter gain
A_r	effective area of receiving antenna
V_s	volume of scatter region
σ	irregularity cross-section
r_1	transmitter to scattering region distance
r_2	scattering region to receiver distance

3.2.9 Real systems

Practical systems have to achieve a compromise between such influences as the optimum design, the available financial resources and the desired geographic location. The behaviour of the resulting non-ideal systems will be illustrated in Chapter 4 where the coherent backscatter radars employed in this study will be discussed.

It is possible to measure the power and phase angle of each returned lag to good accuracy. Current radars under development can measure phase angles at a sensitivity approaching a thousandth of a radian (J. Thornhill (1993) private communication). Thus the backscatter power, Doppler shift and Doppler broadening of the returned signal can be well quantified. However, the interpretation of these parameters as an irregularity cross-section, an irregularity phase speed and a measurement of the coherence of the scattering object respectively is subject to unknown errors dependent on how well current theory can describe the irregularity behaviour. How much the measured irregularity parameters differ from their true values is a difficult problem to resolve, without independent comparative measurements.

3.3 Incoherent Scatter

The principles of incoherent scatter radar and the implementation of the technique have been extensively discussed, e.g. Evans (1969), Beynon and Williams (1978), Rishbeth and Williams (1985). Here it is sufficient to present the basic physics of the technique and describe what information can be obtained. Specific practical details will only be introduced later, as necessary.

The spatial charge distribution in a plasma is determined by the effective potential field of all the charged particles present. Calculation (e.g. such as first by Debye and Hückel, 1923) predicts the potential of a given charge is effectively screened by the induced field of the other particles at a distance from the particle greater than or equal to a distance called the Debye length 'D' where,

$$D = \sqrt{\frac{\varepsilon_o k_B T_e}{Ne^2}} \qquad (3.15)$$

D is an important scale length for a plasma, especially in relation to the wavelength of a probing electromagnetic wave.

In the ionospheric plasma the free charges consist of electrons and ions such as O^+,O_2^+ and N_2^+ (for more details see Rishbeth, 1988). The Debye length varies from about 0.3cm at the F-region peak to 6cm in the lower E-region and at altitudes in excess of 2000km (Beynon and Williams 1978). If the radar wavelength is shorter than the Debye length scatter from individual particles occurs. If the radar wavelength is greater than the Debye length the scatter is from larger scale structures. The thermal motion of the particles takes the form of ion-acoustic and electron-acoustic plasma waves. These constitute structure from which transmitted radio waves ($\lambda > D$) will scatter.

The ion-acoustic and electron-acoustic waves propagate in all directions at a variety of wavelengths. They are strongly quenched by Landau damping and thus their scattering cross-section is small (in fact, of the order of the electron cross-section, $10^{-28}m^2$). If observation is to be successful then high power transmitters and sensitive receivers are required. There are no aspect angle requirements as necessary for coherent backscatter radars. A Bragg condition for scatter will be met provided the transmitter and receiver both look into the same volume.

To illustrate the parameters that an incoherent scatter radar can measure it is instructive to refer to a schematic of a incoherent scatter spectrum drawn in Figure 3.5(a). All components of the spectrum are shifted due to the background drift of the plasma. The double-peak corresponds to ion acoustic waves propagating towards and away from the radar. The two peaks at larger Doppler shifts are due to electron acoustic waves. The position of these peaks can be measured to give directly the component of the plasma drift velocity in the line of sight of the radar, the ion acoustic speed and the electron acoustic speed.

Further information can be derived from the spectrum such as the ion and electron temperatures and the electron density. In practice, this is achieved by calculating a set of theoretical ACFs by assuming a given composition model for the ionosphere and a velocity distribution function. Each measured ACF is compared to this library of theoretical ACFs to find the closest fit. Figure 3.5(b) illustrates how features of the spectrum are related to these other derivable parameters.

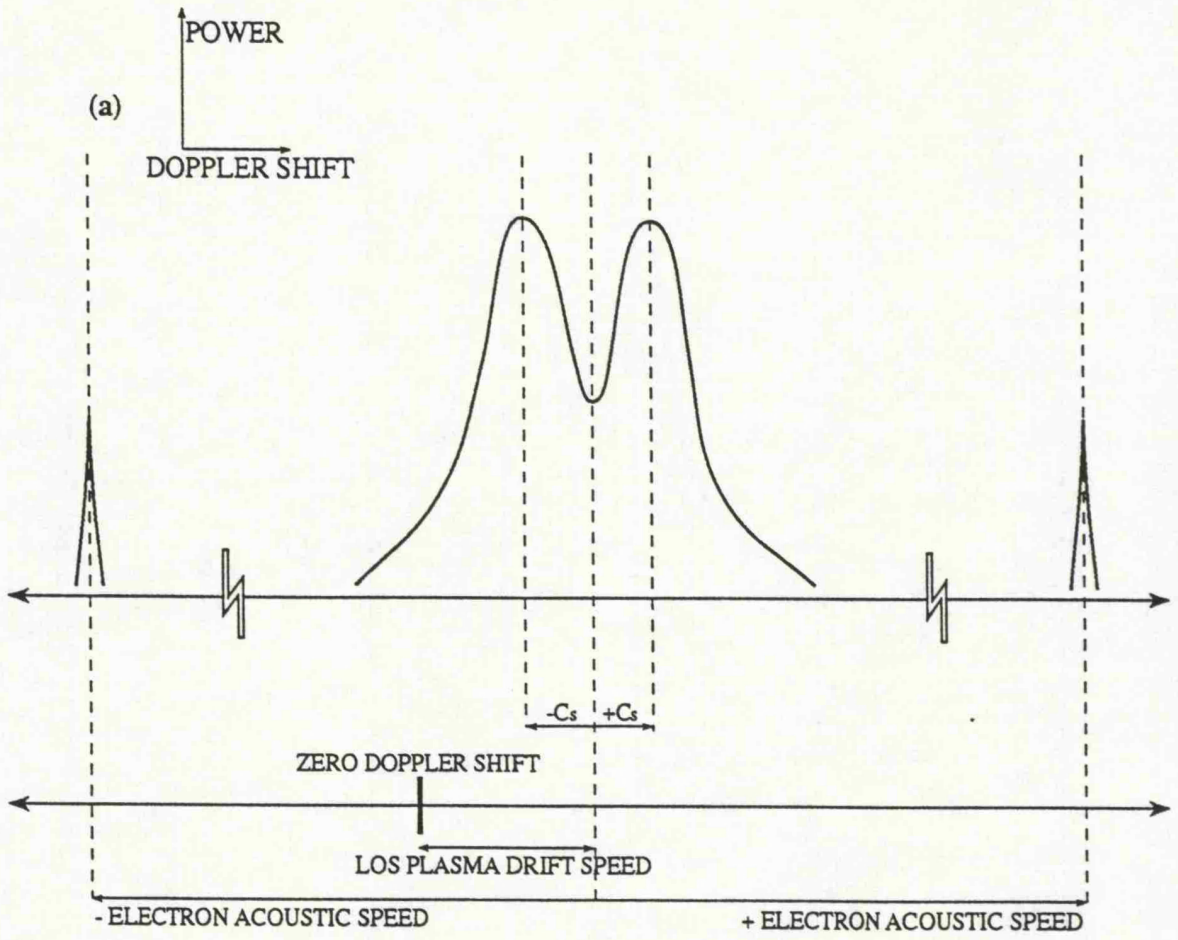

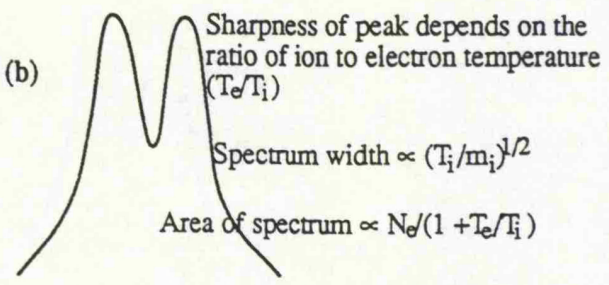

Figure 3.5 Incoherent scatter spectrum

Chapter Four

RADAR SYSTEMS

4.1 Introduction

The bulk of the data to be presented in this work originates from three coherent radar systems; the Wick radar of SABRE, the Halley radar of PACE and COSCAT. Each radar has a different operating frequency and is hence sensitive to a different irregularity wavelength. Table 4.1 summarises the operational parameters of each radar and Figure 4.1 depicts the radars' geographical locations. The following sections provide a detailed description of the important aspects of each radar.

	SABRE (Wick)	PACE (Halley)	COSCAT
Irregularity wavelength /m	1	7-20	0.16
Normal programme	Double pulse	Multipulse	Sample CW
Routine measured parameters	Power Doppler velocity	Power Doppler velocity Spectral width	Power Doppler velocity Spectral width
Range resolution/km	15	50	None
3dB point separation	50° transmit 3.2° receive	2.5° at 20MHz 6° at 8MHz	4° transmit 1.2° receive
Temporal resolution/s	20	5	5
Beam geometry	Co-located transmitter and receiver. Receive simultaneously over eight beams.	Transmit and receive on same beam. Beam electronically steered	Spatially separated transmitter and receiver.

Table 4.1

A comparison between the SABRE, PACE and Halley radar systems.

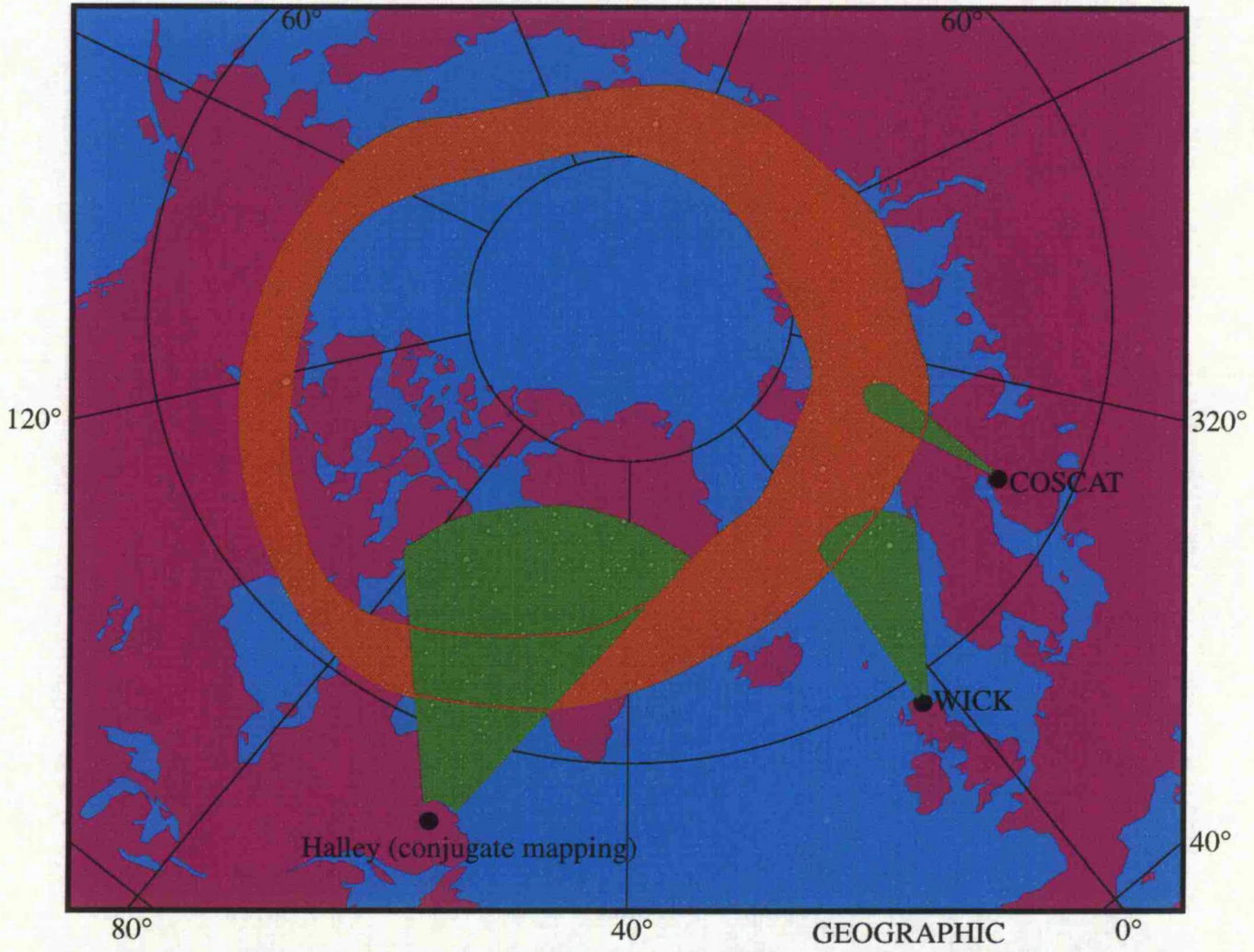

Figure 4.1 A schematic map of the fields of view and locations of the Wick, COSCAT (transmitter at Oulu) and Halley radars. The Halley field of view has been mapped along the magnetic field to its conjugate position in the northern hemisphere. Shown also, in orange, is the position of the mean auroral oval at 00.00 UT.

4.2 SABRE

The Sweden and Britain Auroral Radar Experiment (SABRE), Nielsen et al. (1983), came into operation in 1982. It consisted of two coherent radars, one located at Wick (58.4°N,-3.1°E) and the other at Uppsala (59.9°N, 17.7°E). Each radar forms an array of 16 beams that permeate a volume of the E-region between approximately L shells of four and six, illustrated in Figure 4.2. A transmitter at each site illuminates the observed volumes and the backscattered signal is received on the middle eight beams of the receiving array. Observations are restricted to the middle eight beams since these have magnetic aspect angles of 90±2°, moreover, the outer beams suffer from poor side-lobe suppression. The radars operate at slightly different frequencies, Wick 153.2MHz and Uppsala 142.6MHz, to avoid one radar detecting the signal of the other. The common viewing volume for each radar encompasses geographic coordinates of 0° to 12°E in geographic longitude and 64°N to 68°N in geographic latitude, corresponding to an area of $2x10^5 km^2$. Along each beam, 50 measurements are taken between a starting range of 495 to a final range of 1230km at a resolution of 15km. The beams are separated by 3.6° centre to centre and are 3.2° wide at the 3dB points. Routine operation consists of double pulse transmissions with an integration period of 20s. This gives measurements of backscatter power and line-of-sight Doppler velocity for a maximum of 400 range cells for each radar (8 beams x 50 ranges). In the common volume of the two radars, the line-of-sight velocities are combined to give an estimate of the plasma drift velocity, e.g. Greenwald et al. (1978).

Studies of the double-pulse data have already been undertaken, notably Mattin and Jones (1986), Mattin and Jones (1987) and Waldock et al. (1985). Additional experimental programmes that have been conducted which include EISCAT/SABRE experiments (discussed fully in Chapter 6) and SABRE spectral measurements (Mode 3 data). In many cases, the data from SABRE are from a single station only. This is because either only one station was operating or the special programme was conducted from one station only. Furthermore, in 1986 SABRE was reduced to a monostatic system, owing to the decommission of the Uppsala radar.

4.2.1 Wick spectral measurements : Mode 3 data

In this mode, the radar transmits a series of 14 double pulses with increasing separation that allows the calculation of a 15 point auto-correlation. Details of this method are reported in Schlegel et al. (1986). Due to memory limitations of the radar computer these measurements are not performed over all 400 range cells. Two procedures have been adopted in practice. Either ACFs are measured for the middle 25

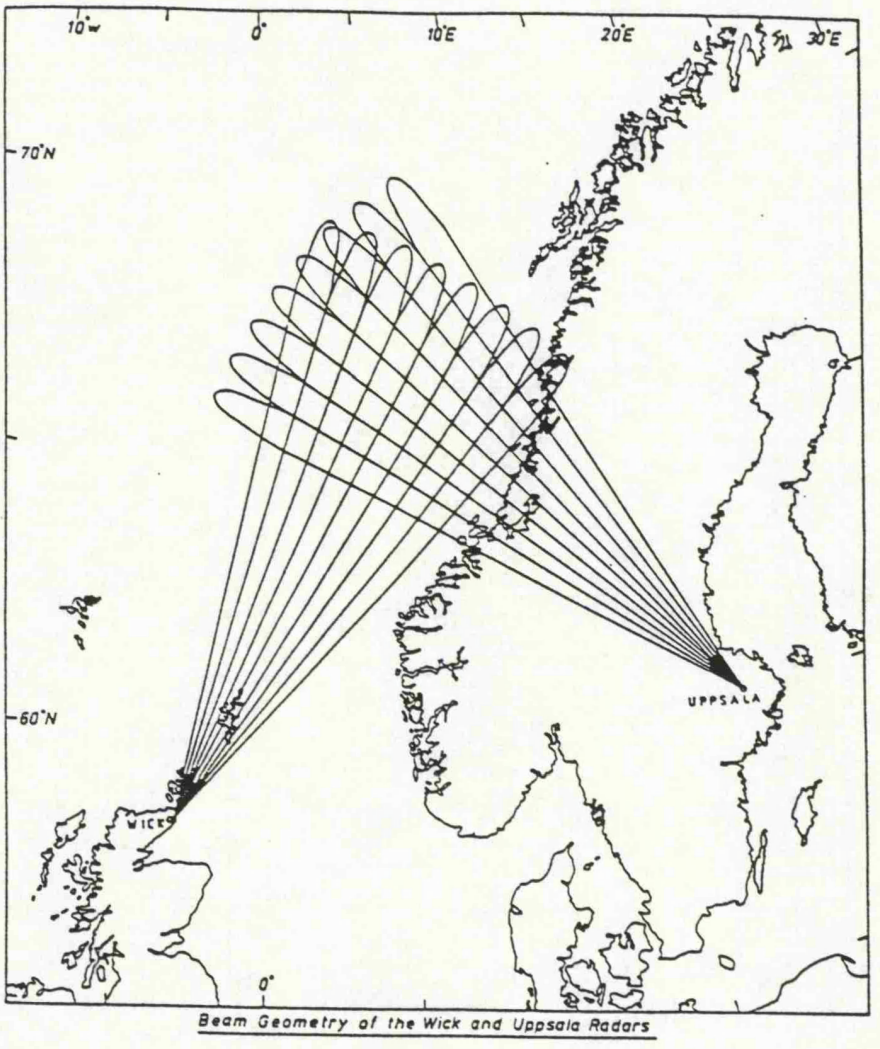

Figure 4.2 The field of view of the SABRE radar including the beam geometries of each station (After Mattin and Jones (1985)).

ranges and middle 4 beams (100pts) or the most distant 16 ranges and middle 6 beams (96pts). The ACFs are written to magnetic tape for later analysis at Leicester. Four ACFs were recorded for each beam at ranges in excess of 1400km, where no backscatter is expected, to provide a measure of the noise within an ACF. In addition to this, double-pulse measurements are available for all 400 range cells.

The data analysis involves a Fast Fourier Transform (FFT) of the ACF to give the backscatter spectrum (original code by Ridge and Schlegel (1986), incorporating a NAG algorithm). The backscatter power is calculated from the zeroth lag from the ACF. The Doppler velocity is estimated as the shift in the spectrum midway between the two half power points and the spectrum width has been taken as the full width at half maximum (cf Figure 3.4).

4.2.2 Data quality and resolution

Owing to cross-range noise the signal to noise ratio that can be achieved with the transmission of one double pulse can be no better than 3dB. For this reason, a large number of double pulses are averaged in each measurement and all resulting power measurements of less than 3dB are discarded. The power threshold on occasion needs to be set higher. This arises due to the limited dynamic range of the Wick receivers. The gain of the receiver for a given beam is set automatically in response to the highest power in that beam. If there is a large range of powers, poor estimates of irregularity parameters are obtained for those of lower power. This is overcome by setting the power threshold to be 20dB lower than the maximum power in the beam (Thomas (1993) private communication). This type of problem arises in less than 5% of the data.

Since Mode 3 operation involves the transmission of a sequence of double pulses, the noise floor for each point measured on the ACF is 3dB. In the analysis just the zeroth order lag is checked against the threshold. The integration time is extended to three times that of the double pulse technique (i.e. 60s) in order to improve the signal to noise ratio of all the lags.

For the SABRE Mode 3 data to be presented in this work, a lag spacing of 400μs was adopted. The resulting derived power spectrum has a separation between individual points of 78Hz. A frequency shift (Δf) can be converted to a Doppler shift in velocity (Δv) through the expression:

$$\left|\frac{\Delta f}{2f_{transmitter}}\right| = \left|\frac{\Delta v}{c}\right| \qquad (4.1)$$

For Wick this gives a point to point resolution of 78m/s. The minimum spectral width that can be resolved is half the point to point separation, i.e. 39m/s.

4.3 Halley

Halley is one of two HF coherent backscatter radars that comprise the Polar Anglo-American Conjugate Experiment (PACE), Baker et al. (1989). Halley is located at 76°S, 27°W in Antarctica. The other radar is at Goose Bay in Labrador at 53°N, 60°W. The field of views of each radar encompass regions of the same magnetic local time and opposite geomagnetic latitudes. PACE makes it possible to investigate conjugate behaviour of geophysical processes in the ionosphere of the Earth's Northern and Southern Hemispheres. However, this is a difficult task, since the configuration of the geomagnetic field is very variable, especially at high latitudes due to the coupling between the ionosphere, magnetosphere and solar wind.

Goose Bay has been described in Greenwald et al. (1985) and the Halley radar is similar. It consists of an array of 16 broad band log-periodic antennae employed for both transmitting and receiving. The signal produced by each antenna is phase shifted in order to produce a single beam. The beam can be electronically steered to point in any one of 16 directions separated by 3.3°. A seven pulse sequence is transmitted which allows the determination of a 17 lag ACF. Typically, the radar integrates the signal for 6s, collecting data for 50 ranges at an approximate resolution of 50km. The controlling hardware allows real time manipulation of the radar parameters such as frequency and pulse length. Early memory limitations resulted in only the top 20 powers measured along the beam being recorded for each integration period. New hardware development has surmounted this constraint. Scanning the beam through all pointing directions allows large spatial maps of irregularity parameters to be constructed every 96s which is the time taken to sweep the field of view. Halley operates in the HF band from 8 to 20MHz and can observe both in the E- and the F-regions. The E-region observations tend to be restricted to the first 10 ranges accessible to the radar. Further ranges are filled with observations from F-region altitudes. The effect of HF propagation on determining the location of the coherent echoes has been studied by Villain et al. (1985) with the Scandinavian and French Auroral Radar Investigation (SAFARI) and EISCAT. Errors in the positioning of backscatter returns, when no electron density information was available, were postulated to be of the order of a few tens of kms. This error will increase when tilts and gradients in the electron density are present as is often the case in the auroral zone ionosphere.

The data to be presented in this work predates the hardware developments that obviated the memory limitations. Only E-region observations have been utilised and were obtained by selecting just the first six ranges of observation.

Data analysis relies on study of the ACF and the standard technique for analysing the PACE data has been described in Villain et al. (1987). The method estimates the backscatter power, irregularity phase speed and spectral width. Errors in the parameters arising from the fitting technique are typically no greater than 5%. The point to point separation in a Doppler spectrum is typically 60m/s.

4.4 COSCAT

The COherent SCATter experiment (COSCAT) is an innovative coherent radar system created by adding a 500W transmitter to the EISCAT facility. The project is a joint initiative between the Max-Planck-Institut für Aeronomie, The Ionospheric Physics Group at Leicester and the Physics Department of the University of Oulu. Figure 4.3 illustrates the observing geometry of the transmitter (positioned at Oulu (64.97°N, 25.67°E)) and the EISCAT receivers. The radar illuminates a volume of the E-region where it is calculated that the EISCAT receivers can obtain pointing directions close to orthogonal to the magnetic field. A detailed description of the COSCAT system is given in McCrea et al. (1991).

COSCAT undertakes two modes of operation termed PASSIVE and ACTIVE. In PASSIVE operation the EISCAT receivers act as passive detectors of the signal transmitted from Oulu and scattered from the irregularities. The receivers can observe a fixed point or make spatial scans in azimuth and elevation. In ACTIVE experiments, the EISCAT transmitter at Tromsø illuminates a volume of the ionosphere and the incoherent scatter technique provides measurements of other plasma parameters in conjunction with the irregularity measurements. Results from PASSIVE and ACTIVE experiments will be found in Chapter 5 and Chapter 7 respectively.

The EISCAT receivers record ACFs of the backscattered signal. A typical procedure, as for example applied to PASSIVE experiments, is for four signal ACFs and a noise ACF to be recorded on two channels of each receiver. The noise ACFs are subtracted from the signal ACFs. The ACFs from each channel are added to reduce system noise that is uncorrelated between the two channels and then integrated for a period of 5s. In Leicester, the ACFs are converted to spectra and the moments of these are estimated from which irregularity parameters are derived. Errors in the estimation of irregularity parameters, arising from the analysis technique, are no greater than 2%.

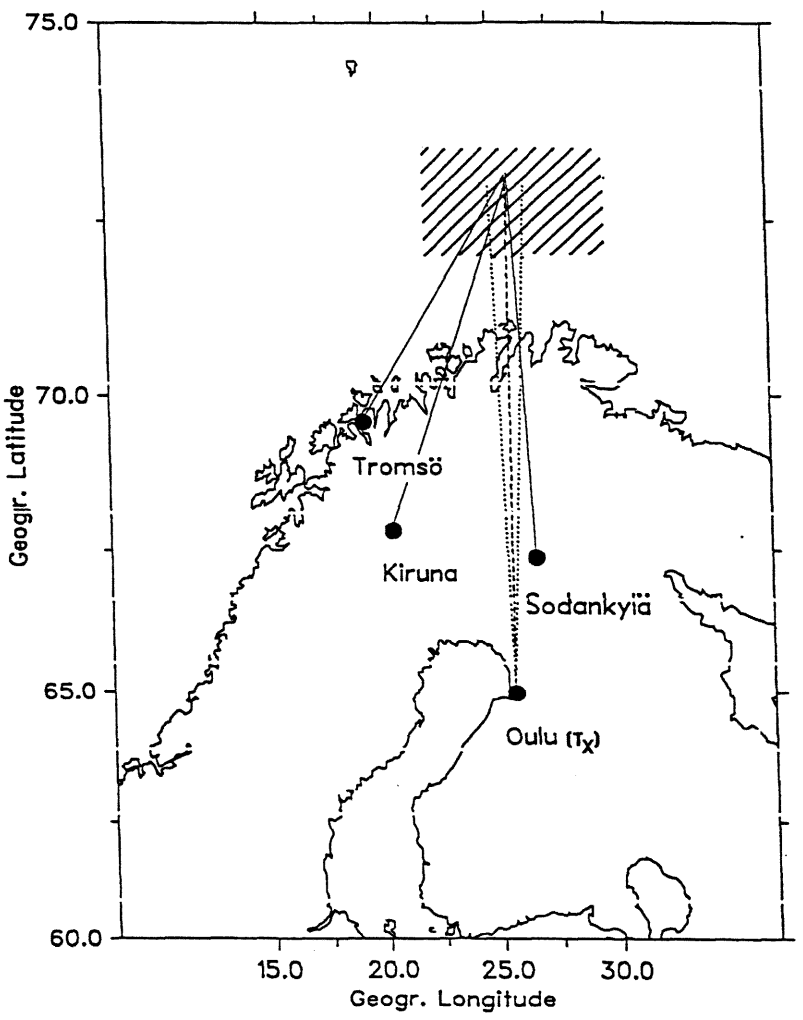

Figure 4.3 The geometry of the COSCAT experiment. In PASSIVE experiments the three EISCAT receivers are oriented to detect the signal transmitted from Oulu scattered by E-region irregularities.

Chapter Five

OBSERVATIONS OF RADAR SPECTRA

5.1 Introduction

Observations of E-region spectra with SABRE, COSCAT and PACE (Halley) are presented and discussed. The backscatter spectra have been characterised by their spectral moments as described in Chapter 3. A statistical study of the spectral moments of each radar has been conducted and comparisons made between the results obtained from the different radars. This gives insight into the variation of irregularity parameters due to changes in radar wavelength and the geophysical observing conditions. A study of the relationships between the principal spectral moments at a fixed wavelength has also been undertaken.

Schlegel et al. (1986) carried out a statistical study of the spectral data observed at Wick in 1984. In the present study, the spectral data have been extended beyond that available to Schlegel in two ways. Firstly, simultaneous double pulse data were available from Uppsala for part of the observing time (1986 day 72). This enabled the flow angle to be estimated during these periods. Secondly, for one Mode 3 campaign EISCAT data from above the SABRE field of view were available (see Chapter 6). The first results from the COSCAT experiment were discussed by McCrea et al. (1991). In this thesis further results are reported that have significantly expanded the original data set, allowing the general properties of 16cm wavelength irregularities to be more clearly established. Furthermore, experiments that include the simultaneous measurement of incoherent scatter data with EISCAT are discussed in Chapter 7. Studies of E-region data with the PACE HF radar have been made, notably Villain et al. (1987) and Villain et al. (1990). However, Villain's work consisted of observations in the Northern hemisphere from Goose Bay. Statistics for the Antarctic PACE radar located at Halley are presented here.

5.2 Backscatter statistics

5.2.1 Occurrence of backscatter

The diurnal distribution of backscatter for each radar has been established by evaluating the total number of backscatter occurrences for every hour of Universal Time in the day. An occurrence is defined as sufficient integrated signal, returned from the

ionosphere, that has a power greater than the noise threshold for the radar. Histograms of the number of occurrences in each hour are displayed in Figure 5.1.

The Wick histogram (Figure 5.1(a)) is compiled from approximately 100hrs of Mode 3 observation from all points in the field of view. The data originates from two periods: (1) from 1986 day 8 12:34UT to 1986 day 14, 03:32UT and (2) from 1986 day 59, 12:33UT to 1986 day 73, 19:05UT. No irregularities were observed between 05.00 to 11.00UT. Occurrences maximise around 17.00 to 20.00UT and then fall to a local minimum between 21.00 and 22.00UT. The spectral data statistics for Wick can be compared with the occurrence statistics for the Wick double pulse data, Figure 5.1(b). The double pulse statistics consist of minute averages, for one point in the Wick field of view, taken over a period of 8 years. In these data, the period from 05.00 to 11.00UT of no spectral observations corresponds to a broad minimum in the number of returns. Otherwise the form of the spectral backscatter histogram is similar to that for the more abundant double-pulse data.

In assessing the COSCAT observations, Figure 5.1(c), the distribution in time of radar operation must be taken into account. This is plotted on the histogram as a contiguous line. Most COSCAT occurrences arise during two intervals 01.00 to 04.00UT and 15.00 to 17.00UT. There is a distinct minimum between 17.00 and 20.00UT. No significance can be attributed to the broad minimum between 05.00 and 12.00UT since COSCAT never operated during this period of the day. In Figure 5.1(d) the number of backscatter occurrences have been divided by the minutes of observation in the same hour and the total distribution has then been normalised. This reveals the maximum in coherent scatter occurrence at 15.00 to 16.00UT is exaggerated by the number of observations in that hour. The backscatter occurrence maximum is between 14.00 and 15.00UT. There is a second maximum between 01.00 to 04.00UT.

The Halley histogram, Figure 5.1(e), contains data taken from 9 months of continuous observation. These data were available in a condensed data-base created by Leonard (1991). The diurnal distribution of the E-region Halley data, contains a large asymmetry in the number of occurrences before and after 12.00UT. More irregularities are observed between 00.00 and 12.00UT than in the remaining 12 hours of the day. This is a result of the experimental programme executed at Halley and does not reflect any physical property of the irregularities. The radar operating parameters are usually altered at noon so that the radar field of view follows the expected location of the auroral oval. This feature has been incorporated into the radar operation since it is thought that the location of backscatter is coincident with the position of the auroral oval (e.g. Tsunoda et al., 1976). One result of this policy is to bias the measurements

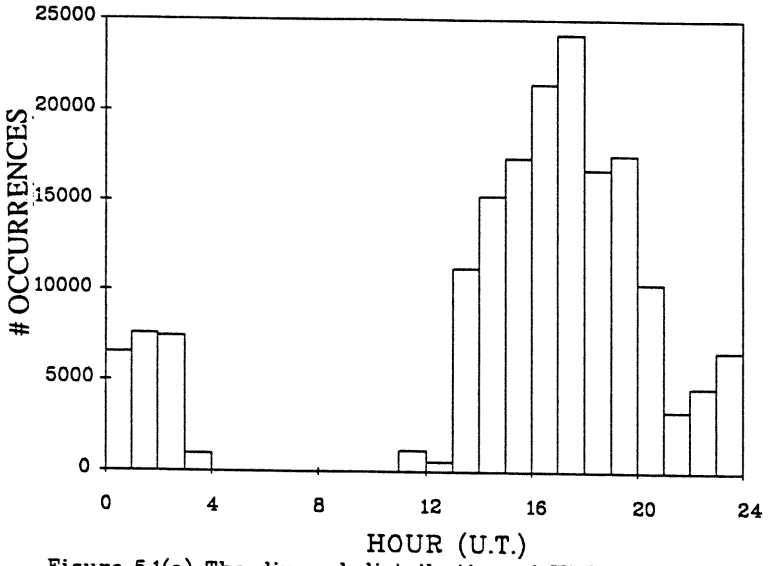

Figure 5.1(a) The diurnal distribution of Wick spectral observations.

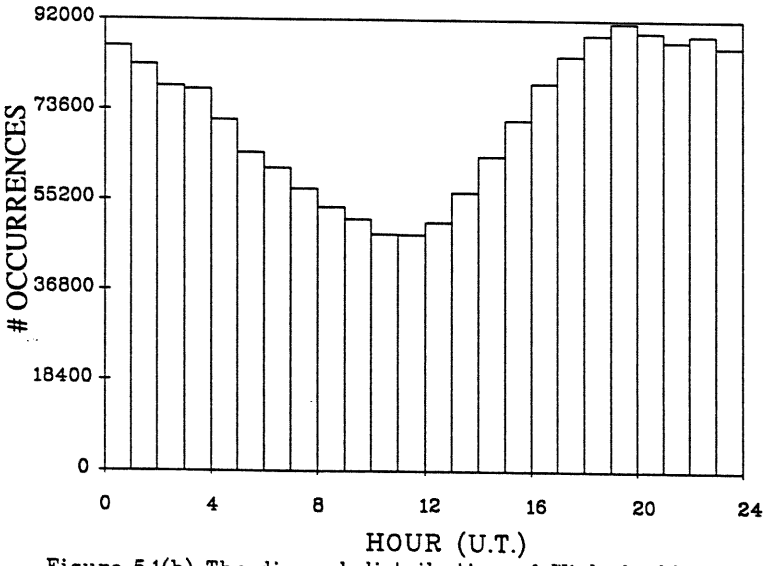

Figure 5.1(b) The diurnal distribution of Wick double-pulse observations.

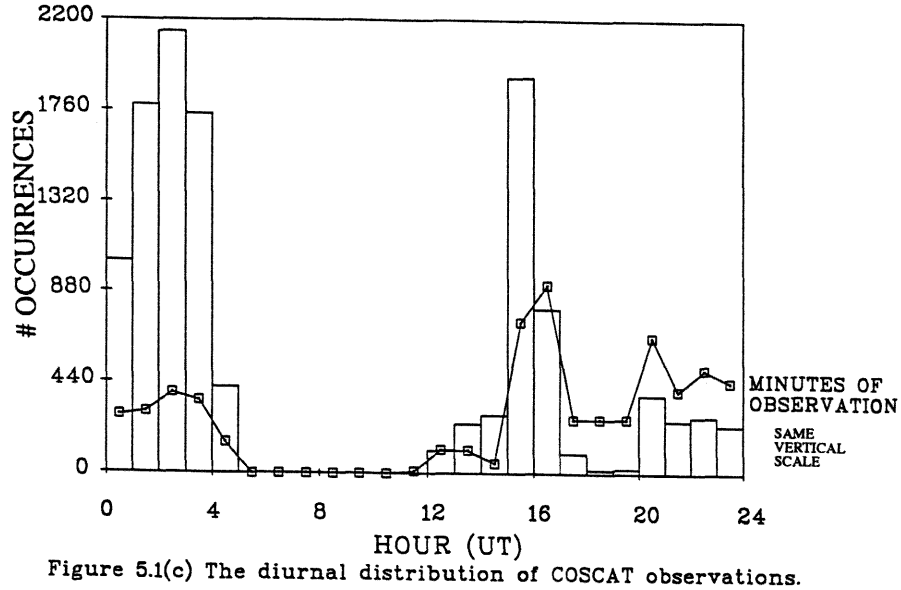

Figure 5.1(c) The diurnal distribution of COSCAT observations.

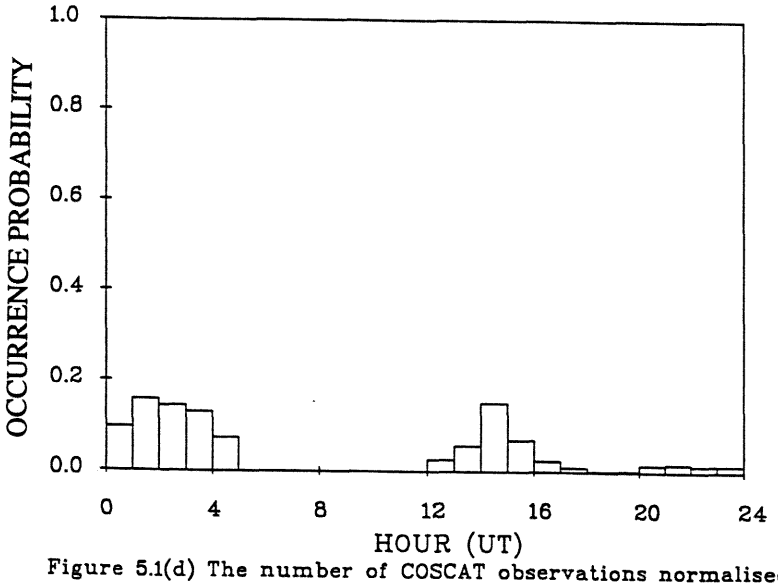

Figure 5.1(d) The number of COSCAT observations normalised with respect to minutes of radar operation.

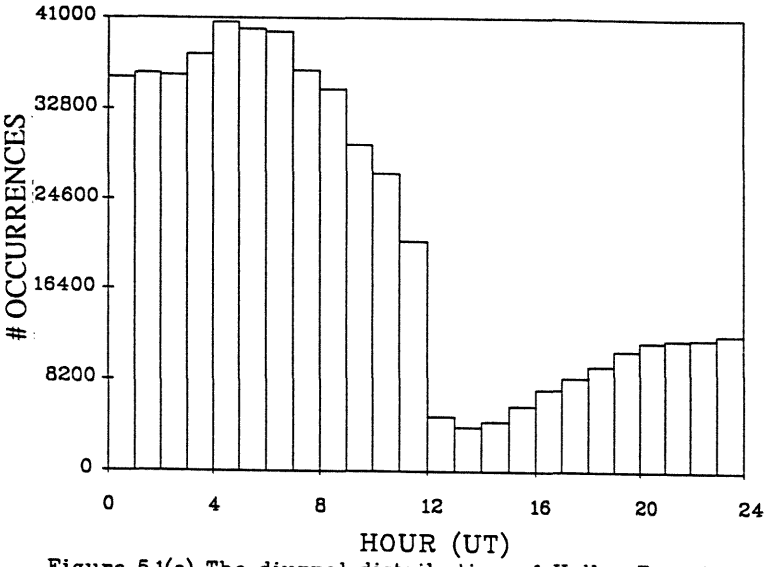

Figure 5.1(e) The diurnal distribution of Halley E-region observations.

towards fewer observations of E-region spectra in the afternoon. With this asymmetry in mind, the Halley histogram exhibits a broad minimum in occurrence centred about 13.00UT. The possibility of a further minimum exists between 00.00 and 03.00UT.

The following table summarises the temporal location of the minima in each histogram.

	Broad minima		Narrow minima	
WICK	05.00 - 11.00 UT	04.40 - 10.40 MLT	22.30 ±1.00 UT	24.00 ± 1.00 MLT
COSCAT	no observations	no observations	18.30 ±1.00 UT	22.00 ± 1.00 MLT
HALLEY	13.30 ±1.00 UT	09.30 ± 1.00 MLT	0.00 - 03.00 UT	21.00 -24.00 MLT

Table 5.1

The time of each minimum is measured from the histograms in universal time. In Table 5.1 these have been converted to the magnetic local time in the middle of the radar's field of view. In some cases it is not possible to identify the centre of a minimum and a range of times is given. The minima occur during similar periods of magnetic local time for each radar.

The next sections discuss the statistics of the three principal spectral moments, which constitute the backscatter power, phase speed and spectral width. The nature of the background plasma convection pattern (see Section 1.5) determines two distinct regimes during which backscatter observations are made. Namely when the plasma drift is predominantly in an east-to-west direction or a west-to-east direction. For the Wick and COSCAT data positive Doppler shifts (V>0) in the coherent scatter returns correspond to east-to-west plasma flow while negative Doppler shifts correspond to west-to-east plasma flow. Thus, in subsequent analysis, the two Doppler shift regimes are considered separately. However, for the Halley radar, the beam look directions are close to perpendicular to the plasma flow direction, this makes it impossible to unequivocally determine the direction of the plasma flow from the sense of the coherent scatter Doppler shift for the Halley data.

5.2.2 Backscatter Power

The histograms of backscatter power for each radar, Wick, COSCAT and Halley are illustrated in Figure 5.2(a). The power distributions are skewed and Gaussian in shape. Most occurrences are at low powers, while there is an extended tail of fewer backscatter observations at higher powers. Calculation of the mean observed powers

Figure 5.2(a) Histograms of backscatter power on a dB scale specific to each radar.

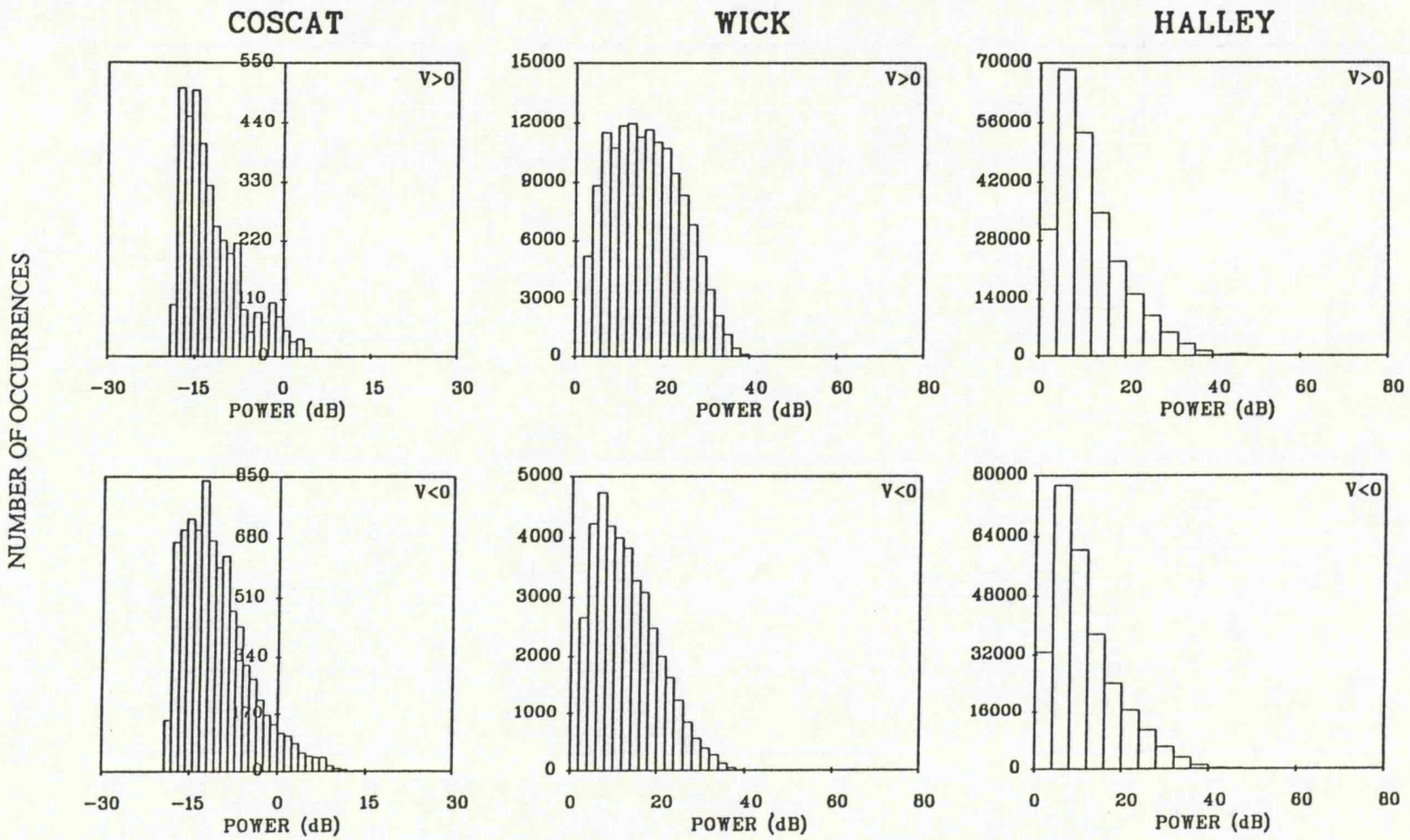

and the root-mean-square deviation of the data about this mean, gives the following values:

RADAR	POWER/dB	
	V>0	V<0
COSCAT	-12 ± 5	-11 ± 6
WICK	17 ± 8	14 ± 8
HALLEY	11 ± 8	11 ± 7

Table 5.2

The entries in the table are the mean power observed and the standard deviation of the observations, the later tables for phase velocity and width follow this format. V>0 and V<0 refer to the sign of the coherent scatter Doppler shift.

5.2.3 Phase velocity

The Wick and COSCAT phase velocity histograms are similar. They are characterised by two distributions in each flow regime, Gaussian in shape, centred about ± 400m/s and of the same width. The calculated mean values are given in the following table:

RADAR	PHASE VELOCITY (m/s)	
	V>0	V<0
COSCAT	340 ± 160	-360 ± 150
WICK	460 ± 160	-420 ± 150
HALLEY	220 ± 310	-180 ± 290

Table 5.3

Further to this, the COSCAT data contain a number of spectra at around zero Doppler shift. Some of these results arise due to observed backscatter at zero velocity that were later identified with tropospheric scatter directly from the Tromsø transmitter. At other times double peaked spectra, with components at ± Doppler shift were observed, e.g. the spectrum in Figure 5.3. In moment analysis of such spectra, the two peaks are not resolved and a velocity estimate near zero is obtained.

The Halley phase speed observations are markedly different to those of COSCAT and Wick. 50% of Halley occurrences are at a phase speed of less than 200ms^{-1}. The number of occurrences decreases rapidly at higher velocities. This pattern is true for

Figure 5.2(b) Histograms of irregularity phase speed.

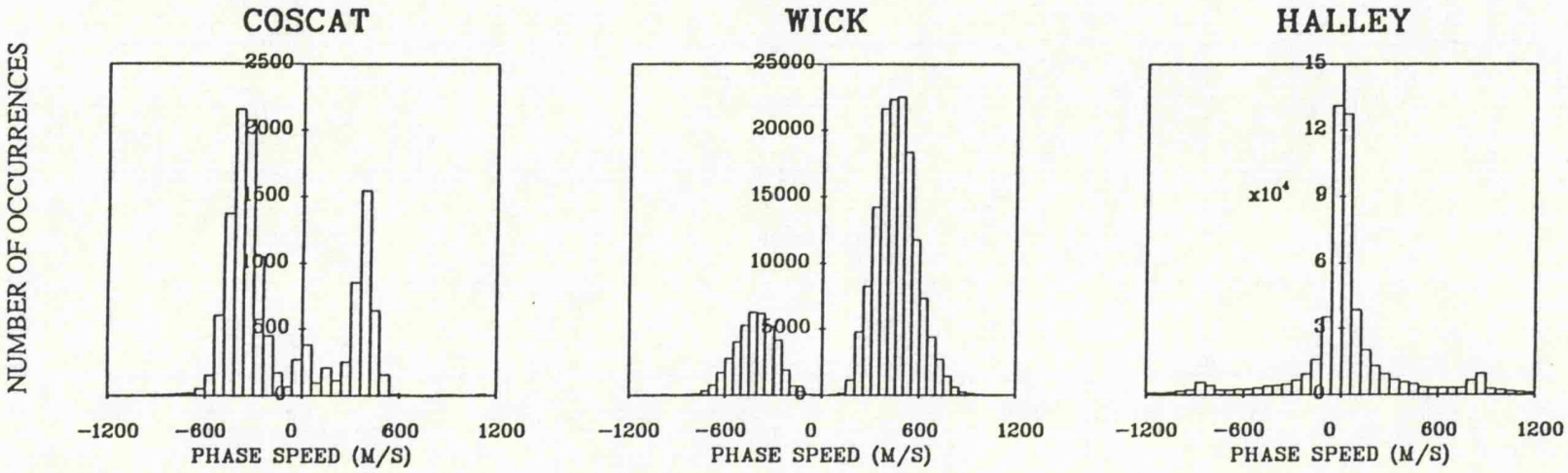

both positive and negative Doppler shifts. In addition there are localised peaks in the number of occurrences at ± 900m/s.

5.2.4 Spectral width

Spectral width statistics are given in the following table, the histograms for each radar appear in Figure 5.2(c).

RADAR	SPECTRAL WIDTH (m/s)	
	V>0	V<0
COSCAT	250 ± 190	300 ± 120
WICK	280 ± 360	320 ± 200
HALLEY	130 ± 130	130 ± 130

Table 5.4

An asymmetry between the occurrences for each flow regime is evident for the Wick and COSCAT radars. The mean spectral width is smaller (approximately 85%) for the (V>0) regime than for (V<0). Other differences are evident by looking at the shape of the histograms. In the case of the Wick data set studied by Schlegel et al. (1986), the spectral width histogram was narrower for positive Doppler velocity than for negative Doppler velocity. The same is true throughout data sets for both Wick and COSCAT. Taking the full width at half maximum for each histogram (Halley included) results in the following figures:

FWHM of Histogram/ms^{-1}	COSCAT	WICK	HALLEY
V > 0	60	150	125
V < 0	160	275	125

Table 5.5

The table gives the width at half maximum (in m/s) for each of the spectral width histograms of Figure 5.2(c).

There is a greater spread in the measured width for observations during west to east plasma drift (V<0) conditions. The standard deviation results (Table 5.4) do not suggest this, the standard deviation of the data about the mean is greater for the (V>0) cell than the (V<0) cell. This is a result of the long tail on the (V>0) spectral width distribution. The Halley histograms of spectral width do not exhibit any asymmetry with respect to the sign of the Doppler shift.

Figure 5.2(c) Histograms of spectral width.

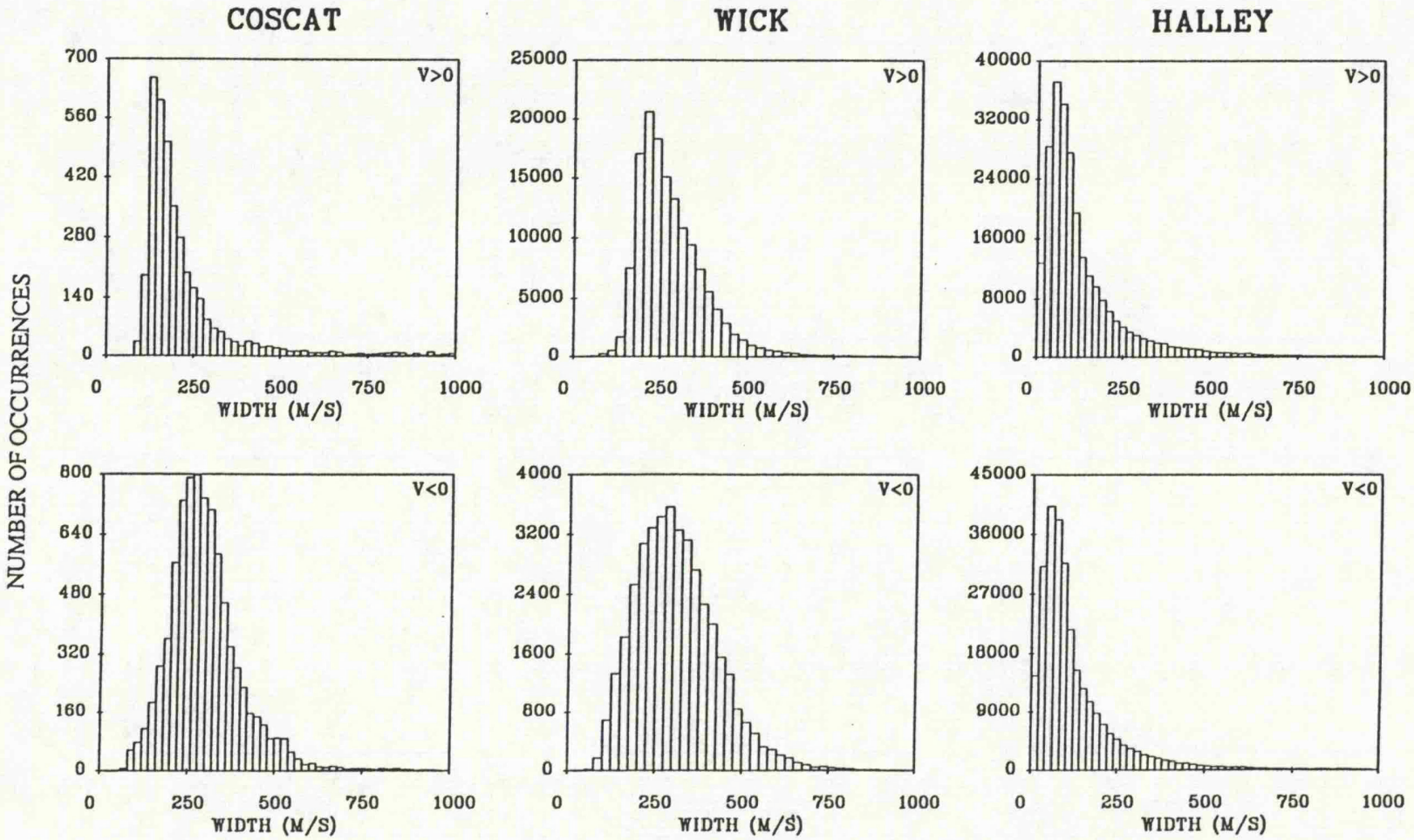

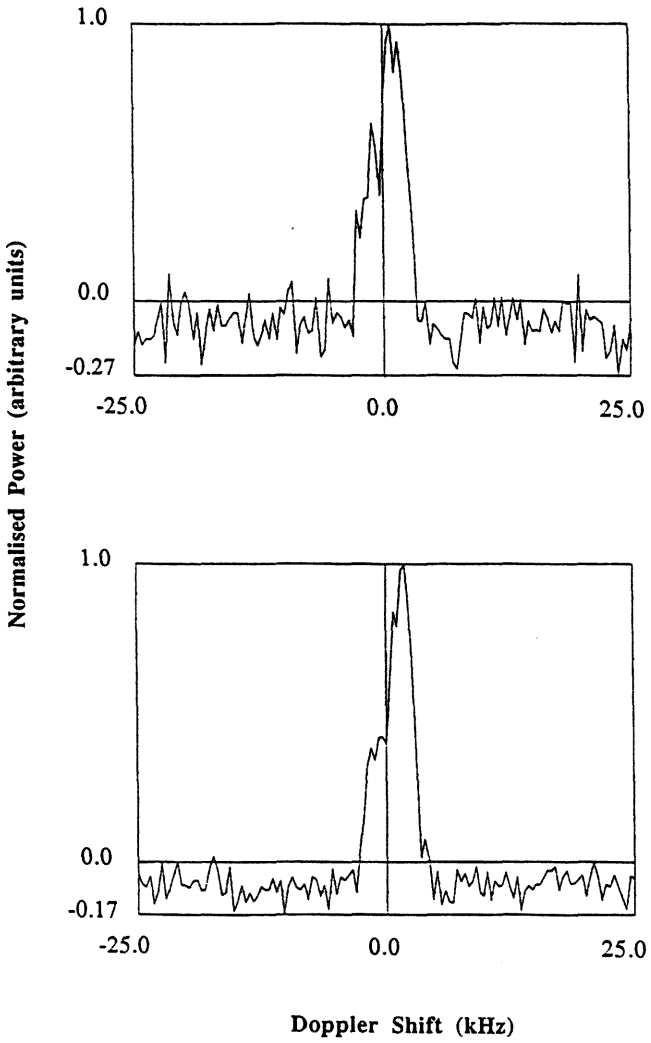

Figure 5.3 Coherent scatter observed over the Oulu - Kiruna path. These spectra, from the experiment of the 13/03/91 at 01:41:50 UT (top) and 01:40:30 UT (bottom), exhibit a double-peaked shape.

5.2.5 Irregularity types observed

The Wick and COSCAT statistics are consistent with the observation of Type (I) irregularities. The spectral width is smaller than the mean Doppler shift, which is of the order of the ion-acoustic speed. In contrast, the Halley radar detects low phase speed Type (II) irregularities. The reasons for the different observations between each radar system are likely to have a geophysical origin. The orientation of the Halley radar is such that the radar beams point close to perpendicular to the direction of the local L-shells. Thus observations are predominantly perpendicular to the plasma flow direction. This results in the observation of gradient drift irregularities propagating at velocities that are a small component of the plasma drift velocity. Under these circumstances Type (I) irregularities could only be detected during conditions of high plasma flow speeds when the maximum angle at which irregularities could be excited in a plane orthogonal to B is enlarged. Under such strongly driven conditions an elevation in the local ion acoustic speed would be expected and the phase speed of the irregularities would be large. This could account for the two peaks in the Halley phase speed distribution at ±900m/s, Figure 5.2(b). In comparison, Wick and COSCAT observe irregularities at smaller angles to the flow and are thus sensitive to Type (I) irregularities at lower phase speeds.

5.3 The behaviour of the spectral width with respect to other irregularity parameters

In this section, a study is made of the relationship between the spectral width and the irregularity parameters of wavelength, backscatter power and phase speed. Statistics and comparisons to various theoretical models are also presented here. The sections that concentrate on the inter-relationships between the spectral width and other spectral moments are based on statistics compiled chiefly from the Wick spectral measurements. Where possible, the study made with the Wick data is compared with similar measurements from the COSCAT and Halley data sets.

5.3.1 The relationship between spectral width and wavelength

Multifrequency studies of irregularities were initially undertaken by Leadabrand (1964), who measured the wavelength dependence of backscatter power with a coherent radar in Fraserburgh, Scotland. Studies of the wavelength dependence of spectral width were first conducted in the equatorial electrojet by Balsley and Farley (1971), who measured irregularities at radar frequencies of 16, 50 and 146MHz. They were unable to make any definitive conclusions concerning spectral width. All their

16MHz data consisted of spectra that were composites of Type (I) and Type (II) irregularities. Their observations at 50 and 146MHz indicated that the frequency widths were consistently larger at the higher wave number. Hanuise and Crochet (1981b) made spectral measurements at radar frequencies of 30 to 300MHz and fitted a power law to the relationship between width and irregularity wave number of the form k^n and found an index n = 0.7.

The average spectral width calculated from all the available data has been established for the Wick, COSCAT and Halley radars. Further to this a mean spectral width observed at a radar frequency of 398MHz has been deduced from the work of Moorcroft and Tsunoda (1978). Figure 5.4 is a $\log_e$-$\log_e$ plot of the spectral widths in Hertz against the irregularity wave number (per metre). This yields a power law with n = 1.2 ± 0.4.

5.3.2 The relationship between spectral width and irregularity backscatter power

Figure 5.5 is a plot for the Wick spectra of irregularity power against the spectral width, calculated as the full width at half maximum in metres per second. Maximum powers occur for spectral widths just below 200m/s. Each side of this point, there is a strong boundary defined by the maximum power at any given width. This behaviour is also displayed in a plot of the average power in 50m/s velocity bins as displayed in Figure 5.6. After the peak in power at 200m/s width, there is a monotonic decrease in the power. Before the peak, the increase in power is more rapid. Straight lines can be fitted to each boundary, corresponding to the limiting measured power at each spectral width. It is found:

before peak	$y = 0.074x - 7.4$	(5.1)
after peak	$y = -0.005x + 5.0$	(5.2)

where 'y' is the logarithm to base 10 of the signal-to-noise-ratio and 'x' the width in metres per second.

The strict definition of the power, as the zeroth order spectral moment, is:

$$P = \int_{-W}^{W} F(\omega')d\omega' \qquad (5.3)$$

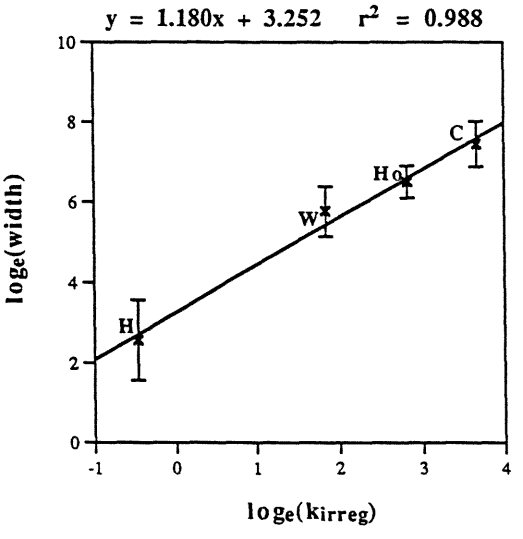

Figure 5.4 A log-log plot of the average spectral width for Halley (H), Wick (W), Homer (Ho) and COSCAT (C) plotted against the irregularity wavenumber. The Homer width is deduced from the work of Moorcroft and Tsunoda (1978). A linear fit, performed on these data, is included.

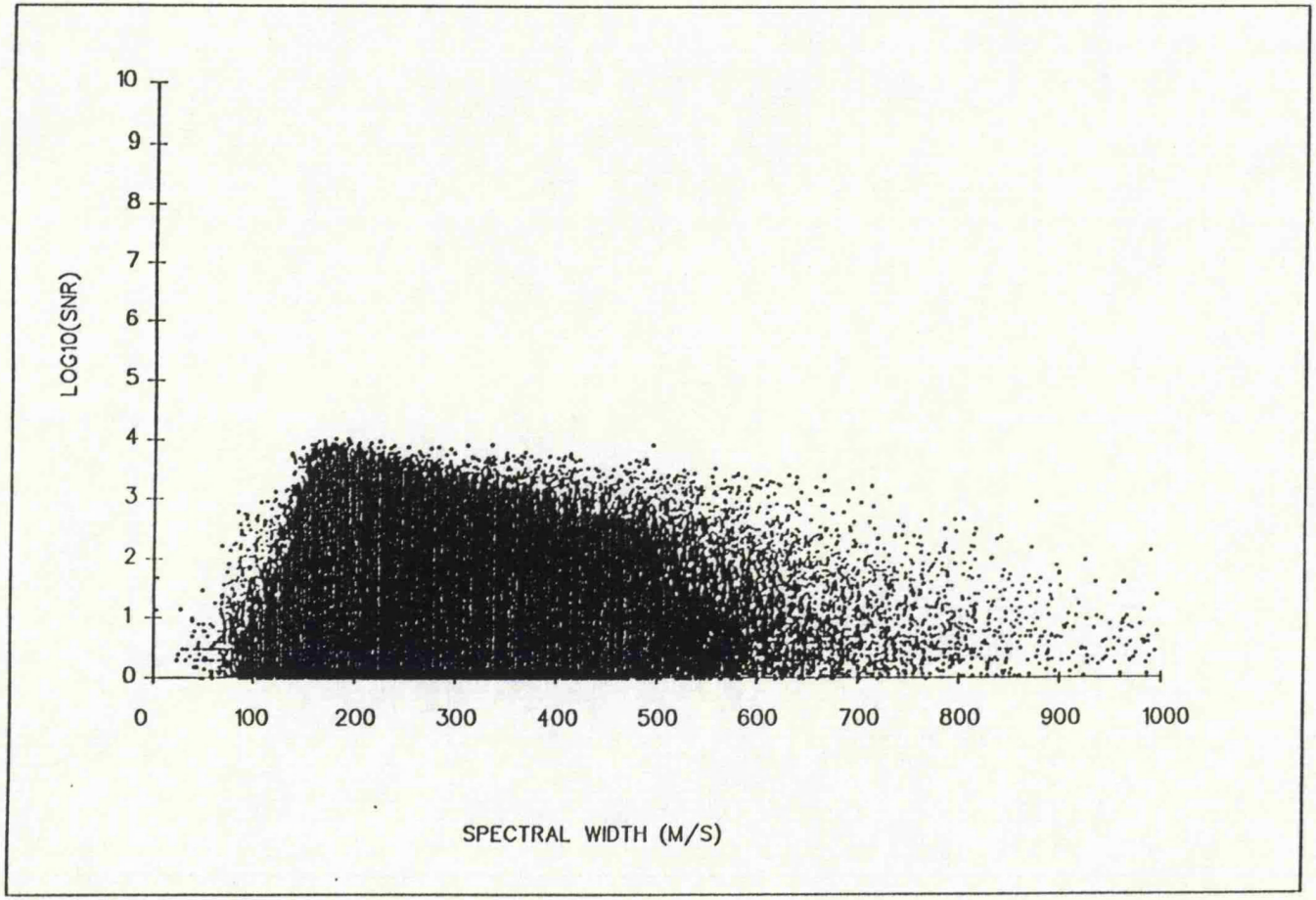

Figure 5.5 A plot of backscatter power against spectral width for the Wick radar

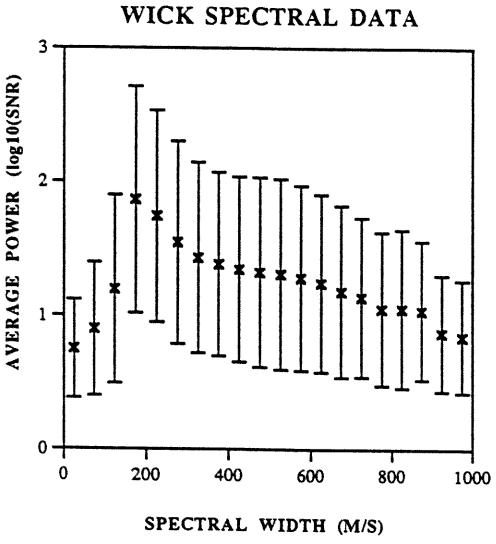

Figure 5.6 The variation of power with spectral width.

F(ω′) describes the spectrum in the frequency interval [-W,W]. The width of this interval '2W' is equal to the reciprocal of the smallest lag period in the pulse sequence transmitted. If the spectrum is lifetime broadened, see Section 2.5.1, F(w′) is defined as a Lorentzian in accordance to Equation 2.11 with a full width at half maximum equal to 2γ. Integration of 2.11 following 5.3 results in an expression for the power as:

$$P = 2\phi_0\left[\tan^{-1}\left(\frac{\omega+W}{\gamma}\right) + \tan^{-1}\left(\frac{\omega-W}{\gamma}\right)\right] \qquad (5.4)$$

This demonstrates that a relationship between the power and spectral width is expected. This function (Equation 5,4) is plotted in Figure 5.7, with $\omega=300s^{-1}$ and $W=1250s^{-1}$, which are typical values for Wick spectral mode operation. The curve illustrates a decrease in power as the width increases. This is similar to the behaviour of the data in Figure 5.6 above spectral widths of 250m/s.

However, power is not usually estimated by calculating the area under the backscatter spectrum. For Wick it is estimated by taking the power of the zeroth lag in the returned signal, essentially a single pulse method. This can then be divided by a noise figure for each beam, to give a signal-to-noise-ratio. Equation 2.1 then implies that the power is equal to ϕ_0. For a single irregularity this contains no information regarding the temporal evolution of the irregularity and it is unreasonable to assume this has any relationship to the width. The existence of a relationship suggests that a study of the effect of multiple scatterers be undertaken. Each measurement may consist of the summation of the power backscattered from a host of irregularities at different states of growth and decay, each with different amplitudes and growth rates. For the general case the received power is a sum of the form:

$$P_r = \sum_{i=1}^{N} \phi_i e^{-t_i\gamma_i} \qquad (5.5)$$

This model calculates the power as being the sum of the contributions from N irregularities in the scattering volume. ϕ_i and γ_i are the amplitude and growth rate of the ith irregularity which is at a time t_i in its evolution. Under the assumption that all the irregularities in the scattering volume have the same maximum amplitude ϕ the received power as a function of growth rate can be written as:

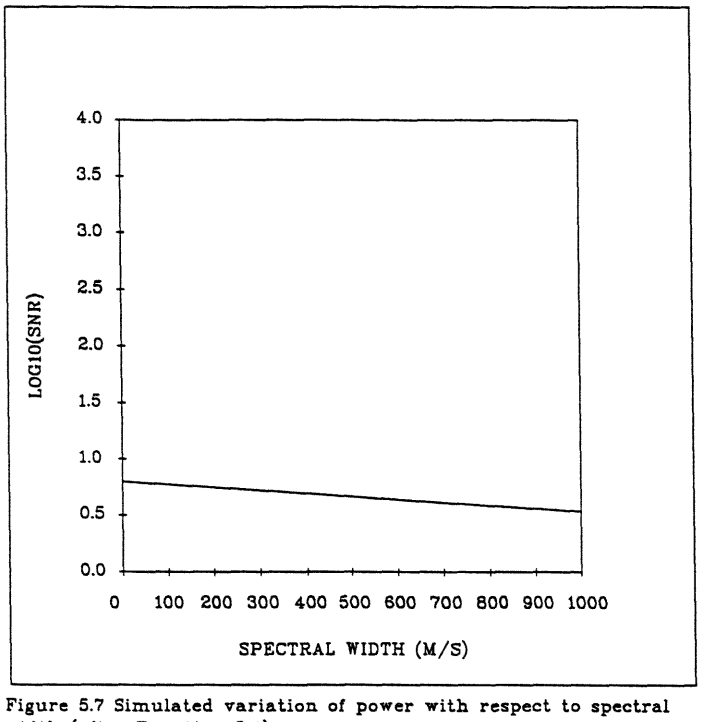

Figure 5.7 Simulated variation of power with respect to spectral width (after Equation 5.4).

$$P_r(\gamma) = \phi \sum_{n=1}^{N} e^{-(n-1)\tau\gamma} \qquad (5.6)$$

Here t_i has been substituted by $(n-1)\tau$. τ is the spacing between successive radar pulses and thus simulates the sampling rate of the radar. n is the new index to sum over. Provided $|e^{-\tau\gamma}| < 1$ then 5.6 is a convergent sum as N tends to infinity. Calculating this sum gives:

$$P_\infty = \frac{\phi}{1 - e^{-\tau\gamma}} \qquad (5.7)$$

This is plotted in Figure 5.8 with ϕ taking the arbitrary value of 10 and τ was chosen to equal 0.0004 so that increments in 'n' corresponded to successive lags, 400μs apart, of the radar signal. The model can be compared to the data if it is assumed that the growth rate corresponds to the spectral width of the irregularity observation. Consequently, in Figure 5.8 the data from Figure 5.6 is superposed. The model exhibits good agreement with the data except for low widths (<250m/s). Here the model power values increase and tend to infinity as the width goes to zero. The measured power values fall as the width goes to zero. This is an instrumental effect. Firstly, the maximum power observed is limited by the receiver. Secondly, spectra with widths less than 39m/s are not observed since this is the limiting resolution for spectral width measurements.

5.3.3 The relationship between spectral width and irregularity phase speed

The average spectral width for Wick binned in 100m/s intervals of irregularity phase speed is plotted in Figure 5.9. The error bars denote the standard deviation of each distribution of widths. Positive Doppler shifts exhibit a minimum in the spectral width in the 400 to 500m/s phase velocity bin with approximately symmetric behaviour either side. About the minimum the error bars are smaller than the point-to-point variation indicating that the minimum is a statistically significant effect. No such behaviour exists for negative Doppler shifts; here the average widths are constant just above 300m/s for Doppler shifts from -200 to -600m/s. At the peripheries of the graph +/-1000m/s there are little data (see histogram in Figure 5.2(b)) and little significance can be applied to these points.

In Figure 5.10 a subset of the data is plotted, from the spectral measurements taken from 1986 between day 70 and 73 at Wick. In this a minimum for the negative phase

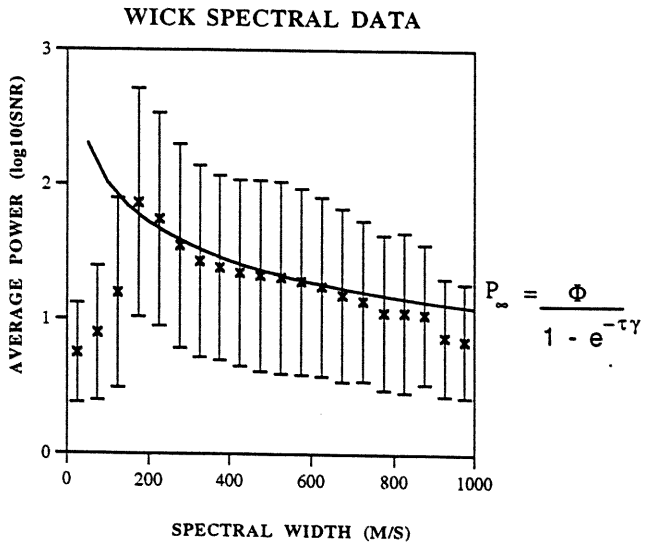

Figure 5.8 The variation of power with spectral width with the model curve of Equation 5.7.

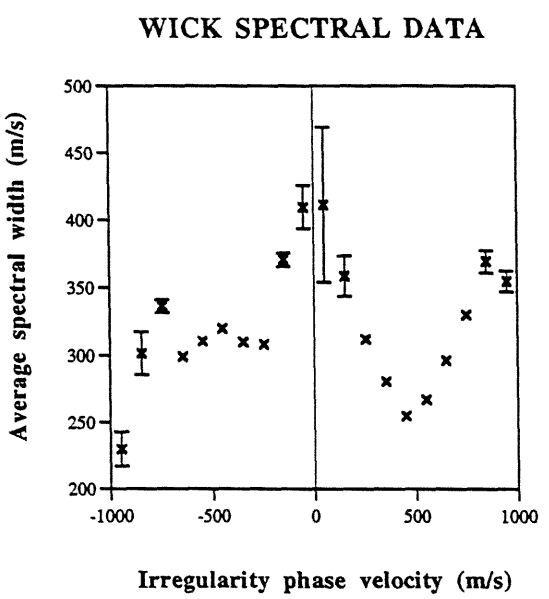

Figure 5.9 The average spectral width of irregularities observed by Wick for 100m/s bins of irregularity phase speed. The error bars denote the standard deviation of each average.

speed portion of the graph is observed. Its non-appearance in the post-midnight sector (negative flow regime) of Figure 5.9 may be a consequence of more variable flow patterns in that convection cell. Figures 5.9 and 5.10 suggest a relationship between the spectral width and phase speed. The question that can be investigated is whether any aspect of theory predicts such a relationship.

If the spectral broadening is controlled by the life time of a single irregularity, such that a long lifetime produces a narrow spectrum, then it is necessary to assume the irregularity growth rate γ is a good representation of the spectral width. The growth rate equation can be written as:

$$\gamma = \frac{\Psi}{1 + \Psi}\left(\frac{\omega^2 - k^2C_s^2}{\upsilon_i} + G\right) \qquad (5.8)$$

where G represents the gradient drift term. For the case where there are no gradients in density, G=0, γ has been plotted against ω/k for five different heights in Figure 5.11, experimental data is superimposed on each panel. The values for Equation 5.8 have been generated by the theory of Robinson and Honary (1990). This comparison indicates that the radar observations do not match the theoretical values.

This is not unexpected since, as already suggested, the observations are the result of a sum of contributions from different spectra. Furthermore, the theoretical condition for a stable irregularity is that the phase speed is equal to the local ion-acoustic speed when the growth rate, $\gamma = 0$. Non-zero spectral widths are a possible indication of a finite difference between the phase speed and the ion-acoustic speed. Assuming the magnitude of this difference was constant over all phase velocities, Equation 5.8 could be rewritten as:

$$\gamma = \frac{\Psi}{(1 + \Psi)\upsilon_i}\left(\text{constant scaling}(\chi)\right) \qquad (5.9)$$

In this equation the non-constant terms (Ψ and υ_i) will vary with the irregularity phase velocity since they are dependent on the background plasma drift velocity. In Figure 5.12, Equation 5.9 has been fitted to the data by adjusting the value of χ. The theory curve 'turns on' at just below 400m/s, rises to meet the data points and follows them closely until high phase velocities (>800m/s) when the two curves diverge. This would imply that the non-constant term from 5.9 is able to describe the variability of the irregularity data for phase speeds larger than 400m/s. A $\chi = 10^8$ was required to give the fit illustrated in Figure 5.12.

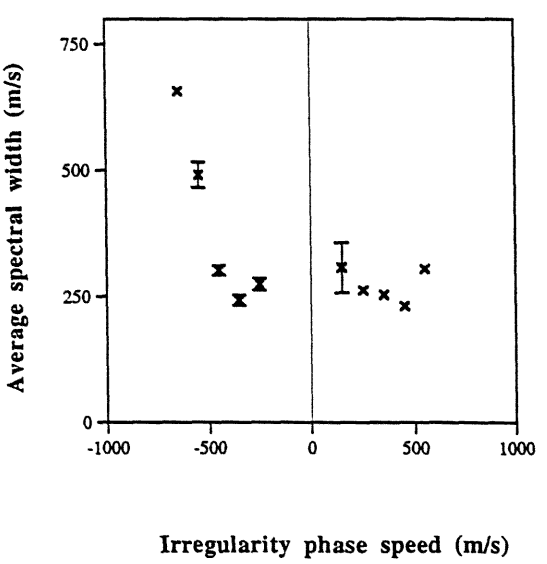

Figure 5.10 The same plot as Figure 5.9 but for a reduced interval of data (only 1986 days 70-73). Here a minimum for negative phase speeds is observed.

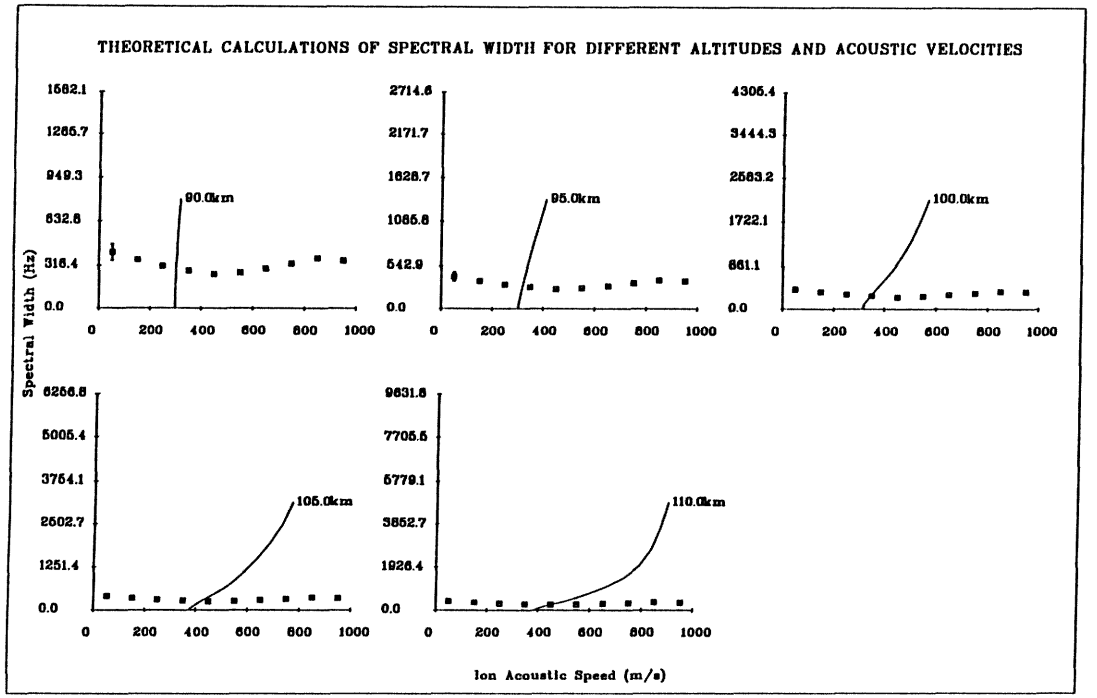

Figure 5.11 The full lines are theoretical calculations of the spectral width as a function of the ion acoustic speed for five different altitudes, following equation 5.8. Data points (squares) are superposed on the Figure.

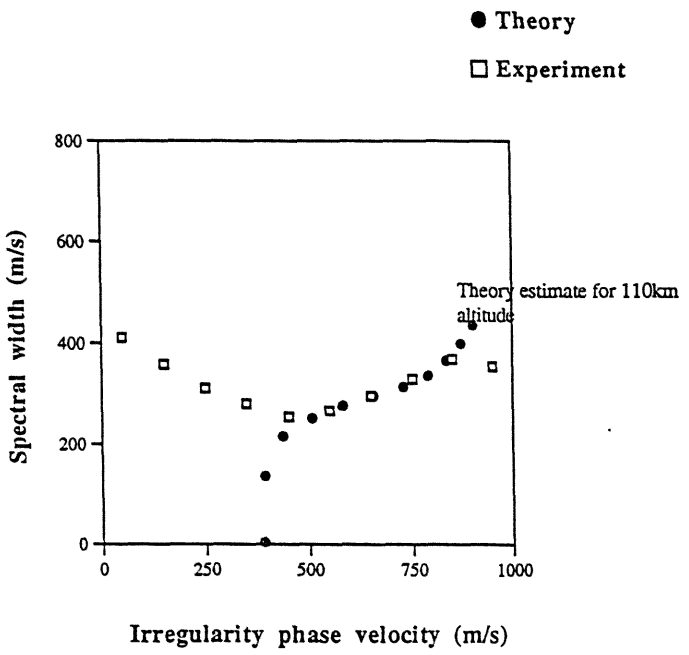

Figure 5.12 Theoretical calculation of the spectral width following equation 5.9.

To satisfy $\chi = 10^8$, when typically kC_s~6x300=1800Hz, implies the angular wave frequency ω has to be of the order 10^4Hz and thus an irregularity phase velocity near 1000m/s. This is clearly unreasonable. For two-stream waves the gradient drift term is usually taken as negligible, since the scale length L is taken as infinite. Substitution of order of magnitude values into the gradient drift term of $\Omega_e=10^7$Hz, $\upsilon_i=10^4$Hz, $\upsilon_e=10^5$Hz, $\omega=10^3$Hz, $k=10m^{-1}$ results in:

$$G = \frac{\Omega_e \upsilon_i \omega}{k \upsilon_e L} \sim \frac{10^8}{L} \qquad (5.10)$$

Thus for this to give the measured width, the scale length has to be about 1m, the same magnitude as the irregularity wavelength. This is a severe gradient not routinely observed. Equation 5.9 can account for the observed variation, however, current theory is unable to explain the value of χ required.

Figure 5.9 presented results from only the Wick radar. In Figure 5.13 and 5.14 similar plots for Halley and COSCAT respectively have been constructed. The COSCAT data reveal minima in the width for both positive and negative Doppler shifts near 450m/s, earlier reported in McCrea et al. (1991). A fit to Equation 5.9 has also been performed (Figure 5.15). The two curves are similar and the minimum in the data corresponds well to near 400m/s. The Halley data exhibits the trend that the spectral width increases with phase velocity, there are no distinct local minima. This is consistent with the growth rate equation prediction for gradient drift waves. Discarding the two-stream part of Equation 5.8 results in the expression:

$$\gamma = \frac{\Psi}{1 + \Psi} \left(\frac{\Omega_e \upsilon_i \omega}{kL \upsilon_e} \right) \qquad (5.11)$$

where the growth rate is directly proportional to the phase speed (ω/k).

5.4 Further studies on Wick spectral data

5.4.1 Power/Velocity/Width profile

The relationships between the spectral moments has so far been undertaken by considering pairs of components. In Figure 5.16 an attempt has been made to further investigate the Wick data by replotting Figure 5.5 but including extra information by

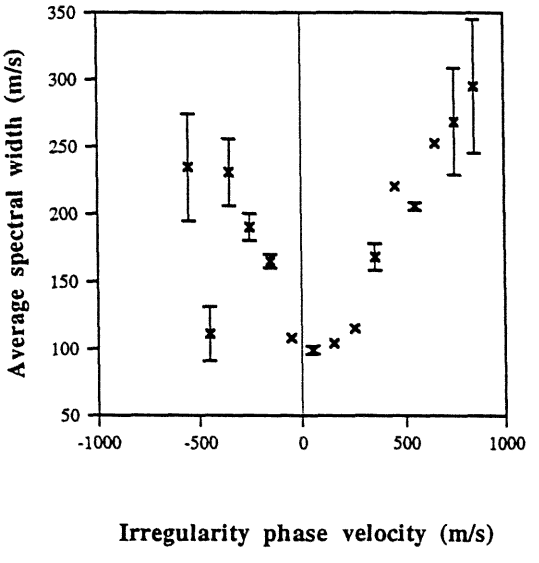

Figure 5.13 The average spectral width of irregularities observed in the E-region by Halley for 100m/s bins of irregularity phase speed. The error bars denote the standard deviation of each average.

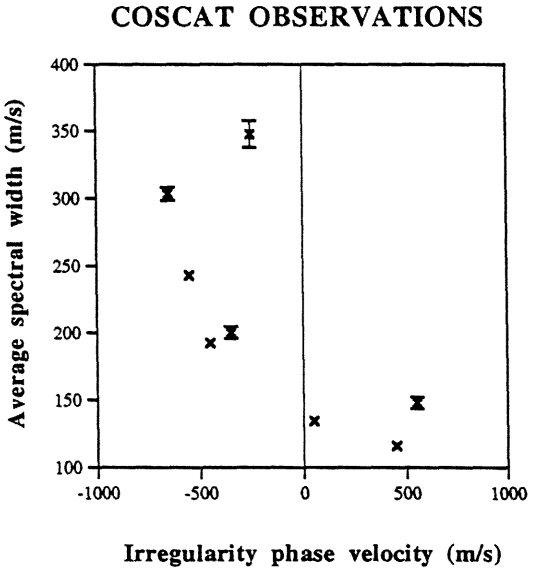

Figure 5.14 The average spectral width of irregularities observed by COSCAT for 100m/s bins of irregularity phase speed. The error bars denote the standard deviation of each average.

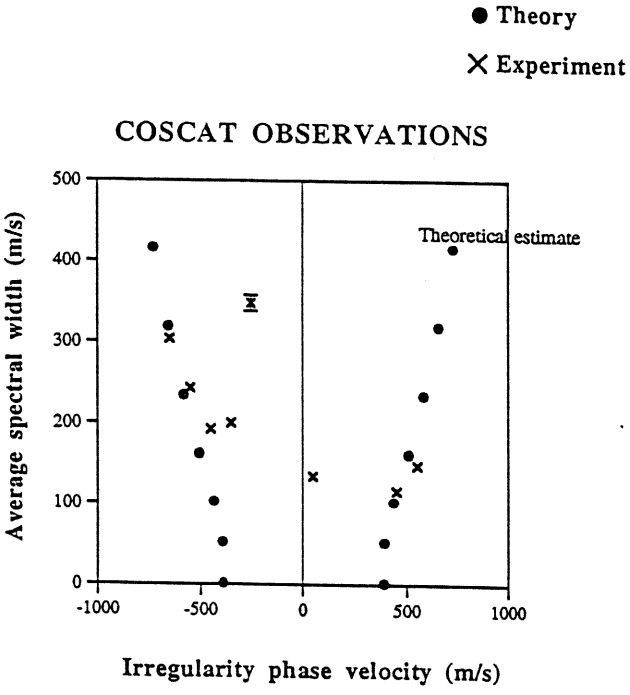

Figure 5.15 The average spectral width of irregularities observed by COSCAT for 100m/s bins of irregularity phase speed compared to a theoretical estimate derived from Equation 5.9.

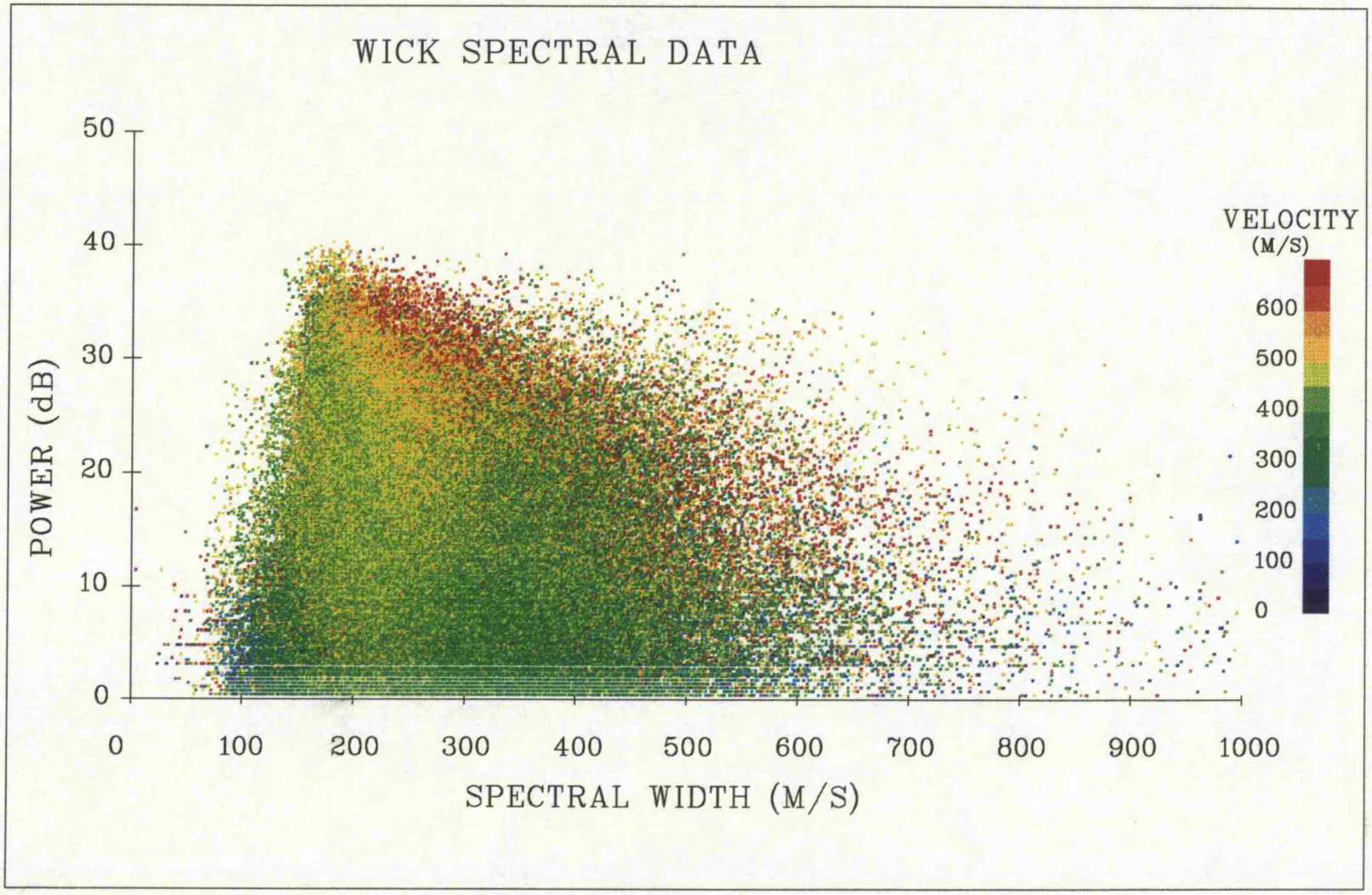

Figure 5.16 A plot of backscatter power against spectral width for Wick spectral data. The average irregularity phase speed is included as a colour coding.

colour coding the data in terms of the velocity. Schematically, the figure can be represented as:

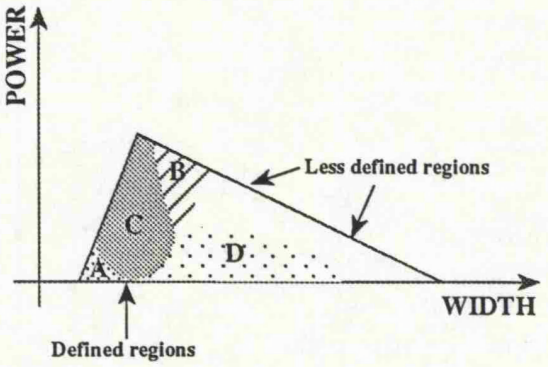

Some regions of the power vs. width plot correspond to narrow distributions in velocity. In other regions the velocity measurements are more spread. Four regions A, B, C and D have been identified to characterise the more ordered part of the plot.

A	Low power < 10dB. Low width < 150m/s. Velocities < 300m/s.
B	High power >20dB. Width 200 to 300m/s. Velocities above 350m/s, with a high proportion (50%+) > 600m/s.
C	Full range of power 0 to 40dB. Width 200±100m/s. Velocities 350 to 700m/s.
D	Low power >20dB. Width > 250m/s. Velocities 250 to 500m/s.

These regions are defined with the intention of illustrating the general structure in the graph. It is possible to associate irregularity types with the defined regions on the power/velocity/width profile as follows:

A	Type (II) (or Type(III)?)
B	Type (I) (or Type (IV)?)
C	Type (I)
D	Type (I) and Type (II)

Two regions of Type (I) irregularities have been identified. Region C comprises irregularities that conform to the typical Type (I) definition. In region B the phase speeds are much higher and they could possibly be identified with Type (IV). However, this is dependent on how the Type (IV) definition and generating mechanism becomes established. These high speed spectra resemble Type (I)s that have been

shifted to higher phase speeds, as consistent with plasma wave heating increasing the local ion acoustic speed, Robinson (1986).

In region A some spectra have widths of the order of 100m/s and phase speeds near 250m/s. These could be defined as Type (III). However these spectra typically have low powers just above the 3dB threshold. The peak in the spectrum is well resolved above the noise. The flanks are near the noise threshold. Since the flanks are not well resolved the spectra appear apparently narrow. It cannot be unequivocally stated that they are therefore Type (III), they are more likely Type (II). Region D is a mixture of Type (II) and Type (I) irregularities.

5.4.2 Morphology of Wick backscatter power

In Section 5.2.2 backscatter power statistics were summarised and compared at different wavelengths. Interpretation of power measurements is difficult since the irregularity cross-section is sensitive to a number of parameters, including the angle between the direction of irregularity propagation and the local magnetic field (magnetic aspect angle δ), the angle between the direction of irregularity propagation and the direction of the plasma drift velocity (flow angle θ), the electron density N_e and the amplitude of the electron density fluctuation ΔN_e. The relationships can be summarised following Kustov et al. (1989) as;

$$\sigma = F(\delta)H(\theta)\langle N_e^2\rangle\left\langle\left(\frac{\Delta N_e}{N_e}\right)^2\right\rangle \qquad (5.12)$$

In this study, the morphology of the backscatter power distribution for the Wick radar has been examined. There are limitations in using COSCAT or Halley. COSCAT detects irregularities at an unknown range. Halley makes single beam measurements and this beam is swung so there is a lack of simultaneity in azimuthal measurements. It is also more difficult to model the HF backscatter due to the refraction of the HF rays. Wick measures simultaneous values in 400 ranges cells over 8 beams giving regular snapshots of the spatial distribution of backscatter power, albeit smeared over a 20s integration period.

Examination of a large number of power range and azimuth plots for Wick indicate that the average power distribution is not uniform. Even under quiescent conditions when all the range cells are filled the observed intensities exhibit non-uniform distributions both in range and azimuth. Figure 5.17(a) is a typical example taken when there was a planetary magnetic index K_p of 4. The distribution contains a characteristic

maximum in power to the right of the central pointing direction at ranges at and beyond 900km.

The spatial distribution of backscatter intensity has been simulated. To achieve this a FORTRAN computer program was written to model various radar and coherent scatter characteristics. Details of the calculation the program performed are described in Appendix A. Figures 5.17(b) to 5.17(f) are a series of simulation results, each containing successively more modelling of backscatter physics. The scale on each simulation result is different. This was necessary in order to emphasise the variations in power that each successive simulation generated. The following table summarises the simulation procedure:

		Power Variation (dB)	
		Minimum	Maximum
5.17(a)	Raw data	0	32
5.17(b)	The backscatter volume was uniformly filled with irregularities. The beam sensitivity was assumed uniform in azimuth and elevation. No flow angle effects were included. A magnetic aspect sensitivity of 5dB/deg was adopted. Thus this represents a spatial map of how the orthogonality condition varies over the field of view.	15	35
5.17(c)	Effects of beam sensitivity including a Lloyd's Mirror effect, Mattin and Jones (1986), added. The beams were modelled to have a Gaussian shape.	10	32
5.17(d)	Flow angle effect included, following Oksman et al. (1986). The flows were assumed to be L-shell aligned.	0	14
5.17(e)	Layer of irregularities at 110km altitude, 10km thick.	0	28
5.17(f)	Number of irregularities increased with range.	0	32

Table 5.6

It was only possible to model the range variation if some *ad hoc* assumption about the distribution of irregularities with range was made, e.g. 5.17(f) where the irregularity numbers were increased with range. There are a number of justifications for this. A sudden turn on of irregularities at greater ranges is possible if the Wick field of view partially enters the auroral oval. Electric fields increase at higher latitude and thus more irregularities may be generated. Furthermore, work by Shand (1993, private communication) has revealed a strong relationship between power and phase speed. Differences in backscatter power may arise from changes in average phase speed as the range increase. The azimuthal variation of backscatter power can be accounted for by the other physical effects such as the magnetic aspect angle sensitivity.

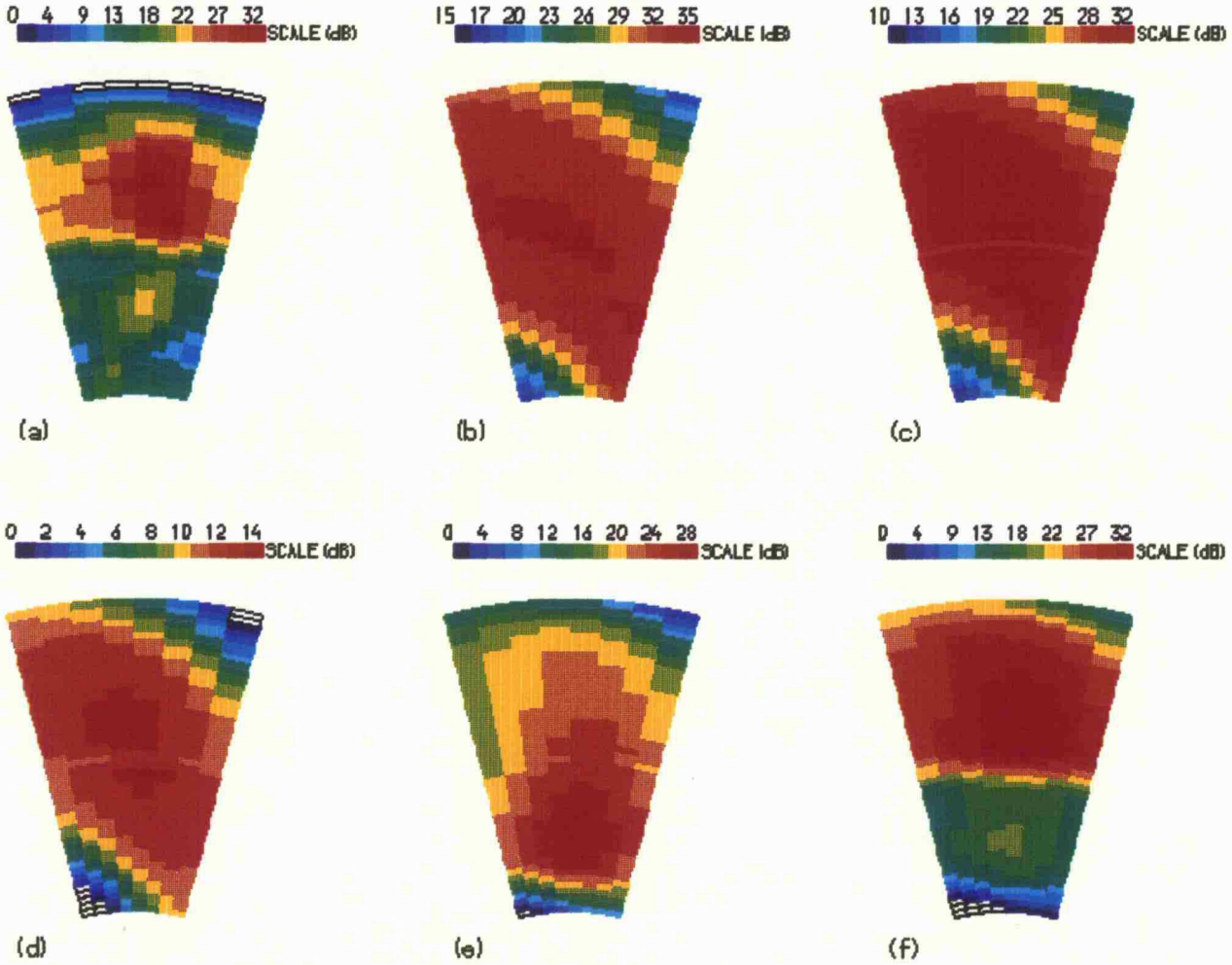

Figure 5.17(a) Raw Vick backscatter power data , (b) to (f) are results of the backscatter power simulation.

5.4.3 The influence of flow angle

Detailed studies have been undertaken of the relationship between irregularity characteristics and the angle between the radar look direction and the direction of the plasma flow. André (1983) performed an extensive statistical study of STARE data and established the dependence of the backscatter intensity on the flow angle. Mattin and Jones (1987) performed similar work with SABRE data. They separated Type (I) and Type (II) irregularity types and determined the behaviour of backscatter amplitude for each irregularity type with flow angle. Later work, Mattin (1994), involved the analysis of the phase speed and flow angle relationship. Mattin's work was based on a large sample of SABRE double-pulse data. With the spectral data now available, the analysis has been extended to an evaluation of the effect of the flow angle on spectral width. Early work by Nielsen et al. (1984) classified spectra into two categories 'narrow' and 'broad'. The width of the narrow spectra were insensitive to variations in the flow angle and the plasma drift speed. The width of the broad spectra was found to increase as the flow angle increased and also as the plasma drift speed increased.

The spectral data for which flow angle estimates could be made consists of 42 hours of continuous observation, during which only five periods of backscatter were observed. A typical time series is presented in Figure 5.18, which consists of four panels representing the time variation of the signal-to-noise ratio, phase speed, spectral width and flow angle running from top to bottom. The variations in flow angle are small, typical values are near 45°. For the whole data set the average value of the flow angle are 40° and 48° for westward and eastward flows respectively. These figures are subject to error, owing to sound speed limiting of the irregularity phase speed. Theoretical work by Robinson (1993) predicts the error to be within a few tens of degrees. From Figure 5.18 the minimum in flow angle, marked by an arrow, corresponds closely to a maximum in power, to a maximum in the magnitude of the phase speed and a maximum in the spectral width.

For all periods of backscatter, the measured spectral width has been plotted against flow angle in Figure 5.19, in which the distribution of phase speeds is included by means of a colour coding. The angle taken is the acute one between the radar look direction and the plasma flow, hence, all angles fall in the range 0° to 90°. Most of the data lies near a width of 200m/s at flow angles from 0° to 70°. This population of irregularities has phase speeds of 200 to 500m/s. The distribution of spectral width broadens as the flow angle increases up until about 60°. Regions of high and low velocity can be identified. The low velocity region is at large flow angle and above average width. The high velocity region occurs at smaller flow angles but also larger

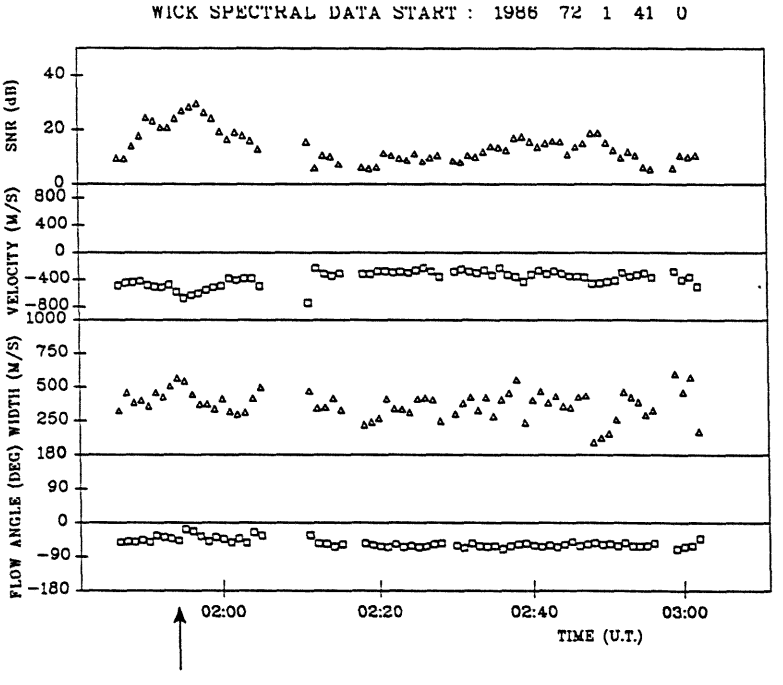

Figure 5.18 Time series of Wick Spectral parameters and simultaneous flow angle measurements.

widths. Replacing the width ordinate with power results in Figure 5.20. In this there appears to be no strong relationship between power and phase speed or power and flow angle. The phase speeds do vary as a function of the flow angle as described above.

5.5 Summary

This chapter contained a statistical survey of spectral characteristics and the result of their comparison to various theoretical ideas. The broader implications of these data will be discussed in Chapter 8.

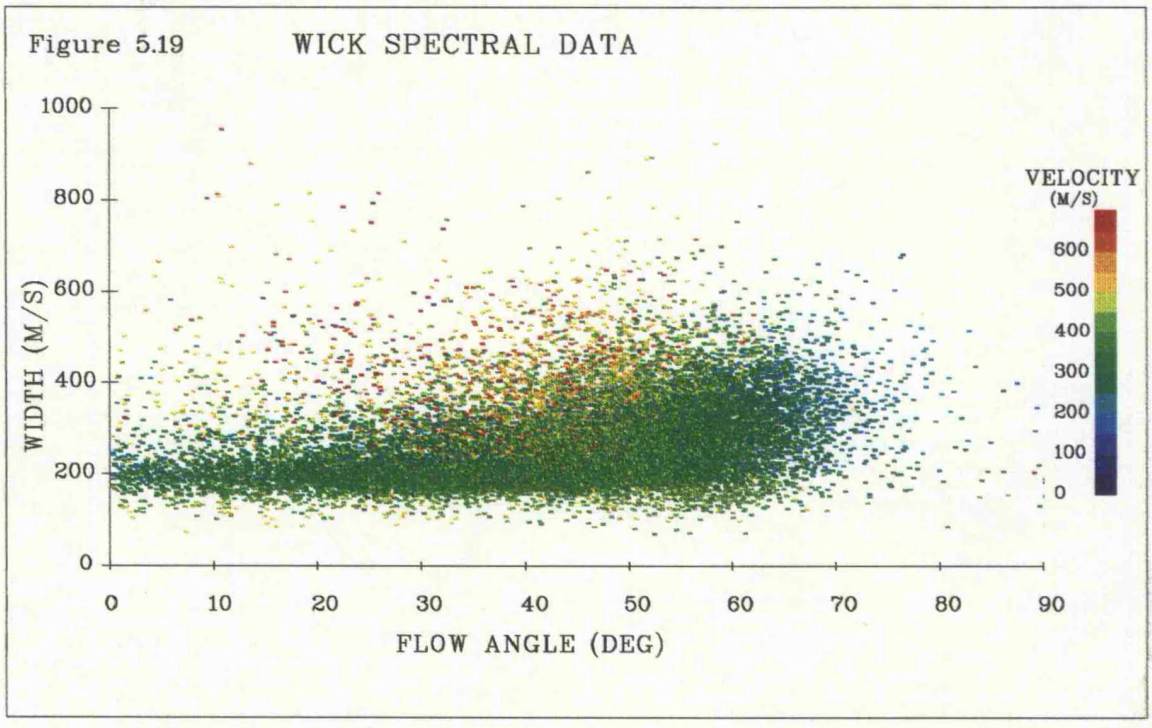

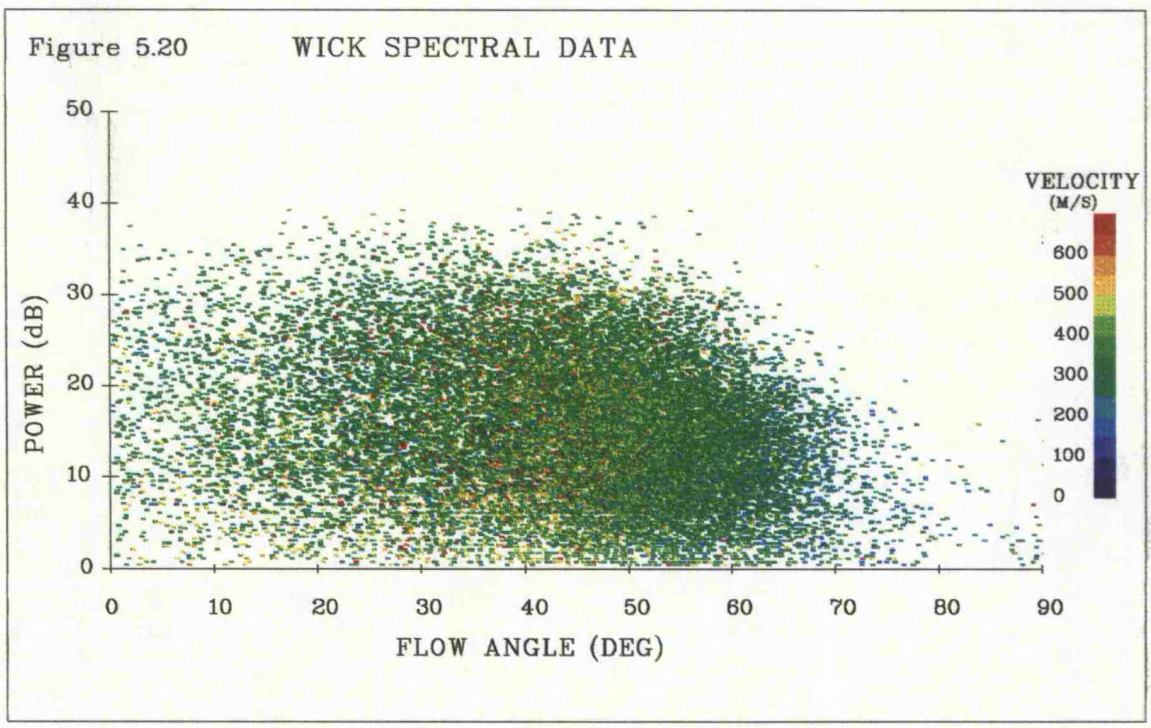

Figures 5.19 and 5.20. The relationship between the flow angle and Wick spectral parameters.

Chapter Six

THE RELATIONSHIP BETWEEN THE IRREGULARITY PHASE VELOCITY AND THE PLASMA DRIFT SPEED : EISCAT - SABRE COMPARISON

6.1 Introduction

An important application of coherent backscatter radar is in the study of ionospheric plasma flows. Knowledge of the plasma flow is essential for the investigation of plasma convection and the understanding of the interaction between the solar wind, magnetosphere and ionosphere. The results of linear fluid theory, e.g. Sudan et al. (1973), implied that the phase speeds of irregularities were equal to the component of the plasma drift velocity resolved in the line-of-sight of the operating coherent backscatter radar. Thus measurements of the phase velocity from two different directions would allow the plasma drift velocity to be established by simple geometry. The observation of a limiting value in the magnitude of the irregularity phase speed (Bowles et al. 1963, Abel and Newell 1969) and the development of non-linear theories (Sudan 1983) pinpointed the shortcomings of this approach. To allow a fuller understanding of the processes controlling the irregularity phase speed, knowledge of the background plasma drift is required. The plasma drift velocity can be measured by incoherent scatter radars.

Early work was conducted by Ecklund et al. (1977). These authors compared F-region incoherent scatter measurements from the Chatanika radar with E-region irregularity measurements obtained from a temporary coherent backscatter radar at Aniak. Their preliminary results suggested that coherent backscatter radar systems were able to measure auroral E-fields.

Nielsen and Schlegel (1983,1985) studied the relationship between the irregularity phase speed and the plasma drift speed by means of the Scandinavian Twin Auroral Radar Experiment (STARE). They observed irregularities at a radar frequency of 140MHz and compared the irregularity phase speed measurements to estimates of the plasma drift velocity made with EISCAT. They tested the ability of STARE to estimate electron drift velocities, found evidence to suggest the limitation of the phase speed to the ion-acoustic speed and developed an algorithm to derive improved estimates of the plasma drift velocity from coherent backscatter radar measurements.

In this investigation a similar comparison to that of Nielsen and Schlegel (1983,1985) has been undertaken but in this case between SABRE observations and those of EISCAT. The data from these experiments are analysed here. The aim is to investigate the relationship between irregularity phase velocities measured with SABRE and estimates of the plasma drift velocity. The results can be compared with current theoretical ideas and with results from other radar systems.

6.2 EISCAT - SABRE Experiment

Since 17/12/84 there have been nine EISCAT - SABRE campaigns. These involve the comparison of SABRE E-region observations of irregularity parameters with the simultaneous observation of the F-region plasma with the EISCAT facility. Coherent backscatter was observed in six of the experiments, these are summarised in Table 6.1.

DATE	START TIME (UT)	END TIME (UT)	TROMSØ	WICK
17:12:1984 1984(352)	15:07:00	21:08:40	BEAM-SWINGING AZ=229° & 249.4° EL=24.7°	PART OF BISTATIC SABRE
08:03:1986 1986(67)	13:30:00	22:10:00	BEAM-SWINGING AZ=229° & 249.4° EL=24.7°	SPECTRAL MODE, WICK ONLY
16:07:1987 1987(197)	17:31:40	19:40:20	FIXED POINTING AZ=240° ; EL=20°	WICK ONLY
15:02:1988 1988(46)	15:45:00	23:00:00	FIXED POINTING AZ=238.8° ; EL=24.7°	WICK ONLY
09:06:1988 1988(161)	20:03:20	22:11:00	FIXED POINTING AZ=240° ; EL=24.7°	WICK ONLY
18:12:1988 1988(353)	18:40:20	21:28:40	FIXED POINTING AZ=240° ; EL=24.7°	WICK ONLY

Table 6.1

The date for each experiment is given in calendar-day:month:year and year(day number) format. For brevity, the latter nomenclature will be adopted for all references in this text. It should be noted, that all observations took place in the evening convection cell. In the first two campaigns beam-swinging of the Tromsø receiver was employed in order to make velocity measurements when the signal-to-noise at the remote stations was poor. Later the Tromsø radar was kept in a fixed pointing mode.

The Tromsø transmitter and receiver looks at 12 range gates typically starting at an altitude of around 200km altitude and moving up in steps of 18km in height to over 400km. Each of these range gates can be associated with a range of geographic latitude and longitude. The EISCAT measurements at each of these F region positions are compared with the E-region coherent scatter measurements. For there to be any physical relationship between the F and E-region measurements the two observation points in the F and E-region examined must lie within the same magnetic flux tube. The justification for this is that the ExB drift velocity in the F-region at a given point is identical to the ExB drift velocity at a point on the same field line in the E-region (Banks et al., 1973). The manner in which the necessary parameters are obtained will be discussed in the next section.

To achieve the required magnetic field line mapping, the mean latitude and longitude of each of the F-region observation gates has been identified with a magnetic field line by means of the International Geophysical Reference Field (IGRF) model. The field line is then traced downwards into the E-region to a height of 110km. The E-region latitude and longitude is calculated and this position is converted into the co-located beam and range position of the Wick radar. An EISCAT range gate mapped down into the E-region has a length of approximately 15km. Consequently, positional errors arising from the mapping procedure will be of the order of one Wick range cell.

6.3 Determination of plasma flows

A single incoherent scatter measurement will give one component of the ion velocity in the F-region. EISCAT, having three spaced receivers, is capable of simultaneously measuring three independent ion velocity components, allowing the construction of complete ion drift vectors (Rishbeth and Williams, 1985). In the F-region, the ions move at close to the ExB drift velocity, thus EISCAT measures the F-region ExB drift. Mapping each measurement down the magnetic field line from the F-region observation point will give the ExB drift velocity at other altitudes on that field line. This includes the E-region where the ExB drift drives the electrons, but where the ions are constrained by collisions with the high concentration of neutral particles.

The plasma drift velocity plays an important role in the growth of E-region plasma waves (cf. Chapter 2). Ideally a direct measurement of the full plasma drift velocity in the E-region would be available. Unfortunately, the EISCAT radars are unable to look at E-region altitudes in the SABRE field of view. It was possible to measure only F-region, line-of-sight ion velocities to derive the ExB drift or estimate the drift velocity magnitude by an ion-energy balance approach (described below).

6.3.1 Plasma flow components

Two-stream irregularities become excited in the line-of-sight of a coherent backscatter radar if the component of the plasma drift velocity in that direction exceeds the local ion acoustic speed. One orientation of the EISCAT receiver and transmitter at Tromsø gives a close approximation to measuring this component directly (illustrated by the Tromsø look direction in Figure 6.1). The arrangement consists of the Tromsø receiver and transmitter pointing 229° in azimuth. In this orientation, the EISCAT beam is in the same vertical plane as the sixth (counting clockwise) beam of the Wick radar. The look directions of the two instruments are now offset by approximately 40° from being antiparallel and collinear. Hence, if it is assumed that the plasma drift is perpendicular to the magnetic field, EISCAT will only underestimate the component of the plasma drift velocity, in the direction of the Wick beam, by 25% maximum. The component gives information about the threshold conditions for excitation and provides a valuable test for linear theory.

Figure 6.1 is a schematic plan view of this experimental geometry. It also illustrates one possible orientation of the remote receivers at Kiruna and Sodankylä.

6.3.2 Plasma drift velocity V_D

The look directions of the Tromsø, Sodankylä and Kiruna receivers intersect at 273(±10)km altitude where tristatic measurements can be performed. Tristatic measurements will give the best estimate of the plasma drift velocity, Caudal et al. (1984). However, the geometry for tristatic measurements in EISCAT - SABRE comparison work is poor. The angles between the line-of-sight look directions of the EISCAT sites to the SABRE viewing area are small, no greater than 35° and the angle between the Kiruna and Sodankylä look directions is of the order of only 10°, leading to measurements of very similar components. Owing to the long slant range of the tristatic observation point, the signal to noise ratio at the remote sites is low, often less than 1%, contributing to large uncertainty in the estimated velocity, Jones et al. (1986). Attempts made to calculate a tristatic velocity resulted in the prediction of unrealistic velocity components parallel to the magnetic field, which contribute to more doubt concerning the measurements validity. Furthermore, since observations can only be made at one height in the F-region, the amount of data obtainable is limited. For these reasons, drift velocity estimates using all three sites was not pursued.

Beam-swinging techniques rely on making assumptions about the flow. Ideally the flow must remain uniform, both spatially, between the positions where components of

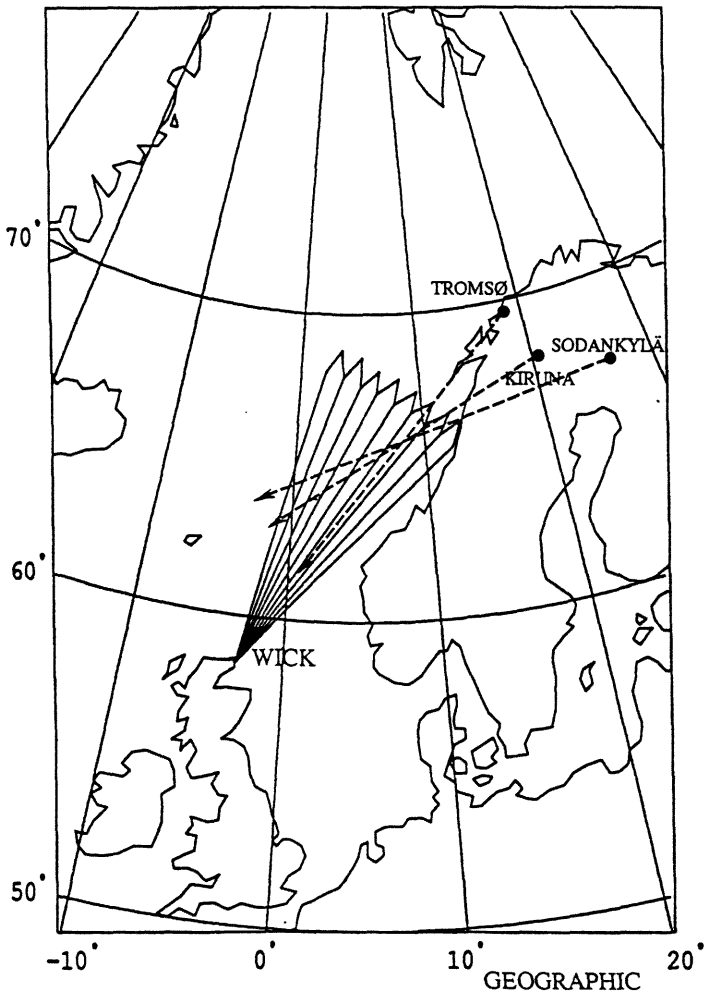

Figure 6.1 A schematic map of the EISCAT-SABRE experiment. Illustrated are the eight beams of the Wick field of view and one possible orientaion of the EISCAT transmitter (Tromsø) and receivers (all three sites). Such was used in the experiment of 3/8/86.

the flow are measured and temporally, between the times at which each measurement is made. Freeman et al. (1991) discovered that single-station estimates of the plasma flow were liable to errors and that it was impossible to determine when the estimates were right or wrong. Owing to the uncertainties in beam-swinging measurements, the fact that the technique reduces temporal resolution and since only a limited number of campaigns employed the beam-swinging option, no results from any beam-swinging analysis will be presented here.

There is a further technique that may be applied which will estimate the plasma drift speed, but not its direction. The technique relies on measurements of ion temperature and this is related to particle velocities through the ion energy balance equation. A full description of the ion-energy balance equation can be found in Banks and Kockarts (1973). One form of the equation which is valid for the F region measurements to be discussed here is given in St. Maurice and Hanson (1982):

$$\psi_{in} 3k_B(T_i - T_n) \approx m_n(v_i - v_n)^2 \phi_{in} + \left(\frac{m_i - m_n}{m_i}\right)\left(\frac{\upsilon_{ie}}{\upsilon_{in}}\right)3k_B(T_e - T_i) \qquad (6.1)$$

where ϕ_{in} and ψ_{in} are velocity dependent correction terms and the other symbols have their usual meanings as defined earlier in the text. The left hand term represents heat exchange between ions and neutrals, the first term on the right is a frictional heating term and the second, heat exchange between ions and electrons. The terms ϕ_{in} and ψ_{in} can be taken as unity and applying an algebraic simplification where T_{eq} represents the sum of the neutral temperature and the electron-ion heat exchange term, Equation 6.1 can be rewritten following St.-Maurice and Schunk (1977,1979) as:

$$T_i - T_{eq} = \frac{m_n}{3k}[v_i - v_n]^2 \qquad (6.2)$$

From this expression it is possible to estimate the magnitude of the E-region plasma drift velocity. A number of assumptions are necessary since the measurements from which the drift estimate are made are ion temperatures and components of the ion velocity in the F-region. The physics of the procedure were outlined in Section 1.4. To summarise, in both the E- and F-region $\Omega_e > \upsilon_e$ so the electrons move at the **ExB** drift velocity (provided there are electric fields present). For the ions $\Omega_i > \upsilon_i$ above 120km altitude so in the F-region they too move at the **ExB** drift velocity. In the E-region below 120km $\Omega_i < \upsilon_i$ and the ion motion is dominated by collisions with the neutrals. Measurement of the ion velocity in the F-region will give the **ExB** drift. The position of

this measurement can be mapped down a magnetic field to the E-region and give the E-region **ExB** drift.

It is possible to estimate the magnitude of the F-region ion drift velocity from Equation 6.2. Rewriting the Equation as:

$$|\mathbf{V_i} - \mathbf{V_n}| = \sqrt{\frac{3k}{m_n}(T_i - T_{eq})} \qquad (6.3)$$

it is necessary to ascertain the neutral velocity $\mathbf{V_n}$, the equilibrium temperature T_{eq} and the average neutral mass m_n. In the presence of no electric fields in the frame of reference of the neutrals, the ions will move with the neutrals. Thus under quiescent conditions, i.e. before the occurrence of backscatter when the electric fields are small, the measured ion velocity will be approximately equal to the neutral velocity. The average ion velocity measured for the quiet periods is input as the neutral velocity for Equation 6.3 during periods of increased electric fields and the observation of coherent backscatter. In the experiments analysed here, the quiet time ion velocity was typically close to zero and $\mathbf{V_n} = \mathbf{0}$ was found to be a good estimate. For example, Figure 6.2 contains a time series of the ion velocity component measured during the experiment of 1986(67). This experiment will be discussed in detail in Section 6.4 just one point needs to be made here. The horizontal bars on the figure correspond to periods of no coherent backscatter. During these periods the ion velocity component is close to zero. In addition, direct observations of neutral winds (Tetenbaum et al., 1986, Manson et al., 1990, Salah et al., 1991 and Johnson and Virdi, 1991) indicate the average velocity is less than 50m/s. Such magnitudes are 10% of the observed ion velocity component during backscatter and therefore the error arising from average quiet time neutral wind values is small.

Consequently, taking the neutral wind speed to be zero, the estimate of the plasma drift speed is:

$$V_D \sim V_i \sim \sqrt{\frac{3k}{m_n}(T_i - T_{eq})} \qquad (6.4)$$

T_{eq} is the temperature of the ions during quiet, unperturbed conditions when there is no frictional heating. At these times the ion temperature is of the order of the neutral temperature plus a small contribution from heat exchange with electrons. The time series of Figure 6.3 gives the ion temperature variation during the experiment of 1986(67). During the intervals not marked with a horizontal bar there are large

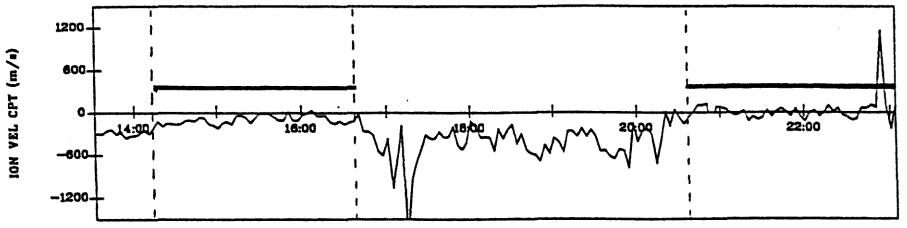

Figure 6.2 A time series of the ion velocity component measured by the Tromsø receiver for the experiment of 1986(67) at a height of 318km.

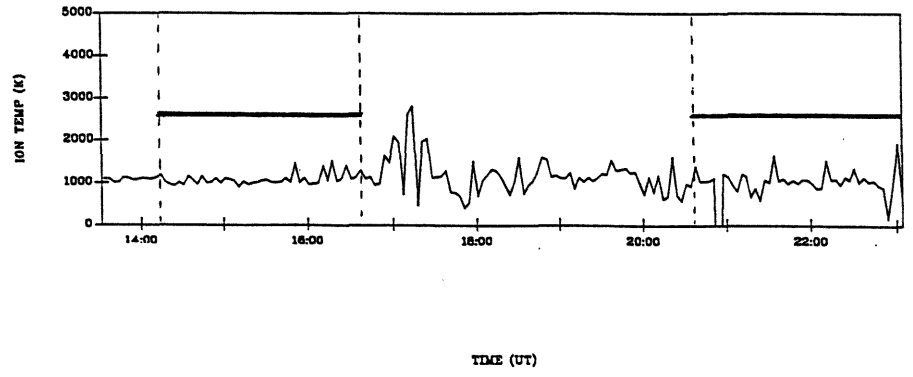

Figure 6.3 A time series of the ion temperature measured by the Tromsø receiver for the experiment of 1986(67) at a height of 318km.

The periods marked by horizontal bars on the above figures, correspond to times when the Wick radar observed no backscatter.

excursions in ion temperature. This corresponds to enhanced plasma flows and ion-frictional heating (and, as will be shown later in the data, the occurrence of coherent backscatter). The ion temperature here is in excess of T_{eq}. During other intervals, when the variation in T_i is small (<5%) there is no frictional heating and the ion temperature is at its unperturbed value, T_{eq}. Provided the majority of the data consists of no heating, the modal ion temperature for the interval gives a good estimate of Teq. For example, the histogram in Figure 6.4 corresponding to the previous time-series gives a modal temperature of 950K, with a confidence of ± 50K.

The neutral mass, m_n, was input as an average value calculated from the MSIS-86 model, Hedin (1987). The variation of the neutral mass with altitude was taken into account. A random error of up to 20% is expected in this value of the neutral mass. This contributes an error of 10% in the drift speed.

In the phase velocity with plasma drift speed comparison, averages of the irregularity phase speed are calculated for 200m/s drift bins. The plasma drift speed is then taken as the middle of this bin. This procedure reduces the significance of random errors in the plasma drift speed estimate.

6.4 Observations

In this section, the experiment of 1986(67) is discussed in detail and provides an example of the strategy adopted for the investigation of further data. The other experiments undertaken are also discussed and these data are presented and compared with each other.

The period of simultaneous EISCAT and Wick data for the 8th March, 1986 (1986(67)) runs from 13:32:20 up until just after 23:00hrs. These data are particularly informative since the Wick radar was operating in its spectral mode (see Section 4.2.1). Figure 6.5 is a time series of the irregularity power spectra. An overview indicates that most of the spectra observed are narrow (width at half maximum < 300m/s) and at average Doppler shifts in excess of 400m/s, these are typical characteristics of Type (I) irregularities.

Closer scrutiny of the Wick spectral data, Figure 6.5, indicates that the first period of backscatter occurs at 13:15 UT and persists for about one hour. The spectra have mean Doppler shifts of the order of 300m/s and the spectral widths at half maximum are 100-200m/s. After 14:15 UT no backscatter is observed again until 16:53 UT. A period of strong backscatter now takes place. The initial phase velocity is 400m/s which

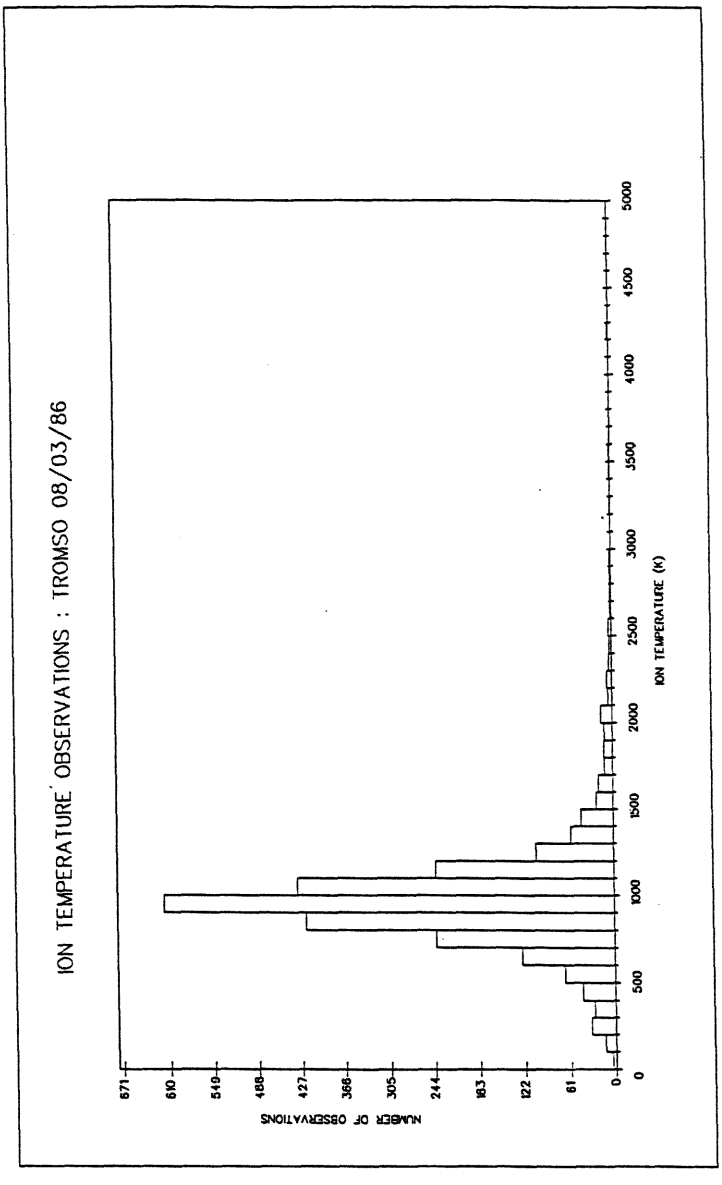

Figure 6.4 A histogram of the ion temperature observations from Tromsø for the experiment of 1986(67).

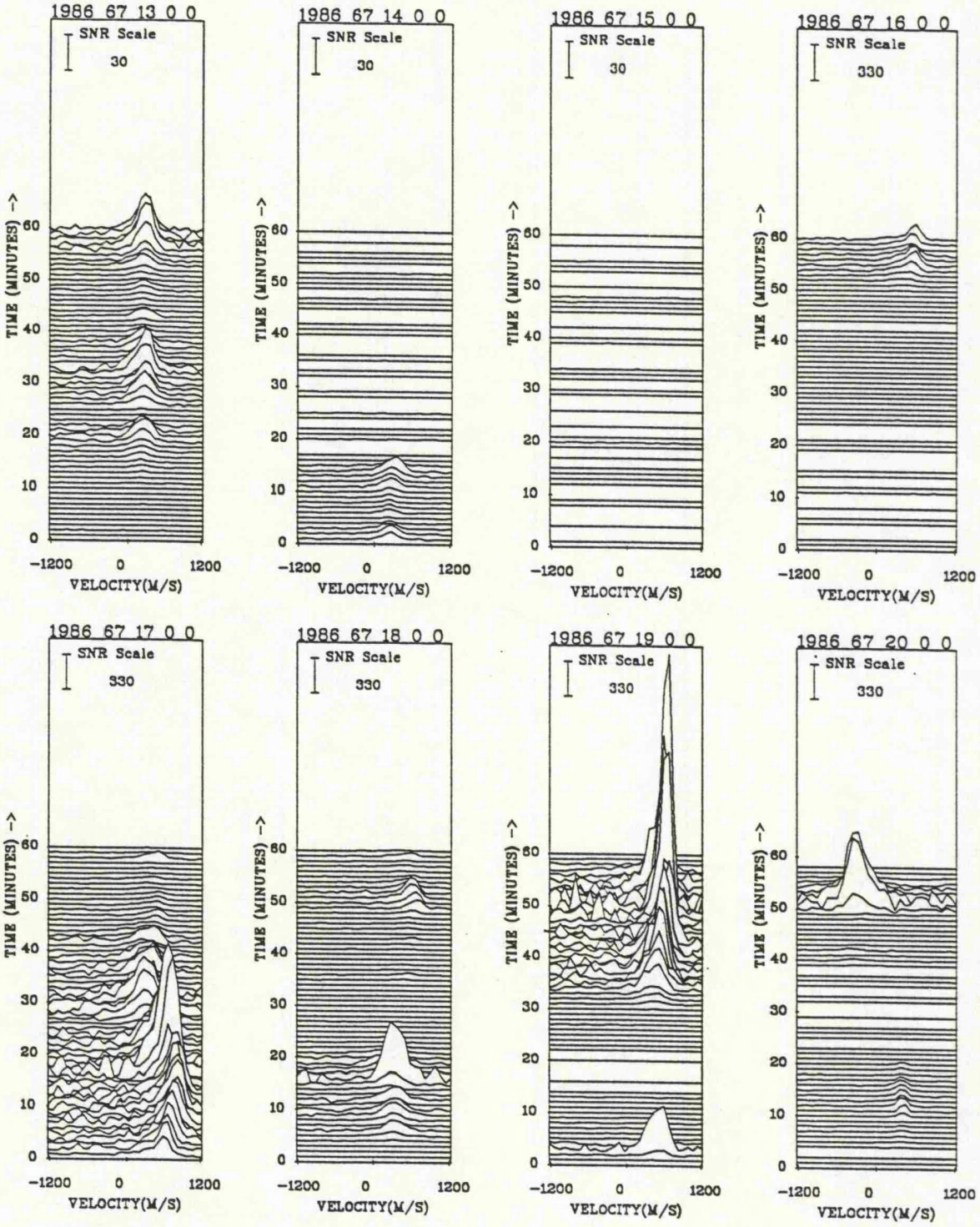

Figure 6.5 Irregularity spectra for the experiment of 1986(67). Each panel contains a series of consecutive spectra running from bottom to top. The start time of each panel is indicated across the top. The measurements come from the 6th (clockwise) Wick beam at a range of 1065km.

steadily increases over the subsequent half-hour to a maximum of 800m/s. This change is accompanied by an increase in backscatter power. The maximum signal to noise ratio in this second interval of backscatter is approximately twenty times greater than that in the first interval.

In the top panel of Figure 6.6 the irregularity phase velocities calculated from the backscatter spectra are plotted as a time series along with the ion velocity component measured from Tromsø. The sign convention taken is that velocities directed towards Wick are taken as positive. Following Section 6.3.1 the ion velocity component can be identified with a component of the plasma drift velocity in the E-region. The Wick data comes from the 38th range of beam six. The conjugate point to this in the F-region is at an altitude of 318km for the Tromsø pointing direction of 24.7° in elevation above the horizon and 229° in azimuth from geographic north. This geometry corresponds to the one which gives the best estimate of the plasma drift velocity component in the line-of-sight of the Wick radar (beam six clockwise). The bottom panel is a time series of the Tromsø measured ion temperature which will later allow the calculation of the plasma drift velocity. The initial period of backscatter (13:15 - 14:15 UT) appears at the beginning of the simultaneous data. For this interval, the ion velocity component is about 300m/s, consistent with the size of the ion acoustic velocity. At 14:15 UT the ion velocity component falls to the order of 200m/s and no more backscatter is observed. The data suggest a threshold for excitation of the irregularities of approximately 300m/s. As discussed in Section 6.3.1 this may be an underestimate. In the worst case, the actual threshold value will be 400m/s.

Backscatter resumes at 16:53 UT when the ion velocity component increases again. In all, the variations in irregularity phase velocity and ion velocity component are well correlated. Over the same period (13:15 - 16:53 UT), there are fluctuations in the ion temperature but on average it remains constant about 1100K. As the component of the ion velocity decreases there is no visible decrease in T_i. However, it is the whole vector drift velocity to which the ion temperature is sensitive. A rotation in the flow direction will change the magnitude of the velocity component in the direction of the Wick radar, possibly decreasing it sufficiently so that no irregularities are generated. However, provided the rate of change of $(V_i - V_n)$ is small, there is no ion-frictional heating and no change in the measured ion temperature.

The interval from 16:53 UT onwards exhibits periods of strong backscatter. The ion velocity component rises rapidly and this is accompanied by an increase in the ion temperature. The irregularity phase velocity is remarkably similar in magnitude to the ion velocity component up until just after 17:00 UT when the ion velocity component

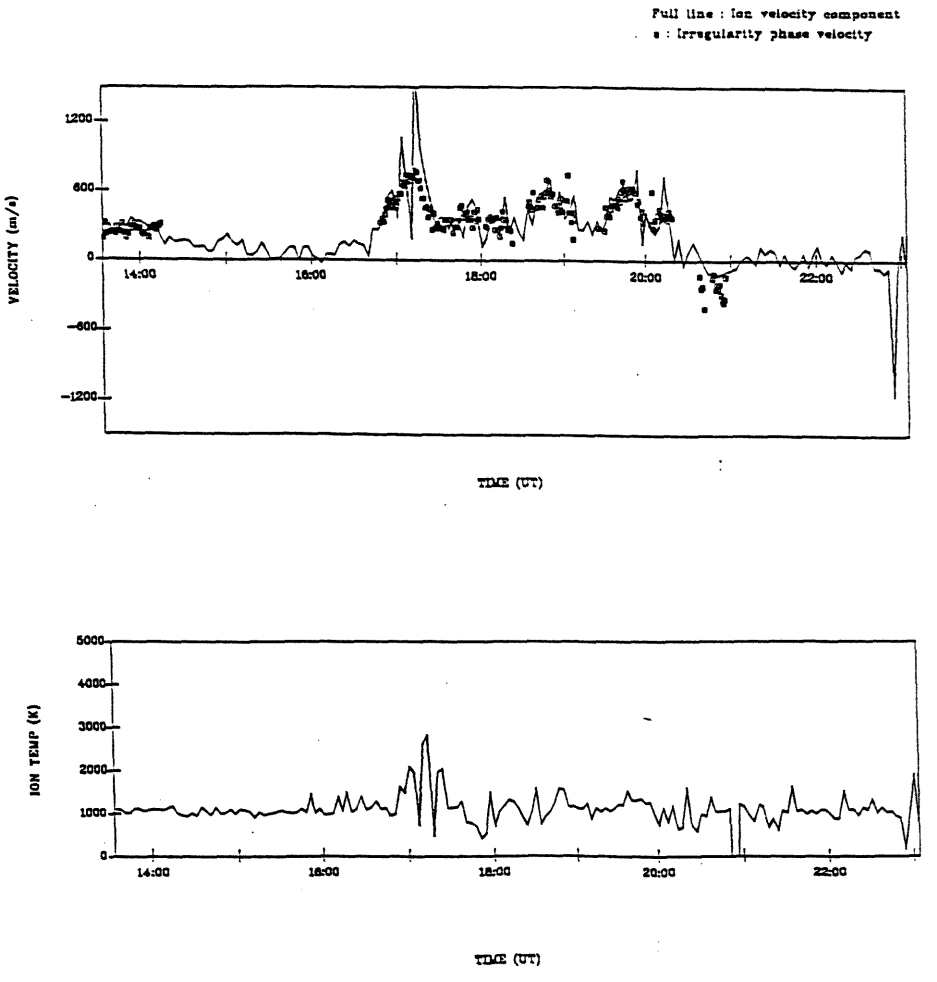

Figure 6.6 Time series of the ion velocity component measured by Tromsø and the irregularity phase speed measured by the Wick radar (top panel) for the experiment of 1986(67). The bottom panel illustrates the variation in the ion temperature for the same period.

exceeds the phase velocity that has maximised at 800m/s. After this peak in velocity, the ion velocity component and ion temperature fluctuations remain well correlated. The irregularity spectra are strong and narrow (refer back to Figure 6.5). A reversal in the plasma flow direction occurs around 20:30 UT. At this point the irregularity phase velocity exceeds the ion velocity component for the first time. The flow may now be in such a direction as to maximise the difference between the measured component of the ion velocity and the component in the line-of-sight of the Wick radar. Alternatively, neutral wind effects may have become important.

A more quantitative analysis of these data can be obtained by investigating the relationship between the directly observed quantities. A graph of simultaneous irregularity phase speeds and ion line-of-sight velocities is presented in Figure 6.7(a) (westward flows only). This includes data from all twelve Wick ranges and the conjugate EISCAT positions. The data are scattered either side of the superimposed 'y=x' line for low drift velocity components. For high values the phase speed is less than the line-of-sight ion velocity. This is demonstrated more clearly if the average phase speed is plotted for 200m/s bins of the ion drift Figure 6.7(b). Linear theory (e.g. Sudan et al. 1973) predicts that the relationship follows the dashed 'y=x' line included on the graph. This is not satisfied here. In order to compare the observations with the results of non-linear theory, the magnitude of the plasma drift speed V_D is required. In the next section, the comparison of the irregularity phase velocity to an ion temperature derived plasma drift velocity will be presented and discussed.

Figure 6.8 contains time series of the EISCAT measured ion velocity component and the corresponding, Wick-measured, irregularity phase speed for the other EISCAT-SABRE experiments. For each experiment, data from only one EISCAT altitude is presented. In none of these experiments is the geometry identical to that in 1986(67). In each case the Tromsø beam looks across several Wick beams, rather than being in line with a single beam as in 1986(67). The Tromsø line-of-sight measurement cannot be identified with the component of the plasma drift in the direction of any Wick beam. However, it does serve as a good indicator of the background flow conditions that drive the plasma instabilities. In 1988(46), 1988(161) and 1984(352) periods of backscatter correspond to significant increases in the ion velocity component. In 1987(197) and 1988(353) there are only small changes in the ion velocity component. During backscatter the ion velocity component tends to be of the same order of the irregularity phase speed or larger. Often the variations in the measurements are well correlated, 1988(161) for example. The interval between 15:45 UT and 17:00 UT of 1986(46) is considered further. Here the ion velocity component and the irregularity phase velocity are well correlated. However, when the ion velocity component is large

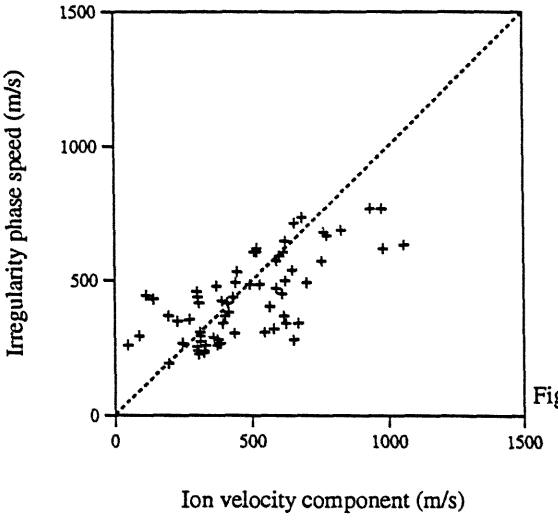

Figure 6.7(a)

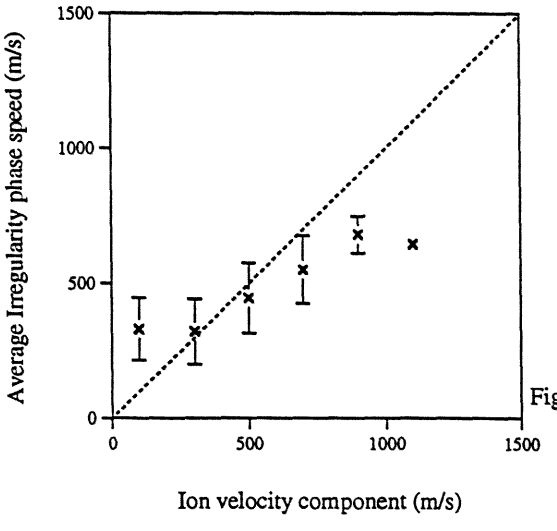

Figure 6.7(b)

Figure 6.7 A comparison between the irregularity phase speed and the ion velocity component for the Experiment 1986(67).

Figure 6.8 Time series of the ion velocity component (full line) and irregularity phase speed (boxed points) for all the other experiments; (i) 1984(352), (ii) 1987(197), (iii) 1988(46), (iv) 1988(161) and (v) 1988(353).

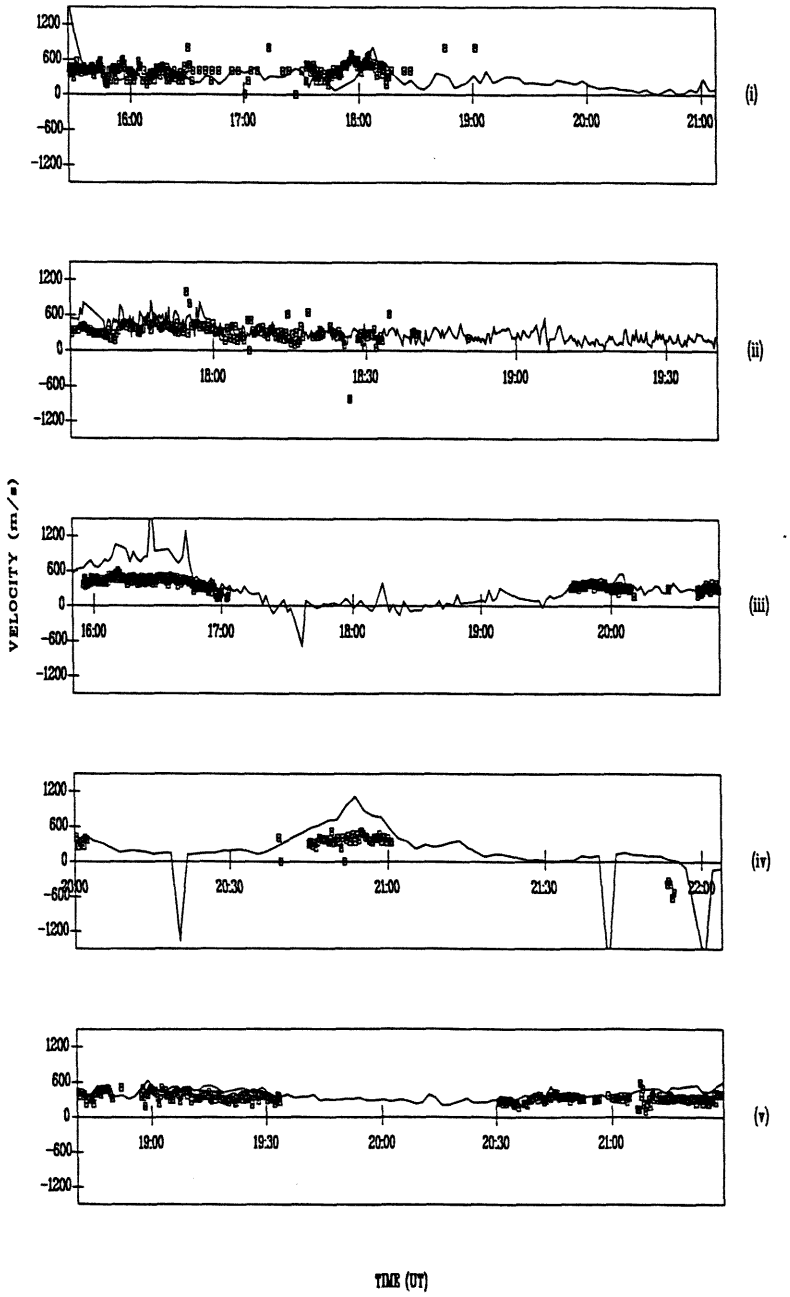

(≥1000m/s) the irregularity phase velocity is about 500m/s, indicating limiting in the phase velocity to a value below the plasma drift velocity component. As the ion velocity component falls it tends to the same value as the phase velocity. This is consistent with the plasma drift velocity component approaching the critical value for the excitation of irregularities.

However, as stressed before, this analysis has only examined a component of the drift velocity. In order to obtain a more complete understanding a comparison with estimates of the plasma drift speed are now made.

6.5 Drift Velocity Magnitude Analysis

The magnitude of the plasma drift velocity in the E-region is calculated from Equation 6.4 for assumptions, regarding T_{eq} and the neutral mass, as described in section 6.3.2. For each experiment the average irregularity phase speed is plotted against an ion temperature derived plasma drift speed. The average values of the irregularity phase speed have been calculated for 200m/s sized bins of plasma drift speed.

As described in section 6.3.2 the principal errors will arise in the estimate of the plasma drift speed. The estimate will be especially poor if there is a large component of the neutral velocity parallel to the ion drift. Tests have been applied to the data to remove any bad estimates. Firstly, if the magnitude of the ion velocity component measured by the Tromsø receiver is greater than the ion temperature drift speed estimate, the estimate is clearly unphysical and these data are removed. Plots of the ion velocity component against estimated drift speed, for each experiment are illustrated in Figure 6.9. Clearly in 1988(161), 1984(352),1986(67) and 1988(46) most of the drift estimates are greater than the component in the line-of-sight direction. The data for these experiments reveal that the ion velocity component approached zero for periods of no backscatter. In the cases of 1988(353) and 1987(197) the ion velocity component varies less between times of backscatter occurrence and absence and more drift speeds can be seen to be poor estimates.

Once backscatter has been initiated following an increase in the plasma drift speed, it is important to consider the subsequent evolution of the neutral particle motion. As the ion velocity increases the neutrals will respond and their velocity will approach that of the ions through collisions. This process takes from 30 minutes to several hours, Baron and Wand (1983). To investigate the effect of this, short periods of data at the beginning of the time series were analysed. This was found to make no significant

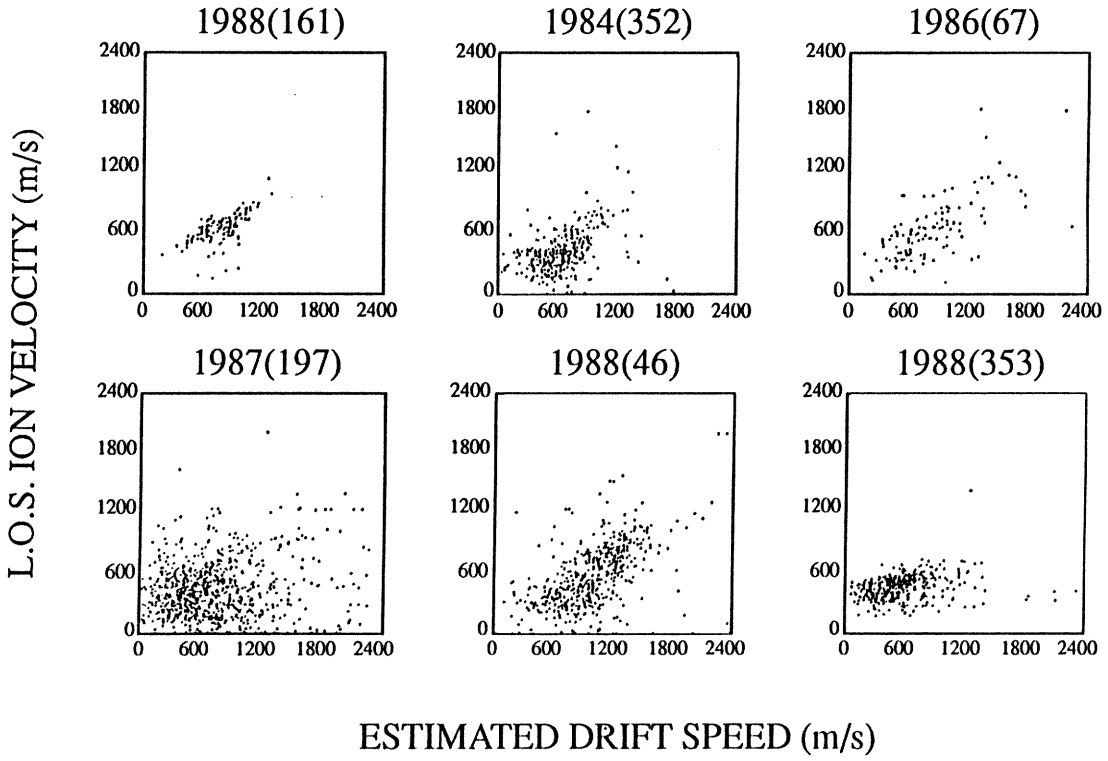

Figure 6.9 Graphs of the ion velocity component against the estimated plasma drift speed for each experiment.

difference to the results (presented next). From this it can be concluded that effects of neutral pick up were not important for these data.

Poor estimates may also arise due to errors in the EISCAT measurement of ion temperature. Thus the data for each EISCAT height is further screened by plotting the ion temperature against the measured ion velocity component, e.g. Figure 6.10. The ion temperature method relies on there being a quadratic relationship between the ion velocity and ion temperature. This can be seen by expanding Equation 6.2:

$$T_i = \frac{m_n}{3k_B}\left(V_i^2 - 2V_i.V_n + V_n^2\right) + T_{eq} \qquad (6.5)$$

In Figure 6.10 it is the ion velocity component that is plotted, this is related to ion velocity by:

$$V_{cpt} = V_i \cos\theta \qquad (6.6)$$

where θ is the angle between the plasma drift velocity direction and the line of sight of the Tromsø receiver. If the direction of the plasma drift remains constant then the T_i vs. V_{cpt} graph will follow a quadratic curve. A quadratic fit has been plotted on Figure 6.10 with a confidence of 95% that it is a good model. 75% of the observed altitudes from the six experiments had confidences of 80% and over. Data with a confidence of less than 50% (10% of observations) were not included in the comparison.

The results of this approach are illustrated in Figures 6.11(a) to 6.11(f) where the data from each experiment are plotted separately. Superposed are theoretical estimates of the irregularity phase speed as a function of the plasma drift speed calculated from the kinetic theory of Robinson and Honary (1990). The theoretical curves vary as a function of altitude. Only the altitudes (in steps of 5km) that give theoretical values that lie closest to the data are plotted. The vertical bars on the data points denote the standard deviation of the average irregularity phase velocity.

For each experiment the spread of irregularity phase speed for a given bin is large, of the order of ±100m/s. However, in all experiments except 1988(161), the data either lies between a pair of theoretical curves for a set of adjacent altitudes or a single curve lies close to the variation exhibited in the data.

It is apparent from the data that different experiments are best fitted by theory for different altitudes. This confirms that the altitude from which backscatter is observed is

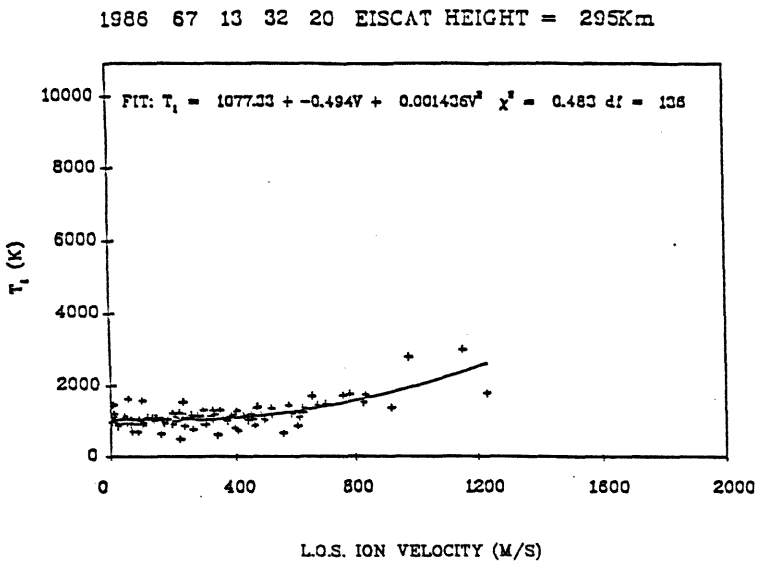

Figure 6.10 A graph of the ion temperature against the ion velocity component, including a quadratic fit performed on these data.

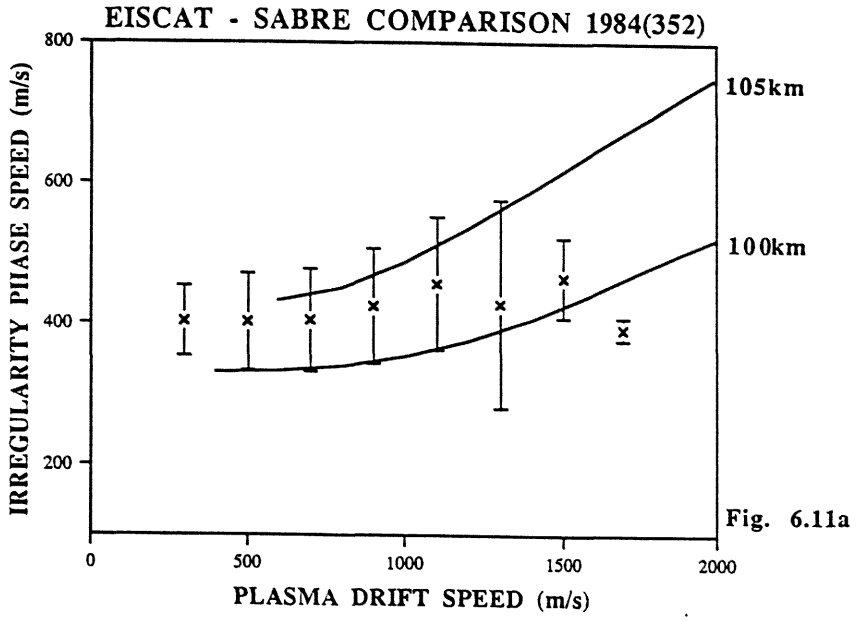

Fig. 6.11a

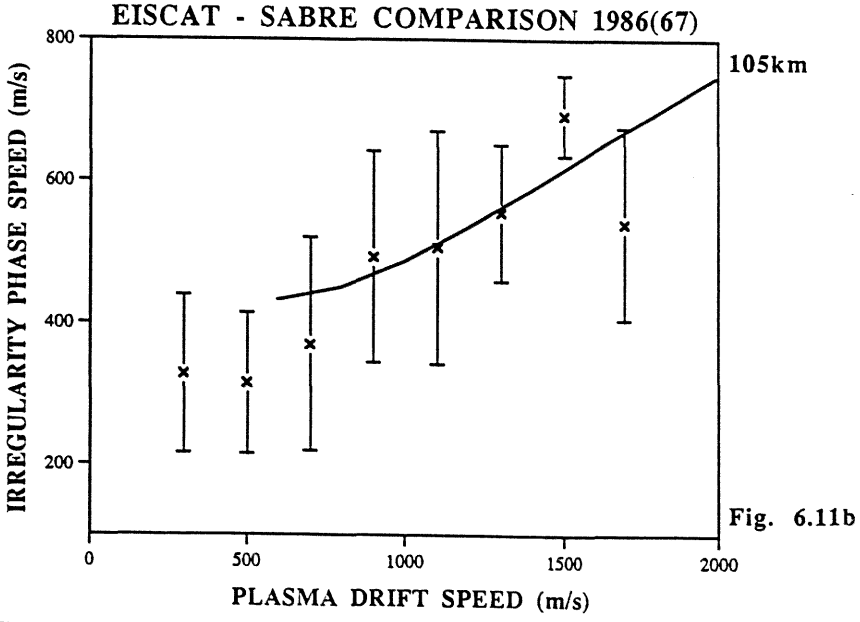

Fig. 6.11b

Figure 6.11 The irregularity phase speed plotted against the estimated plasma drift speed for the six EISCAT-SABRE experiments where backscatter was observed. Kinetic theory curves for the relationship between the phase speed and the plasma drift speed are superposed from Robinson and Honary (1990).

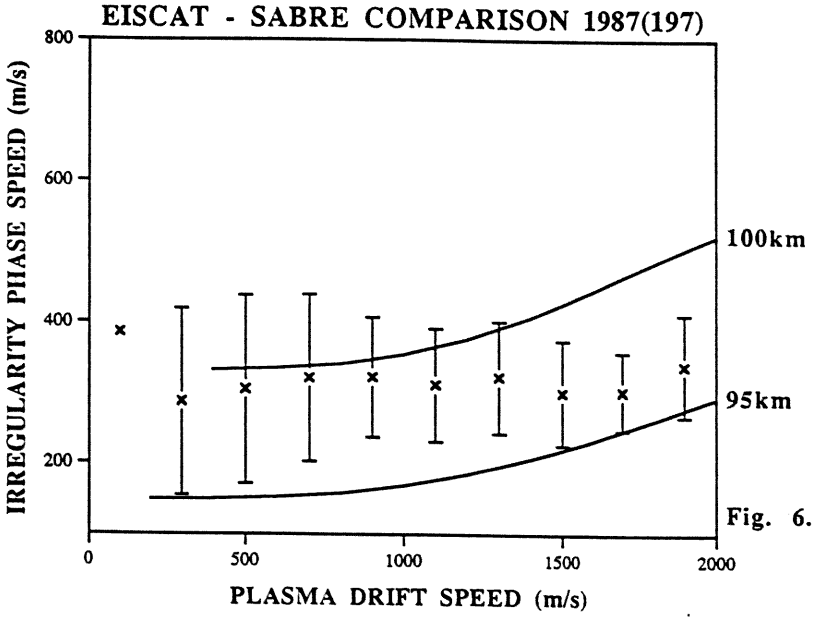

Fig. 6.11c

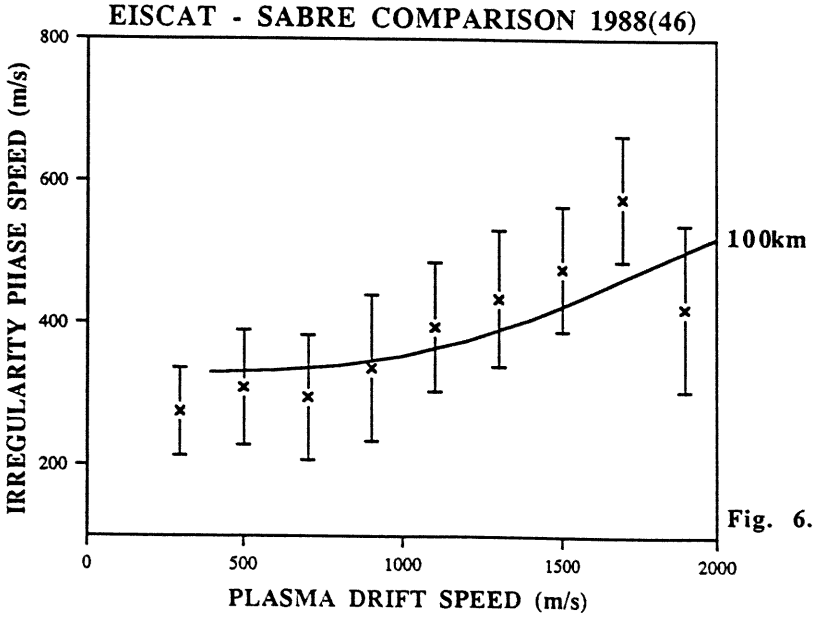

Fig. 6.11d

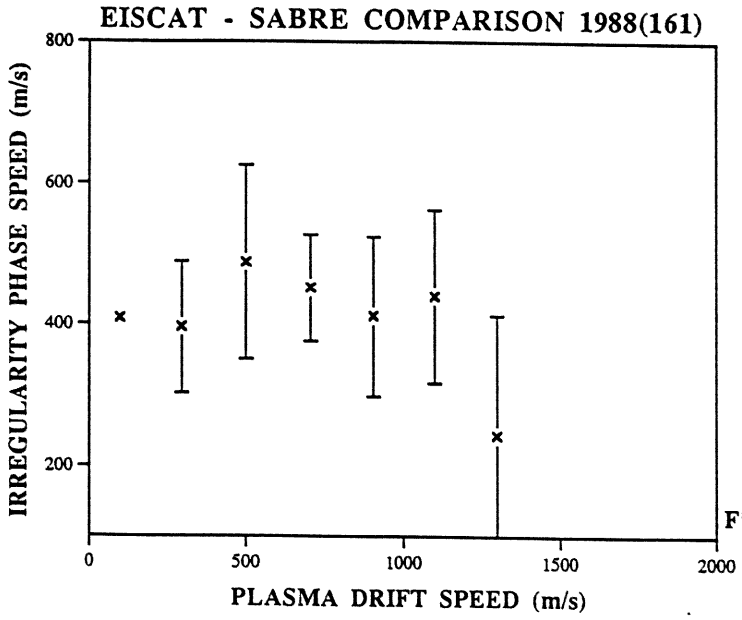

Fig. 6.11e

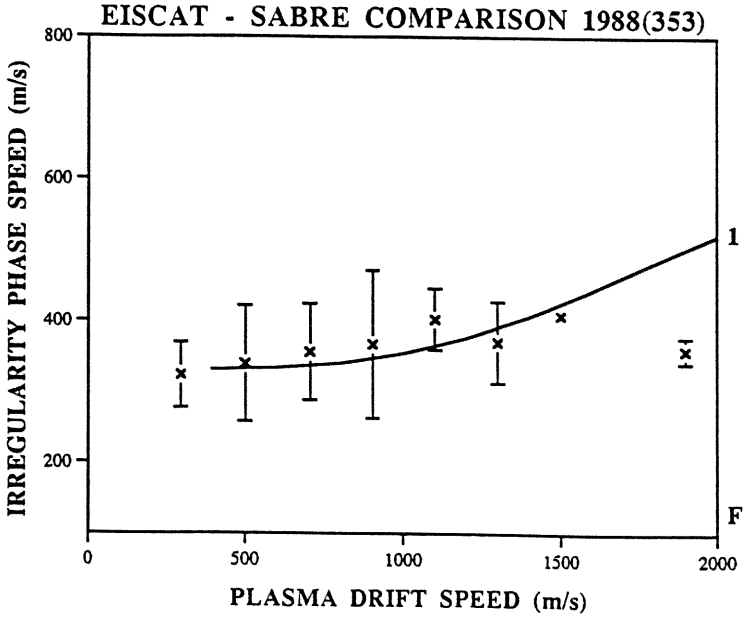

Fig. 6.11f

variable and indicates that there is variability in the altitude of backscatter on a day to day basis of the order of 10km. During a single experiment, backscatter may occur from a number of altitudes simultaneously. This can account for the spread in the observed phase velocities and for differences in the gradient of the mean variations in the data compared with the theoretical curves.

The data of 1988(161) does not fit any of the theoretical curves. However, if the number of EISCAT heights and corresponding Wick range cells is reduced, good comparisons are achieved. For example, Figure 6.12 is composed from three consecutive EISCAT heights from this experiment. The data follow the theoretical curve for an altitude just below 105km. It is evident that there was great spatial variation in the plasma flow conditions for the experiment of 1988(161). It is not possible to make a single comparison for all the data, each EISCAT height must be analysed individually.

In all the data (other than 1987(197) where the average phase speed remains constant) there is an increase in the phase speed as the plasma drift speed increases up to approximately 1500m/s. After this a decrease or levelling of the phase speed is observed. The theoretical curves themselves begin to level off at drift speeds in excess of 2000m/s. The increase in phase speed ceases at lower drift speeds which may indicate a deficiency in the theory. Alternatively, the drift velocities are systematically underestimated or there may be errors in the prediction of high drift speeds. There is evidence for the last suggestion in the data. Examination of the time-series corresponding to individual heights for 1988(353) reveals anomalous ion temperature measurements. Figures 6.13(a) and 6.13(b) are two ion temperature time series that exhibit steady behaviour. However, in Figures 6.13(c) and 6.13(d) large diversions are observed in the ion temperature starting at around 20:00 UT. At the same time, for all data, the ion velocity component exhibit no such variation from height to height, but is steady as in Figure 6.8(v). Meanwhile, there is no significant increase in the irregularity velocity or ion velocity component. This leads to the behaviour observed in the result for 1988(353) at high drift speeds.

6.6 Wick Calibration Curve

Nielsen and Schlegel (1985) derived an empirical relationship between the irregularity phase velocity as measured by STARE and the plasma drift velocity obtained by tristatic measurements with EISCAT. The equation they fitted to the data was of the form:

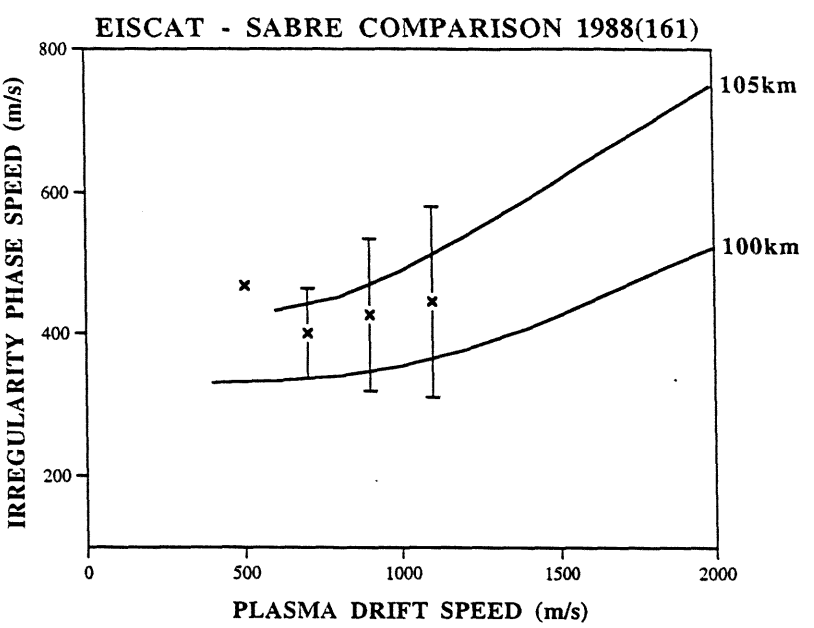

Figure 6.12 As Figure 6.11(e) but only using data from three consecutive Eiscat heights in the middle of the field of view

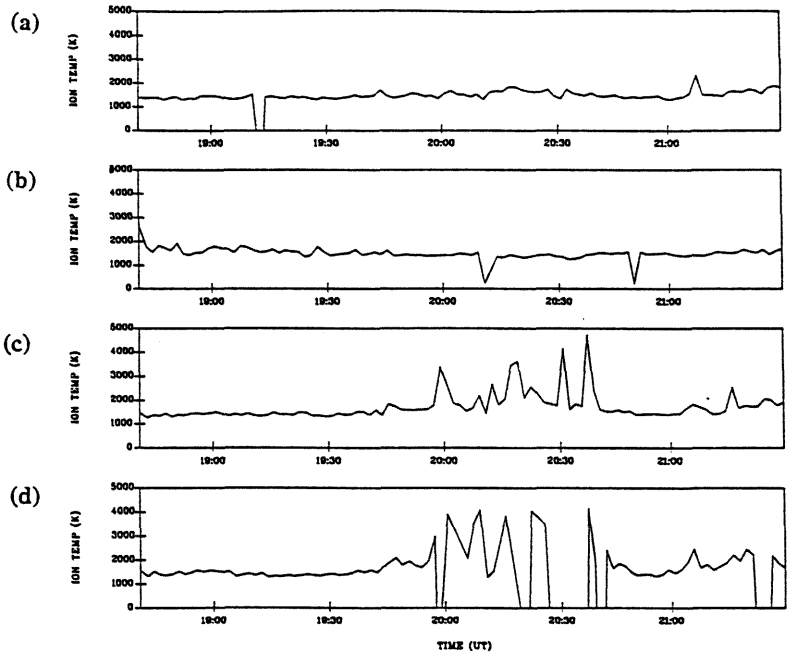

Figure 6.13 Time series of the ion temperature for the experiment of 1988(353).

$$V_{ph} = a + bV_D^2 \qquad \text{valid for } V_D<1600\text{m/s} \qquad (6.7)$$

and found values for the constants of

a = 300 (400)m/s westward (eastward) electron flow

b = 0.00011

where V_D is the electron drift velocity (ion temperature estimate).

A similar fit has been performed on the EISCAT - SABRE data set using all the available data and the result is presented in Figure 6.14. The fit (solid line) was only performed on the plasma drift speed bins ranging from 200 to 1400m/s. The fit gives 'a' and 'b' parameters of 320m/s and 0.00005 respectively. A kinetic theory curve (Robinson and Honary, 1990) is also included (dashed line) for an altitude of 100km.

The calibration curve is a parameterisation of the Wick data. It contains data from all the experiments that encompass a variety of geophysical conditions. It thus gives an average variation rather than one specific to a particular level of geomagnetic activity.

6.7 Summary

The data from the series of experiments have confirmed a strong correlation between the irregularity phase velocities measured at Wick and components of the plasma drift velocity measured with EISCAT.

The data demonstrate that the irregularity phase velocities measured with the Wick radar exhibit systematic non-linear behaviour with respect to the plasma drift speed. The kinetic theory of Robinson and Honary (1990) provides a good description of this behaviour for plasma drift speeds between 500 and 1600m/s. The variation of phase speed at a given plasma drift speed can be attributed to backscatter from different altitudes. At high drift speeds (>1600m/s) deviations from the theory occur. This is either a result of a limitation in the ion temperature method for estimation of the plasma drift speed or an experimental fact, which new theory should address.

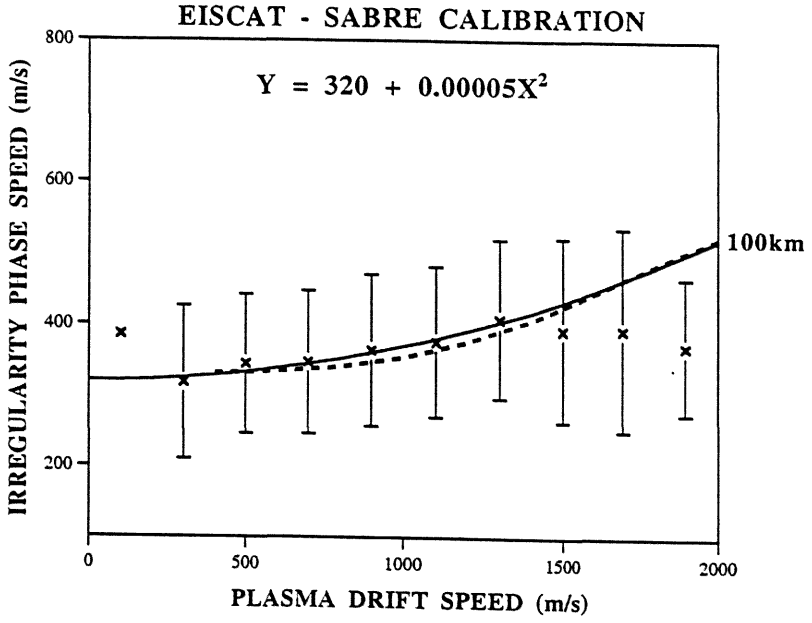

Figure 6.14 The full line is a calibration curve for the Wick radar derived from all the data. In addition, the dashed line is the kinetic calculation of the phase speed as a function of the plasma drift speed for an altitude of 100km.

Chapter Seven

ACTIVE EXPERIMENTS WITH COSCAT

7.1 Introduction

ACTIVE COSCAT (ACOS) experiments share common aims with the EISCAT - SABRE work described in the previous chapter. In addition, ACOS gives the first measurements of irregularities at a 16cm wavelength, a regime where only kinetic theory is applicable. It will be possible to make a valuable comparison of the ACOS results with the previous STARE and SABRE experiments.

A preliminary ACOS experiment has been reported by McCrea et al. (1991). In this experiment, the Tromsø transmitter and receiver were oriented to point in the F-region making continuous incoherent scatter measurements. Meanwhile, the remotes cycled between coherent E-region observations and incoherent scatter observations at the common tristatic location in the F-region. This technique has the drawback that no E-region measurements are performed during the times when detailed tristatic data were collected. McCrea et al. (1991) identified a threshold in the Tromsø line-of-sight ion velocity component of 500m/s for the excitation of E-region irregularities. In the work to be presented here, one remote was pointed continuously in the E-region, while Tromsø and the other remote made F-region incoherent scatter measurements. This has the advantage of continuous F and E-region coverage. However, only two EISCAT receivers are employed in making F-region plasma measurements. This requires assumptions to be made about the plasma drift, in order to estimate the drift velocity.

7.2 Active Coscat

The passive experiments (McCrea et al. (1991) and Chapter 5) demonstrated that the correct geometry required for coherent scatter was achieved only at Kiruna and Sodankylä. Thus, as depicted in Figure 7.1, the Kiruna receiver was oriented to give dedicated viewing of E-region irregularities, while Tromsø and Sodankylä made incoherent scatter measurements in the F-region. The Tromsø and Sodankylä pairing was preferred to that of Tromsø and Kiruna since the former measures two ion velocity components that are at a larger separation in angle.

GEOMETRY OF ACTIVE COSCAT EXPERIMENT

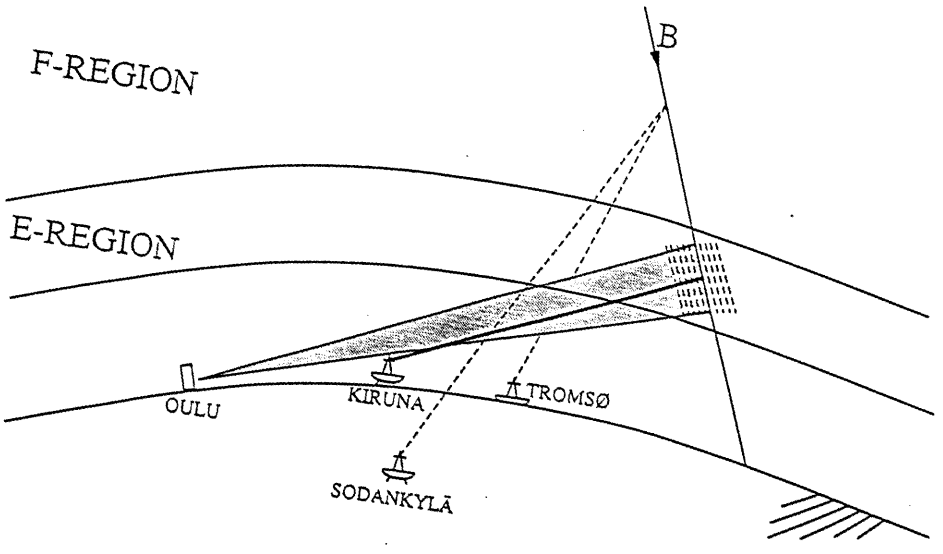

Figure 7.1 A schematic diagram illustrating the geometry of ACTIVE COSCAT experiments.

The F-region measurements of components of the ion velocity are combined to give an estimate of the F-region ExB drift velocity. This then gives an estimate of the E-region ExB velocity (or the electron drift velocity) at the position defined by the magnetic field line that passes between the two points. However, the sketch in Figure 7.1 is somewhat optimistic. The Oulu transmissions contain no timing information and consequently do not allow any range resolution. Hence the exact location of any coherent scatter is unknown and the E-region and F-region positions compared may be on separate field lines.

Another restriction to the data quality is that only two components of the ion velocity are determined at any one time in the F-region. Routine determination of electric fields with EISCAT involves tristatic measurements. These are impossible here since Kiruna is dedicated to E-region observations. In contrast to Chapter Six, where the plasma drift speed was inferred from ion temperature measurements, here a bistatic estimate of the F-region plasma drift velocity is made by assuming the ion velocity parallel to the magnetic field is zero ($V_{||} = 0$). The advantage of a bistatic method over the ion temperature determination, is that it gives an estimate of the flow direction in addition to the magnitude of the plasma drift.

The validity of assuming that the parallel ion velocity is zero has been tested by means of taking an EISCAT CP-2 tristatic data set from which the tristatically determined drift velocity was compared with a bistatic estimate. Figure 7.2 represents a time series of the magnitude of the velocity calculated from tristatic data (full line) together with a bistatic estimate (dashed line) from the measurements taken only from Tromsø and Sodankylä. There is good agreement between the two curves which gives confidence to the adoption of the bistatic estimate in the analysis of COSCAT data for estimates of the magnitude of the drift velocity.

In Figure 7.3 the velocity components defined relative to the magnetic field, as calculated by the two techniques, are compared. The derived velocity consists of a large eastward component and a small northward component. The eastward components derived by the tristatic and bistatic methods agree well. The north bistatic estimate introduces an error of 50m/s towards the south. However, this does not result in any large systematic error in either the magnitude or direction of the inferred velocity.

To investigate the possible errors, consider the angle ϕ as that between the north and the direction of the plasma drift, all in the plane perpendicular to the magnetic field. The angle ϕ is then equal to the inverse tangent of V_E/V_N. If the actual velocity

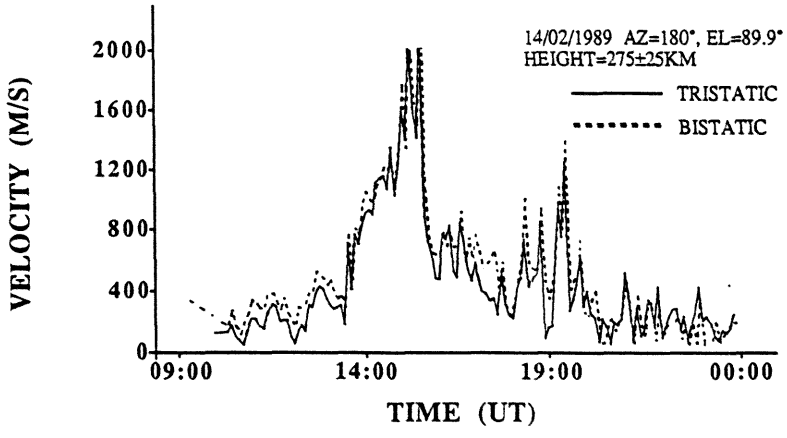

Figure 7.2 A comparison between tristatic and bistatic estimates of the ion drift speed.

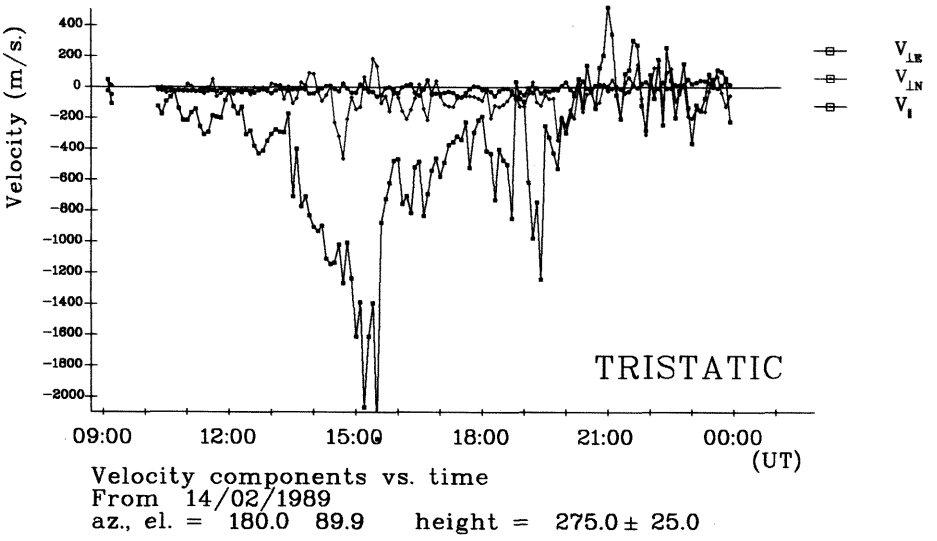

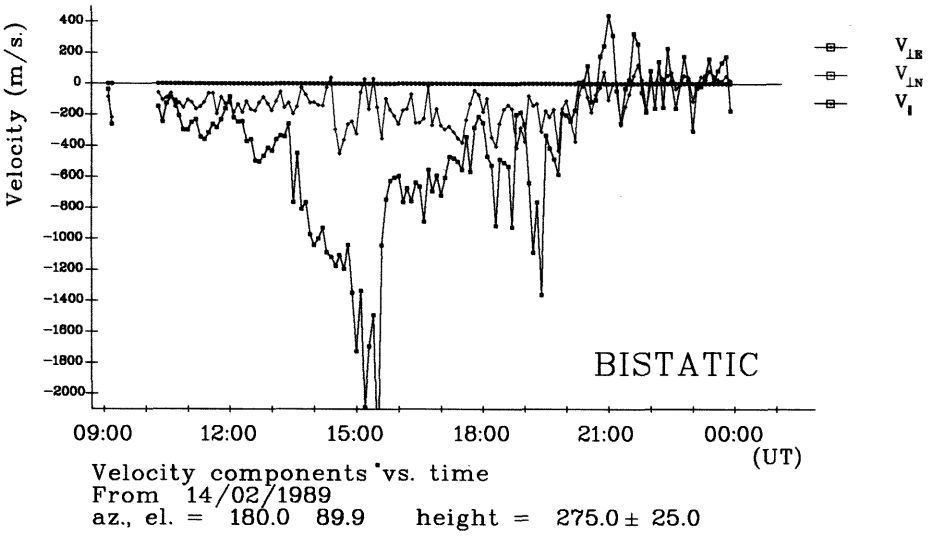

Figure 7.3 A comparison between tristatic and bistatic estimates of components of the ion drift velocity relative to the Earth's magnetic field.

component ratio measured is $p(V_E/V_N)$, owing to an under- or over-estimation of one of the velocity components, then the error in the angle will be :

$$\Delta\phi = \tan^{-1}(V_E/V_N) - \tan^{-1}(pV_E/V_N) \qquad (7.1)$$

This error is plotted in Figure 7.4 as a function of the true ratio between the velocity components, for different values of 'p'. The comparison of plasma drift components in Figure 7.3 revealed a five-fold overestimate of the V_N component, this corresponds to p=0.2. In the worst case this corresponds to an error in the direction of plasma flow of $\pi/4$ when the east and north components are of the same magnitude.

Errors arise when deviations of the parallel ion velocity from zero occur. Figure 7.5 is a plot of the angle error against increasing parallel ion velocity. This error depends on the size and orientation of the components measured by the Tromsø and Sodankylä receivers and on the true plasma drift velocity. Figure 7.5 was constructed by inputting typical values for these parameters from the data illustrated in Figures 7.2 and 7.3. For the values plotted the angle error is small < 0.1 radians (~6°) for parallel velocities up to 500m/s.

The angle between the magnetic field line and the EISCAT receiver look directions in the ACOS experiment is larger (more nearer perpendicular) than those in the CP-2 experiment. Hence the errors are expected to be less significant when the technique is applied to ACOS, where the contribution of the parallel ion velocity to the measurements is smaller.

The active experiments that have so far been undertaken are detailed in the following, Table 7.1:

ACTIVE COSCAT EXPERIMENT	BACKSCATTER OBSERVED
JUNE 1990	14/6 (see McCrea et al. 1991)
MARCH 1991	8/3, 9/3, 13/3
JUNE 1991	24/6
MARCH 1992	no backscatter

Table 7.1

Within this data set four periods of strong backscatter can be identified. The longest period of continuous backscatter was observed on the 9th of March 1991. Figure 7.6(a) depicts time series of the variation of the parameters measured during this event. It is

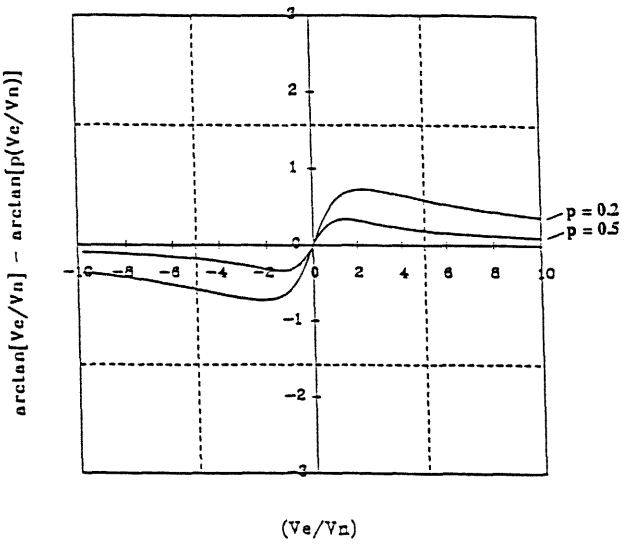

Figure 7.4 The error in angle estimations arising due to errors in the derived components. The error is plotted as a function of the true ratio between the east and north components of the velocity relative to the magnetic field (V_E/V_N). Each curve on the graph corresponds to different values 'p', where 'p' corresponds to an under- or over-estimate of one of the components, giving a measured ratio $p(V_E/V_N)$.

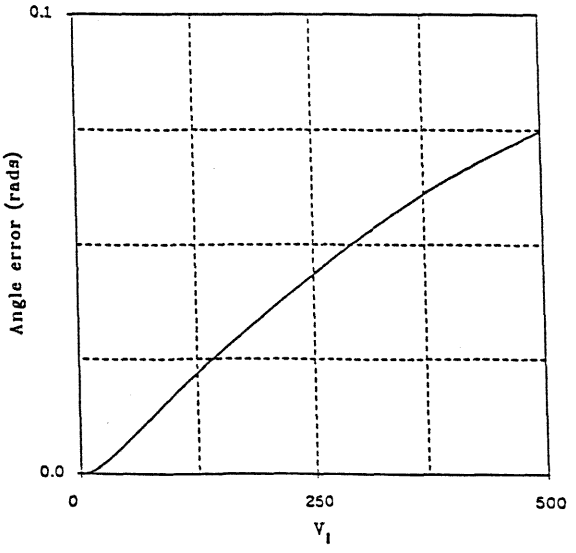

Figure 7.5 The error in angle estimation as a function of V_{II}.

instructive to focus on this data set initially and then collate and discuss the other results later.

In Figure 7.6(a) the square boxes designate values of the COSCAT measured parameters and the full lines are parameters determined by the EISCAT radar. The top panel displays both the coherent backscatter power measured by the Kiruna receiver and the F-region incoherent scatter power as detected from Tromsø. In the bottom panel the irregularity phase speed is plotted along with an estimate of the component of the plasma drift speed in the direction of the Kiruna line of sight. Coherent scatter is first detected at 03:12 UT and persists until 03:36 UT. The gaps that occur between these times in the data correspond to when the Oulu transmitter was switched off, a feature of the experiment design, and confirm that the EISCAT receivers were detecting the Oulu signal. The onset of coherent scatter corresponds to power values of -20dB and which increase up to about 5dB. The strongest scatter occurs from 03:15 UT to 03:18 UT. Figure 7.6(b) is a plot of each spectrum measured every 5s drawn in a continuous stack, with time running from bottom to top. This clearly illustrates the turn on of scatter at 03:12 UT. The subsequent spectra are strong and narrow.

The incoherent scatter power exhibits interesting behaviour during the occurrence of coherent scatter. The power received by incoherent scatter gives an indication of the electron density, in this case at an F-region altitude of approximately 275km. At the onset of strong backscatter (03:12 UT) the incoherent scatter power decreases indicating a decrease in the F-region density. Such depletions have been identified in other studies. For example, in the E-Region Rocket/Radar Instability Study (ERRRIS) (Pfaff et al. 1992) it was found a depletion in the electron density often accompanies strong electric fields. This is of relevance to the COSCAT observations since the appearance of coherent scatter requires the presence of strong electric fields (a 5-15V/m threshold is often quoted e.g. Kustov et al. (1989) and references therein).

7.3 Summary of other data

As for the experiment of 9/3/91 most spectra observed exhibit characteristics common to irregularities generated by the two-stream instability. Exceptions are detailed below. Time series for the other data sets are displayed in Figures 7.7(a) to (c). The form of these figures are the same as Figure 7.6(a).

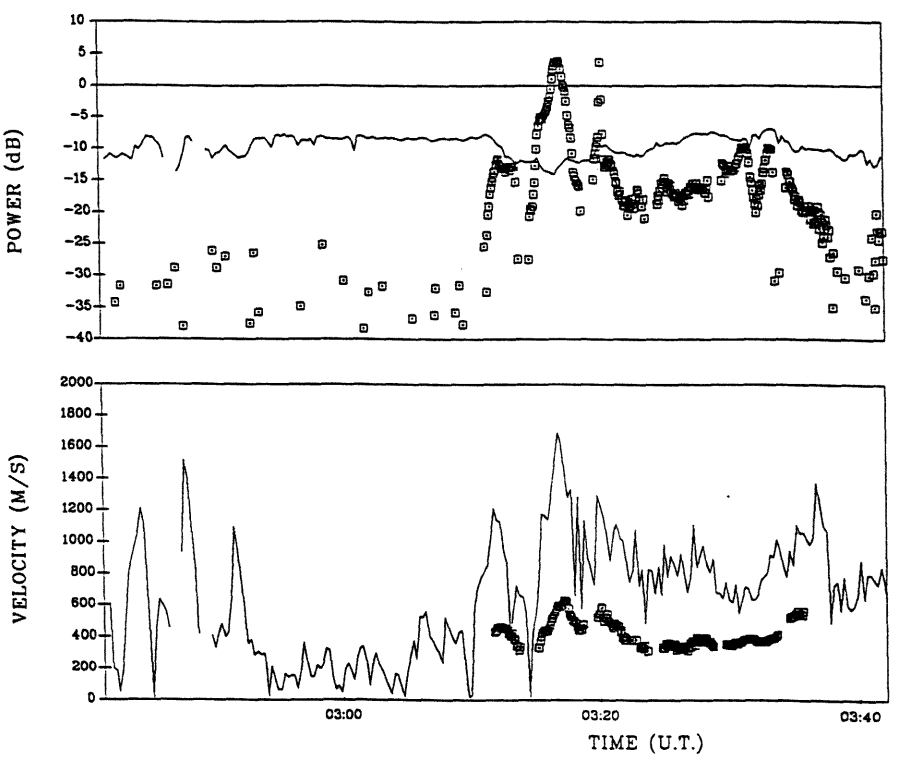

Figure 7.6(a) Time series of irregularity parameters measured in the COSCAT experiment (discrete points) and incoherent scatter measurements from EISCAT (full lines). The top panel illustrates the power scattered from the E-region irregularities received at Kiruna and the power measured by the Tromsø incoherent scatter radar from the F-region plasma. The bottom panel contains the irregularity phase speed and the component of the F-region plasma drift speed resolved in the direction of the Kiruna radar line-of-sight. These data are taken from the experiment of 9/3/91.

FIGURE KEY	Incoherent scatter measured parameter	Coherent scatter measured parameter
	———	●
Top Panel	Tromsø power	Kiruna power
Bottom Panel	Eiscat determined plasma drift component	Irregularity phase speed measured at Kiruna

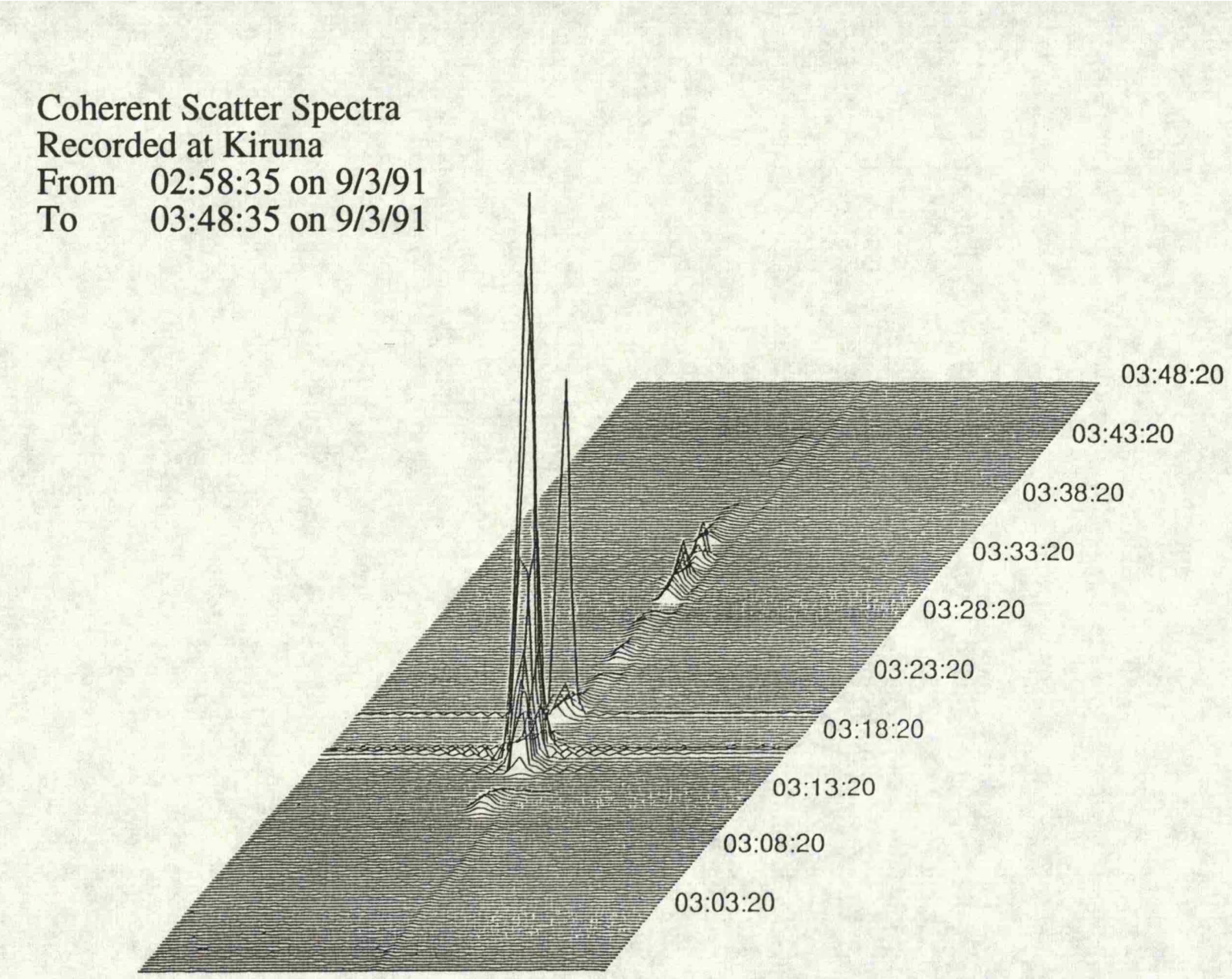

Figure 7.6(b) A time series of the irregularity power spectra observed on the 9/3/91.

8/3/91 Figure 7.7(a)

An interval of backscatter is observed at the start of the experiment at 23:30 UT up until 00:00 UT. During this time the average phase speed is 300m/s. Backscatter is observed during the next two hours but its incidence is very sporadic. The phase speeds also increase and fall in periods of 5 to 10 minutes. The fluctuation of the phase speed may be produced by Alfvén wave activity, e.g. Walker et al. (1979). Decreases are observed in the Tromsø measured backscatter power during the occurrence of backscatter. Throughout the interval there are large variations in the plasma drift component velocity with changes of the order of 1000m/s in periods of a few minutes.

13/3/91 Figure 7.7(b)

Here a continuous period of backscatter exists between 01:20 and 01:50 UT. Again the occurrence of backscatter is accompanied by a depletion in the incoherent scatter return power measured at Tromsø. A number of low phase velocities, approaching zero, are observed especially near 1:40 UT. Scrutiny of the backscatter spectra reveals that these occur due to double-peaked spectra. This indicates the presence of irregularities moving in opposite directions along the Kiruna beam. The phase speed calculated is the average of the phase speeds of the two groups of irregularities and consequently close to zero. Such circumstances may arise when the COSCAT scatter volume contains a shear in the plasma flow.

24/6/91 Figure 7.7(c)

Just 10 minutes of steady backscatter is observed during this experiment. The backscatter commences at 16:10 UT. The subsequent changes in the irregularity phase speed are then well correlated with the changes in plasma drift speed. Outside this period, no other coherent scatter is observed. There are no depletions in the Tromsø power. The variation of all the parameters is smooth.

7.4 Quantitative results

To quantify the conditions under which backscatter occurs the average background plasma drift parameters have been calculated for each experiment in which backscatter was observed. These are the plasma drift speed, the angle between the look direction of the Kiruna receiver and the direction of the plasma drift (flow angle) and the component of the plasma drift in the Kiruna look direction. The average values and their standard deviations have been calculated for each of these parameters during the whole

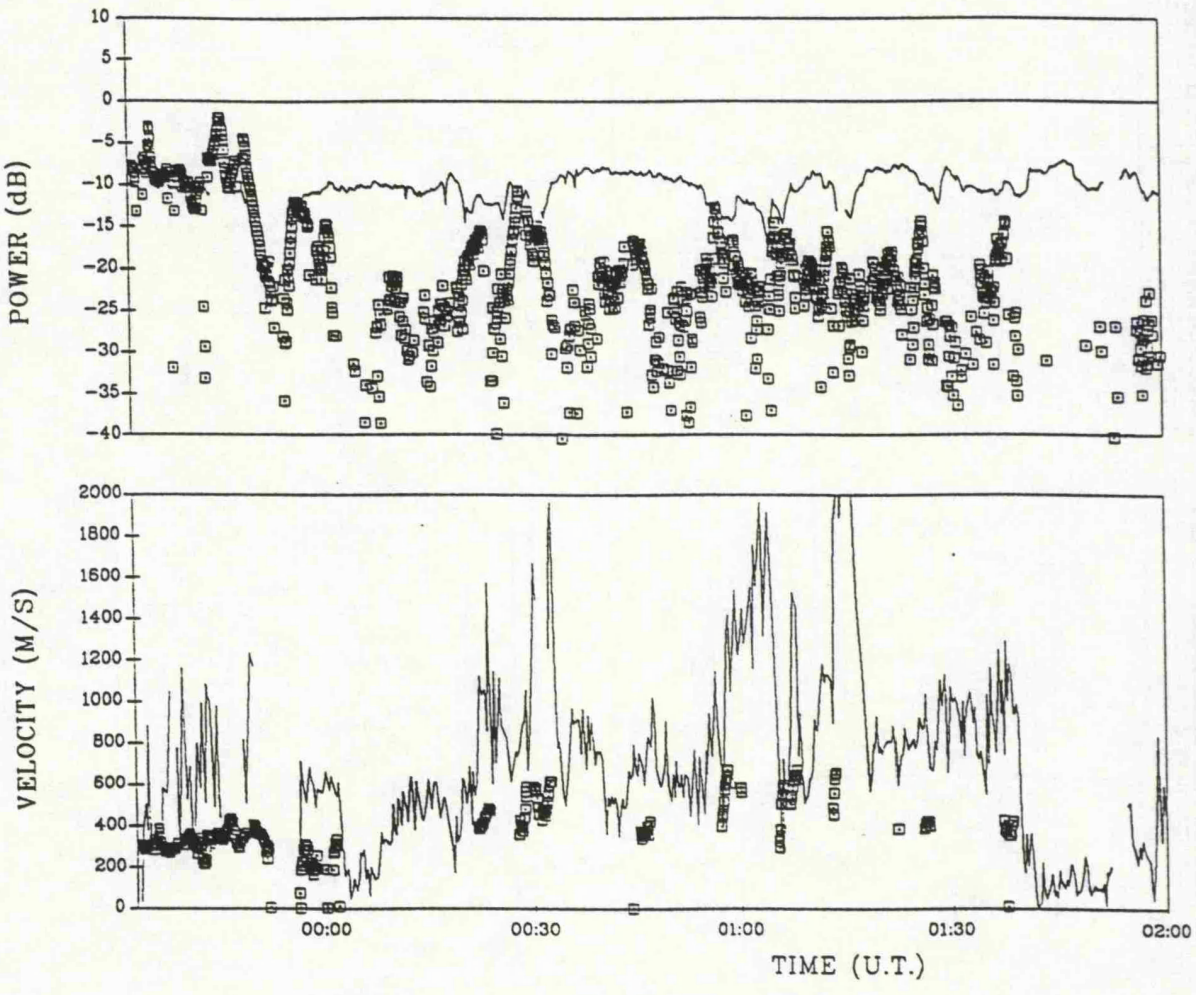

Figure 7.7(a) As Figure 7.6(a) but for data from 8/3/91.

FIGURE KEY	Incoherent scatter measured parameter	Coherent scatter measured parameter
	———	●
Top Panel	Tromsø power	Kiruna power
Bottom Panel	Eiscat determined plasma drift component	Irregularity phase speed measured at Kiruna

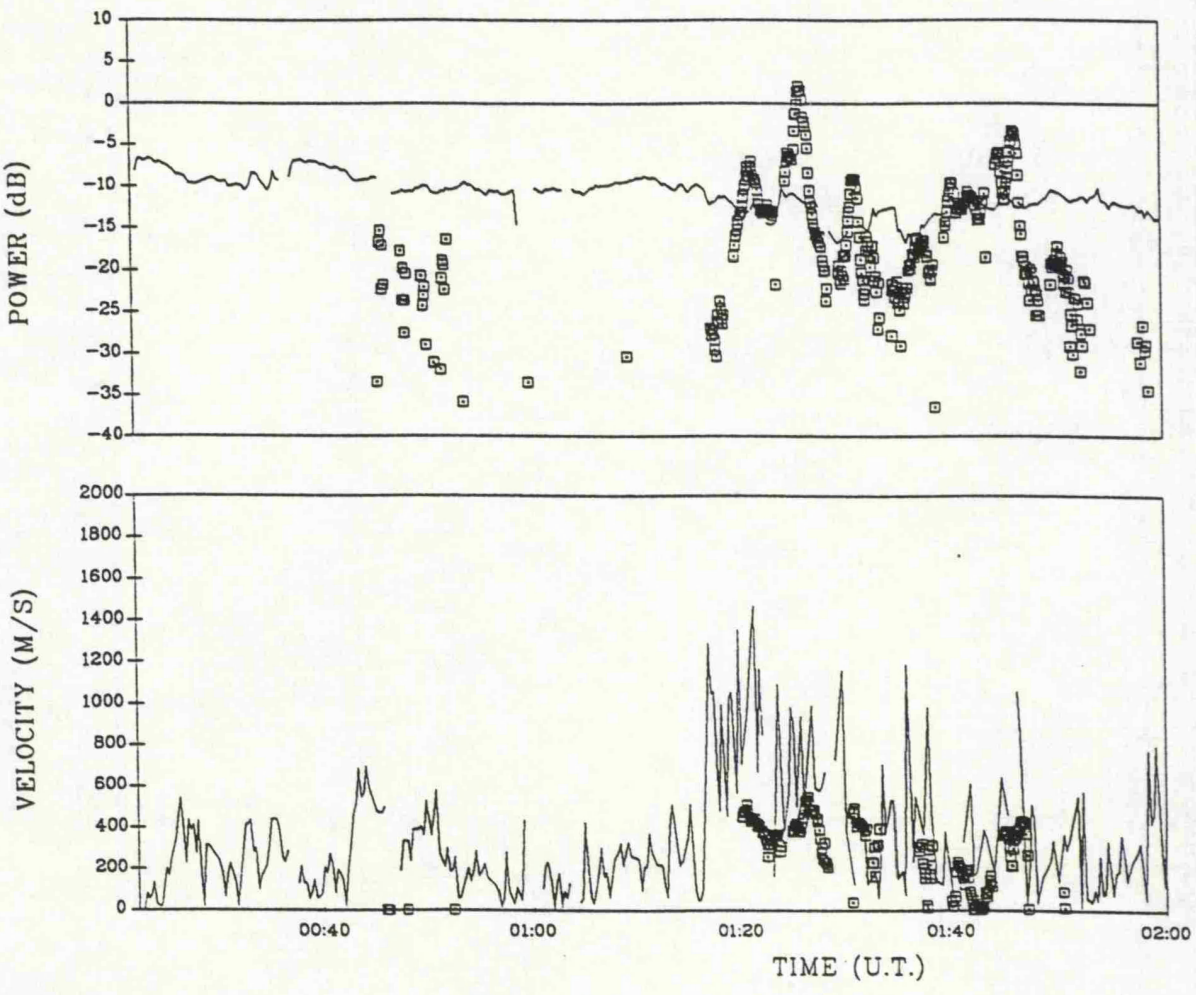

Figure 7.7(b) As Figure 7.6(a) but for data from 13/3/91.

FIGURE KEY	Incoherent scatter measured parameter	Coherent scatter measured parameter
	———	⊡
Top Panel	Tromsø power	Kiruna power
Bottom Panel	Eiscat determined plasma drift component	Irregularity phase speed measured at Kiruna

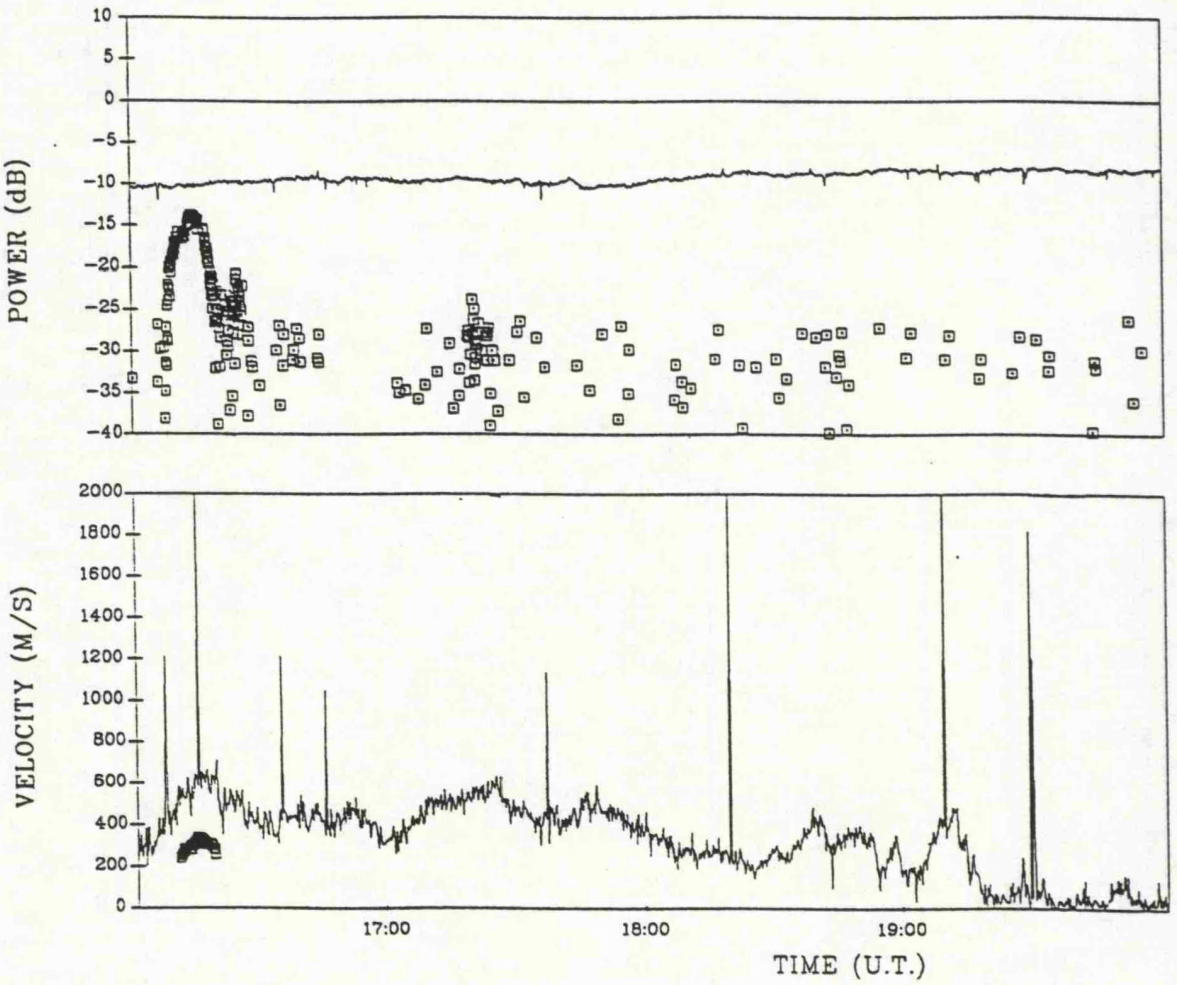

Figure 7.7(c) As Figure 7.6(a) but for data from 24/6/91.

FIGURE KEY	Incoherent scatter measured parameter	Coherent scatter measured parameter
	———	■
Top Panel	Tromsø power	Kiruna power
Bottom Panel	Eiscat determined plasma drift component	Irregularity phase speed measured at Kiruna

experiment, times when no backscatter were observed and times when there was backscatter. The results are summarised in Table 7.2:

KEY the numbers given below are **average value ± standard deviation**			
8/3/91	**WHOLE EXPERIMENT**	**BACKSCATTER**	**NO BACKSCATTER**
Drift Speed (m/s)	1400 ± 1100	1800 ± 1300	1300 ± 900
Flow angle	51° ± 22°	50° ± 21°	51° ± 23°
Drift component (m/s)	700 ± 400	800 ± 350	650 ± 400
9/3/91			
Drift Speed (m/s)	1200 ± 800	1500 ± 800	900 ± 600
Flow angle	47° ± 22°	43° ± 20°	53° ± 24°
Drift component (m/s)	650 ± 400	850 ± 250	400 ± 300
13/3/91			
Drift Speed (m/s)	1400 ± 1400	2400 ± 1700	1100 ± 1000
Flow angle	67° ± 20°	70° ± 20°	65° ± 20°
Drift component (m/s)	350 ± 300	550 ± 400	300 ± 200
24/6/91			
Drift Speed (m/s)	500 ± 400	900 ± 600	500 ± 350
Flow angle	37° ± 23°	42° ± 10°	37° ± 23°
Drift component (m/s)	350 ± 200	600 ± 250	350 ± 200

Table 7.2

Summarised in the table are the average drift speed, flow angle and component of drift speed in the direction of the Kiruna line-of-sight. The standard deviation of the data about these averages is also given. This indicates the variability of the parameters during the period of observation. These statistics have been calculated for three cases; all periods of the experiment, times when there was backscatter and times when there was no backscatter.

The mean drift speed is always greater during periods of backscatter compared with periods when no backscatter is observed. Reduction of the average flow angle is observed for 8/3/91 and the 9/3/91 during backscatter while there is an increase of flow angle in the experiments of 13/3/91 and 24/6/91 during backscatter. The net effect on the component of the plasma drift in the direction of the Kiruna line-of-sight is always an increase in the drift component for periods of backscatter.

The average values calculated for the line-of-sight drift component give an indication of the threshold conditions for the excitation of 16cm irregularities. To establish the threshold conditions more accurately the value of the line-of-sight drift component at the onset (or discontinuation) of backscatter needs to be determined. Scrutiny of the time series for the four experiments (the 8/3/91, 13/3/91 and 24/6/91 data are presented in Figures 7.7(a),(b) and (c)) being discussed gives the following approximate thresholds (an average of onset and turn off values for coherent scatter):

Experiment	Threshold component speed (m/s)
08/3/91	400
09/3/91	600
13/3/91	500
24/6/91	500

Table 7.3

To calculate the flow angle average it was necessary to take the acute angle between a line in the direction of the plasma drift speed and a line in the direction of the Kiruna line-of-sight. This forced all the flow angles in the averaging procedure to vary from 0° to 90°, the limits in this range corresponding to flows parallel and perpendicular to the Kiruna line-of-sight respectively. Thus no distinction is made between flows towards and away from the radar. Time series of the flow angle for each experiment are illustrated in Figure 7.8. These indicate the occurrence of swings in the flow direction from 0° to 180°, e.g. in the initial periods of the 9/3/91 and 13/3/91 data. No backscatter is seen during such periods of large variation in flow direction. The times of occurrence of backscatter are signified on the time series by the horizontal bars. The backscatter generally occurs during periods of smaller variations in flow angle.

The flow angles are often large (up to 70°). Under these circumstances the generation of two-stream waves is still possible, provided the drift speed is large, e.g. as in the experiment of 13/3/91. At other times there are instants of high velocity magnitude, small flow angle and no coherent scatter, for example between 02:40 UT and 03:00 UT in 9/3/91. There are a number of reasons that could account for this. Firstly, the cross-section of E-region irregularities is also dependent on the amplitude of the electron density fluctuation and the background electron density (see Equation 5.12). There are also the experimental uncertainties in not knowing the exact location of the E-region scatter. The two sets of measurements are possibly on different field lines. During the periods where the data are inconsistent, there are large swings in the estimated flow angle, either simultaneously or in adjacent measurements. This implies

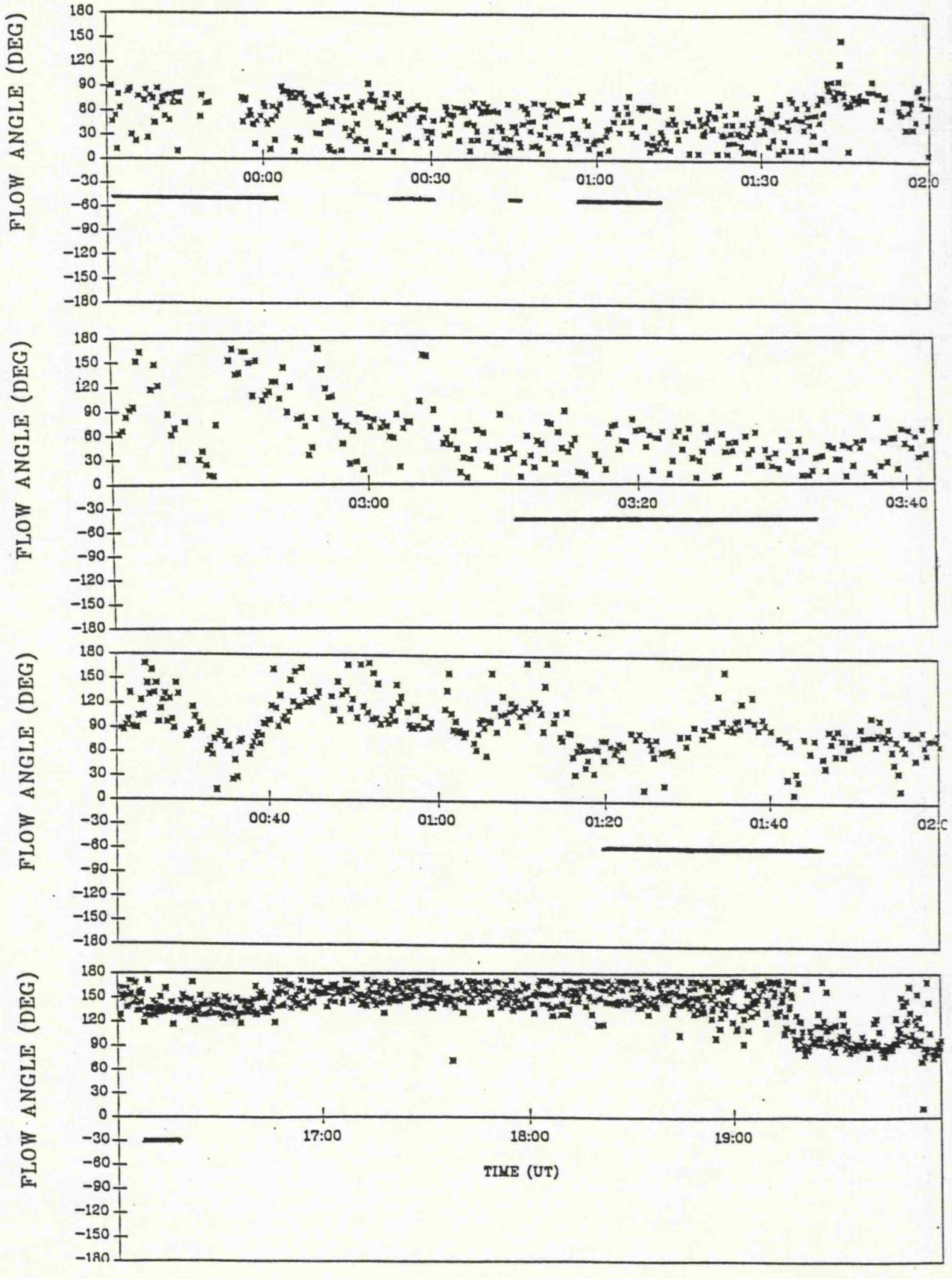

Figure 7.8 Time series of the flow angle measured during each experiment; from top to bottom, 8/3/91, 9/3/91, 13/3/91 and 24/6/91. The horizontal bars mark the times during which backscatter was observed.

there is either great temporal variation in the local plasma drift or that the variation is spatial and the temporal changes arise as the pattern drifts through the radar beams. Under these circumstances it would not be implausible to suggest that the flow regimes observed in the E and F-regions are different. Furthermore, when the coherent scatter does commence the flow angles fluctuate less.

7.5 Comparison with theory

As elucidated in the previous chapter, the phase speed of E-region irregularities is sensitive to the altitude at which they occur. There is no altitude information available in the present COSCAT experiment and this makes it difficult to compare the measured phase speeds with a predicted speed for the electron drift speed at which the measurement was taken. This limits the interpretation of phase speeds for COSCAT in a manner similar to that for SABRE.

In Figure 7.9 the data from 9/3/91 is plotted as a graph of the average phase speed in a 100m/s drift velocity bin against the estimated electron drift speed. Following the procedure in Chapter 6, superimposed are theoretical curves from Robinson and Honary (1990), of the variation of the irregularity phase speed against the elèctron drift speed. The data fit between the theory curves and are consistent with backscatter from an altitude below 100km in the lower E-region.

7.6 Calibration

A good comparison can be made between theory and the experimental data for the results obtained on the 9/3/91. The data quantity in the other experiments is unfortunately insufficient to allow a statistically valid comparison. However, all the data can be combined in order to derive a calibration curve for the COSCAT experiment, following the procedure adopted for Wick in Chapter 6 (after Nielsen and Schlegel (1985)). All data available are plotted in Figure 7.10. The ordinate is the average irregularity phase speed measured in 300m/s drift speed bins. A fit of the form of Equation 6.7 has been applied to the first six data bins. The form of the calibration curve is invalid for high drift speeds since here, as predicted by theory, the relationship between the phase velocity and plasma drift speed is not similar to a quadratic. The theory curves of Figure 2.2 begin to flatten off as the plasma drift speed increases above 2000m/s. The data is not inconsistent with this behaviour. Also at the high drift speeds the number of data points is small in each bin, this is depicted in the histogram of Figure 7.11. Statistical fluctuations in the data will be significant at high drift speeds.

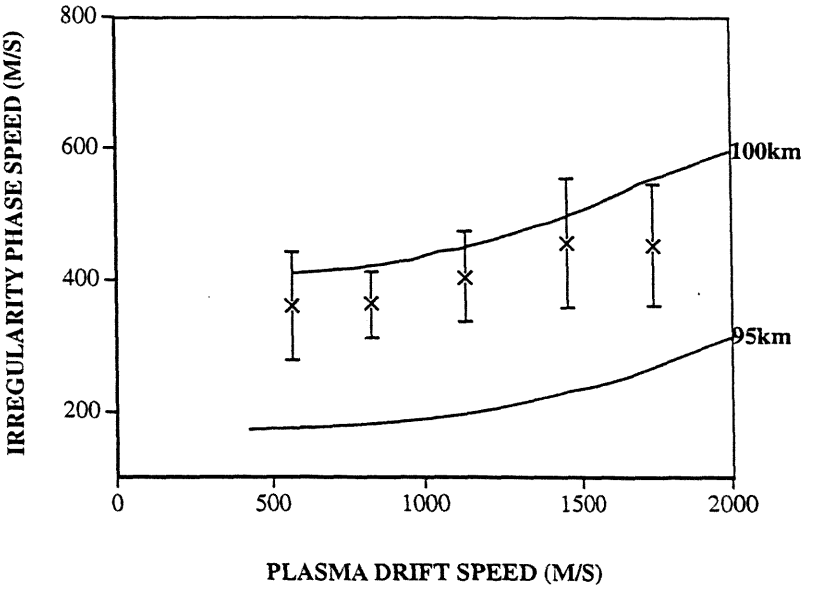

Figure 7.9 The iregularity phase speed plotted against the estimated drift speed for the experiment of the 9/3/91. A curve from the kinetic theory of Robinson and Honary (1990) has been superposed for an altitude of 100km.

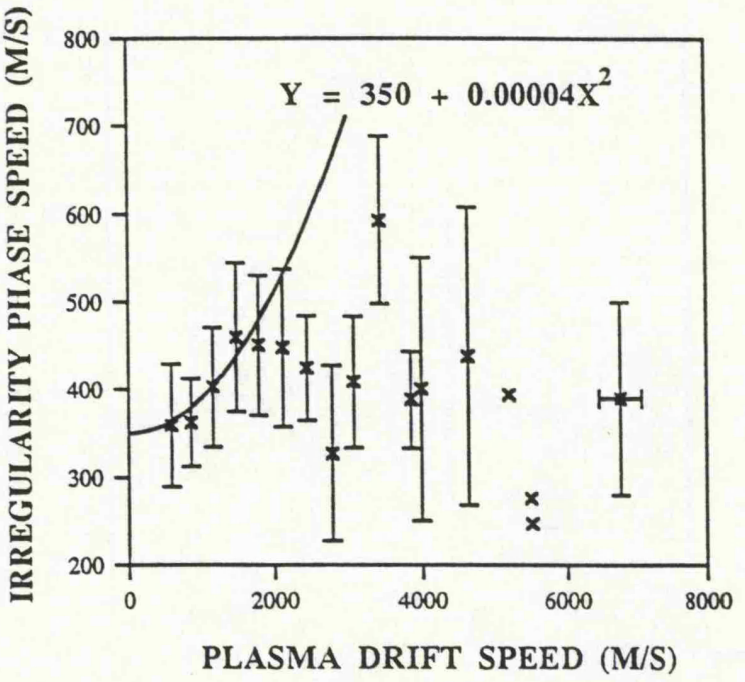

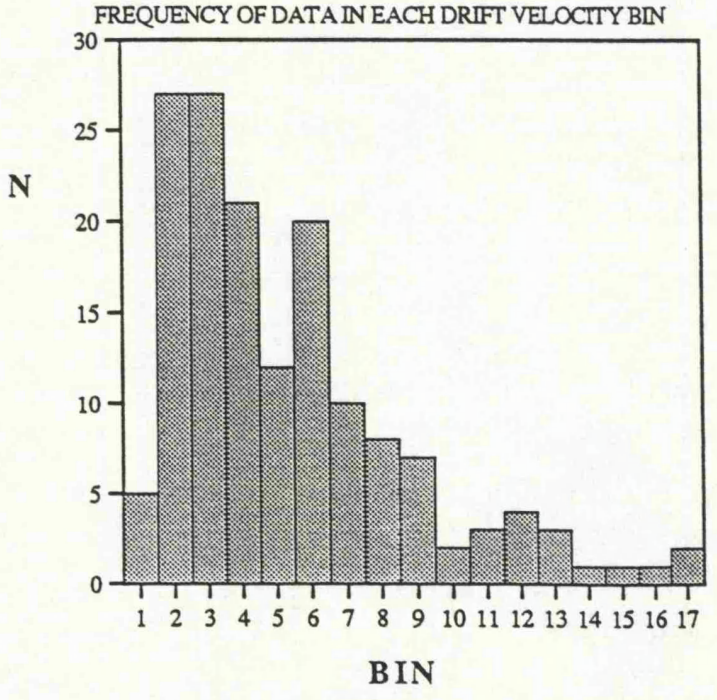

Figure 7.10 (upper panel) is a plot of the iregularity phase speed against plasma drift speed for all the ACTIVE data. A calibration curve has been fitted through the data points up to 2000m/s drift speed. Figure 7.11 (bottom panel) illustrates the number of data points in each drift velocity bin.

7.7 Summary

Under the existing constraints of the COSCAT viewing geometry, comparisons have been made between the characteristics of 16cm irregularities measured with COSCAT and the magnitude and direction of the plasma drift velocity with EISCAT. Measurements of the plasma drift speed were achieved by means of a bistatic estimate. This technique was found to give valid results when compared to an EISCAT tristatic data set. Threshold conditions in the magnitude of the plasma drift velocity component in the direction of propagation of the irregularities had to be met before irregularities were excited. Analysis of the relationship between the phase speed and plasma drift speed implied that the backscatter originated at an altitude just below 100km. These results will be discussed in relation to SABRE and STARE in the following and concluding chapter.

Chapter Eight

CONCLUSIONS AND FUTURE WORK

8.1 Introduction

The characteristics of auroral plasma irregularities have been investigated at a range of different irregularity wavelengths with coherent scatter observations from principally the Halley, Wick and COSCAT radars. The research has involved the analysis of the statistics of coherent scatter spectral moments from large numbers of observations and also case studies, where irregularity characteristics were compared with background plasma parameters obtained from other instruments such as EISCAT. A brief summary is now presented of the most important results obtained and the main conclusions are highlighted.

8.2 Drift speed dependence of phase speed

In experiments conducted with both SABRE and COSCAT (Chapters 6 and 7 respectively) the relationship between the irregularity phase speed and the plasma drift velocity was investigated. An understanding of this relationship is very important since from coherent scatter radar measurements information about the plasma drift motion for geophysical research is inferred. Furthermore, the investigation provided a unique opportunity to compare the behaviour of the irregularity phase speed with respect to the plasma drift speed at two different irregularity wavelengths.

The observations (summarised in Figures 6.11 and 7.9 for SABRE and COSCAT) were consistent with the theoretical predictions of Robinson and Honary (1990). This is a kinetic theory of the modified two-stream instability and predicts the phase speed of a Type (I) irregularity is highly sensitive to the altitude of coherent scatter, the phase speeds increase with the plasma drift speed and the phase speed at a given plasma drift speed is larger for shorter wavelength irregularities. The six EISCAT-SABRE experiments indicated that the theory fits well to the data for a range of different altitudes in each experiment. The comparison of active COSCAT data to the theory suggested the coherent scatter originated from a lower altitude (< 100km) than that commonly observed with SABRE and that phase speeds, at comparative drift speeds, were higher at the shorter irregularity wavelength.

These phase speed differences are evident in a comparison between the data sets that employs the calibration curve:

$$V_{ph} = a + bV_D^2 \qquad \text{valid for } V_D < 1600\text{m/s} \qquad (8.1)$$

first suggested by Nielsen and Schlegel (1985) in their analysis of STARE data. The fitted parameters for COSCAT, SABRE and STARE are listed below:

	a	b	$V_{ph}(400)$
COSCAT	350	0.00004	356
SABRE/EISCAT	320	0.00005	328
STARE/EISCAT	300	0.00011	318

Table 8.1

The last column is the phase speed of irregularities that would be excited at a plasma drift speed of 400m/s. The kinetic calculations of Robinson and Honary (1990) suggested that irregularities at 1m would propagate at phase speeds 10% above the ion acoustic speed, at 16cm wavelength (e.g. COSCAT) the prediction is closer to 20% above the ion acoustic speed. This behaviour is reflected by the figures in Table 8.1 and there is good quantitative agreement if the ion acoustic speed is of the order of 300m/s, which is a reasonable assumption for a low plasma drift speed such as 400m/s.

8.3 Observations on the spectral width

The spectral width was found to be proportional to the wave number raised to a power of 1.2 ± 0.4 (see Figure 5.4). Hanuise et al. (1993) demonstrated that Gaussian and Lorentzian spectra have a k^1 and k^2 dependence respectively. The result is clearly closer to the k^1 theoretical bound. A k^2 dependence arises if the lifetime of the irregularities is short and their rapid decay causes the Doppler broadening. The observed k-dependence suggests that the irregularities comprise stable waves and the spectra are broadened due to fluctuations in the background plasma flow which modulate the phase speed of the irregularities.

For the Wick data, the backscatter power is observed to decrease as the spectral width increases. This behaviour was successfully modelled by superposing the scattered signal from a population of irregularities with decay rates smaller than the

sampling rate of the radar receiver. The spectral width exhibited a minimum at phase speeds of the order of the ion acoustic speed for the Wick and COSCAT data and a minimum near zero phase speed for the Halley data. For Type (I) irregularities the increase in spectral width with phase speed can be accounted for by the dependence of anomalous broadening of the spectrum on the plasma drift speed. The minima in the Wick and COSCAT data correspond to a transition region between Type (II) and Type (I) irregularities observed as the phase speed increases. The Halley observations are composed of predominantly Type (II) irregularities. The increase in spectral width with phase speed may correspond to faster decay rates of Type (II) irregularities as the phase speed increases, as suggested by the irregularity dispersion relation, or may reflect changes in the level of fluid turbulence as the plasma drift speed increases. This can only be resolved when independent measurements of the plasma drift become available in conjunction with further irregularity observations at HF.

8.4 Morphology of coherent scatter power

A study of the spatial morphology of backscatter power was carried out with data from the Wick radar. The backscatter power distribution is typically non-uniform in range and azimuth. For Wick data, it was found that a magnetic aspect sensitivity of 5dB/deg was required to model the observed azimuthal distribution. To account for the range variation, the backscatter cross-section per unit volume had to increase with range. A further result of the Wick modelling work implied that it was often incorrect to consider the radar beams to be only as wide as the spatial separation of their 3dB points. Strong scatterers outside these 3dB points can affect the measurement of power, which is usually completely attributed to irregularities in that beam's bore-sight. The fascinating and important outcome of the modelling work is that smooth distributions of irregularities can exhibit apparent structure which is just a function of the beam geometry. In the operation of radars that map large areas of the ionosphere it is important to establish what structure is observed under quiescent conditions if other phenomena that manifest themselves in radar power returns are to be interpreted correctly.

8.5 Characterisation of radar observations

The majority of observations from each radar system were readily categorised in terms of a common irregularity type. The Wick and COSCAT radars observe Type (I) irregularities while the Halley radar detects Type (II) irregularities, these differences are attributed to the observing geometry of each radar system.

Problems exist with categorising spectra, which is a matter of a definition that relies on the mean Doppler shift of the spectrum relative to the ion acoustic speed. In most experiments there is no independent measurement of the ion acoustic speed. The fact that new spectral shapes have been identified in high latitude observations (Type (III) and Type (IV)) indicates that the classes may need to be rationalised, especially since the new types may just be modifications of the old. The distinctive properties of each irregularity type are determined by the generating plasma instability. Theoretically Type (I) and Type (II) irregularities are defined by the same dispersion relation with the imaginary part containing two terms, corresponding to the two-stream and gradient drift instabilities, Equation 2.3. In definitive examples of Type (I) or Type (II) spectra the appropriate term dominates. The situation is less clear if both terms make a significant contribution. Thus it was not unexpected to find mixed regions of irregularity types in the power - width - velocity profile of Figure 5.16.

8.6 Geophysical implications of the data

As summarised above, the key issues studied in this thesis have been concerned with the plasma physics of auroral irregularities. However, it is also important to point out the geophysical results that are evident in the experimental data.

The histograms of Figure 5.1 (a) to (e) summarised the diurnal occurrence of irregularities for each radar. All the distributions were non-uniform and contained localised minima. The minima correspond to times when the geophysical conditions are less-suited for the production of coherent radar backscatter. The evening minimum (MLT) corresponds to the radar field of view moving from the dusk to dawn convection cell. During this time there are rotations in the plasma flow direction relative to the radar look direction. The broader minimum is located near mid-morning (MLT). This may correspond to the morning reversal. However, during this time the auroral oval is displaced over the polar cap to higher latitudes and thus less coherent scatter is expected.

For Wick and COSCAT the sense of the radar Doppler signal is dependent on the direction of the background plasma flow. This is not the case with the Halley data since the Halley radar look direction is perpendicular to the local L-shells. Because of this, there were differences between the statistics for positive Doppler shift data as compared to negative Doppler shift data in the Wick and COSCAT data sets but not for the Halley radar observations. The most significant difference is that the spread in

spectral widths observed is greater for eastward flows than westward flow. This is apparent in both the Wick (first reported by Schlegel et al. (1986)) and COSCAT data. There are differences between the two flow regimes which may account for this variation. In the nightside region, substorm activity results in field aligned currents. This may lead to a current convective instability that will affect the irregularity growth rates and is a modification to theory that could be pursued. Alternatively, increased particle precipitation may result in additional, small-scale, density gradients in the medium, that will modify the spectral broadening through the gradient drift term, e.g. Farley and Fejer (1975). The scale sizes of these gradients will affect the scales of irregularities that can be generated. In consequence, different wavelength irregularities may not experience the same effects. One definite factor is that there does tend to be greater variation in the eastward flow sector. For example, with Wick there is increased observation of double-peaked spectra that may indicate the presence of shear flows in the scattering volume under inspection.

8.7 Suggestions for future work

Coherent backscatter radar will continue to play a prominent role in studies of ionospheric plasma and the geophysics of the Earth's solar-terrestrial environment. The content of this thesis reflects two areas of endeavour; the statistical analysis of irregularity parameters and the comparison of incoherent scatter data with coherent backscatter radar observations.

Radar parameter analysis techniques rely on a study of ACFs or the backscatter spectrum. Each technique has its own advantages and disadvantages. For example, ACFs allow easy identification of whether the returned power decorrelation is Gaussian or Lorentzian. However, they are poor at identifying multiply peaked spectra. Statistical work that could follow directly from this thesis would include an ACF analysis of the Wick and COSCAT data sets. An analysis of the ACF also facilitates an investigation of the plasma turbulence correlation length as detailed by Hanuise et al. (1993).

Moorcroft (1987) studied the variation of coherent scatter power with respect to the irregularity wavelength. It was impossible to make a quantitative comparison between the Wick, COSCAT and Halley power observations since there is no routine calibration of the power measurements. The power values only have significance in comparison with other measurements made by the same radar system. The absolute power returned would be a useful parameter to measure. It is a difficult technical procedure, since the transmitted power has to be established and the received power

measured for a known input signal. The radar beam pattern has to be accurately modelled or measured. However, under these circumstances it would be possible to calculate an absolute power received per unit volume. This would enable irregularity cross-sections at different wavelengths and for different geophysical conditions to be determined.

The EISCAT-SABRE experiment achieved excellent results in spite of the difficult conditions imposed by the extreme experimental geometry. In fact, the success of the ion temperature method in estimating the plasma drift speed should support the method's application to other experiments. There is still potential for further exploitation of the ACTIVE COSCAT experiment. The simultaneous E-region observation of coherent and incoherent scatter is not possible with the current geometry. However, relocation of the transmitter, now at Oulu, to facilitate this goal is conceivable. A detailed study of possible locations should be undertaken.

It is evident that progress in this field can best be achieved with complementary measurements. Measurements such as those in the EISCAT-SABRE comparison, ACTIVE COSCAT experiments and from previous workers (e.g. Nielsen and Schlegel (1983), Farley and Providakes (1989), Haldoupis and Schlegel (1990), Kofman and Nielsen (1990)) were able to confirm the non-linear behaviour of the phase speed of Type (I) irregularities with respect to the plasma drift speed and its relationship to the ion acoustic speed. The empirical relationship derived between the phase speed and plasma drift speed for SABRE, COSCAT and STARE (Nielsen and Schlegel (1985)) are of value for researchers applying coherent backscatter radar data to geophysical studies. A number of suggestions can be made as regards further experiments. The simultaneous measurement of irregularities in the same volume at different radar frequencies is a natural advance to the multifrequency data studied here. This would give unparalleled measurements of the variation of power, phase speed and spectral width with frequency. Ideally such measurements would be made along the same direction (all the radars co-located) and from different directions. To support the operation of HF radars, electron density profiles need to be measured. This is necessary to allow accurate ray tracing of the HF ray paths in order to establish the location of the scattering irregularities.

Future radar experiments include the construction and deployment of HF radars in the Super Dual Auroral Radar Network (SuperDARN, e.g. Greenwald 1992). This radar system will give almost global coverage of both the E-region and F-region ionosphere at auroral latitudes. SuperDARN holds many exciting prospects for research in both plasma physics and geophysics. The need to understand irregularity

measurements is more important than ever if these studies of the auroral ionosphere are to be optimised.

APPENDIX A

WICK: SIMULATION OF BACKSCATTER INTENSITY.

The backscatter power was calculated for each range and beam position using the following equation:

$$P(\text{range,beam}) = \frac{P_0 L(R) W(R)}{R_1^2 R_2^2} e^{\frac{-(ALT-110)^2}{200}} \Delta V \sum_{AZ} \sum_{EL} F(\delta) H(\vartheta) e^{\frac{-EL^2}{72}} e^{\frac{-AZ^2}{2}} \qquad (A1)$$

It is based upon the radar equation of 3.14 with the functional forms adopted being written explicitly. The range of each position is equal to R_1 (=R_2 for backscatter).

The radar beams were given Gaussian sensitivity profiles in azimuth and elevation.

$$e^{\frac{-EL^2}{72}} e^{\frac{-AZ^2}{2}} \qquad (A2)$$

Aspect angle sensitivity of n dBs per degree:

$$F(\delta) \propto 10^{-0.1n\delta} \qquad (A3)$$

Flow angle sensitivity from Oksman et al. (1986), d=4.6 André (1983)

$$H(\vartheta) \propto e^{-d\sin^2\vartheta} \qquad (A4)$$

Lloyd's mirror effect Mattin and Jones (1986)

$$L(R) = 1 - 0.2e^{-(\text{Range number} - 25)^2} \qquad (A5)$$

Distribution of irregularities. A Gaussian density profile with height was modelled and a function defining the variation with range W(R) was included.

$$W(R) e^{\frac{-(ALT-110)^2}{200}} \qquad (A6)$$

The function W used in the successful simulation was a step function that turned the irregularities on at a range R_t from the radar.

$$W(R) = \frac{1}{1 + e^{R_t - R}} \qquad (A7)$$

P_0 was an arbitrary value that could be varied to scale the results to appropriate power levels. The summation involved adding the contributions from each position in azimuth and elevation at a given range. The step length in azimuth and elevation was decreased as the range increased in order to keep the volume elements constant in size at a given range. The volume elements were taken as:

$$\Delta V = \frac{4}{3}\pi\left(R_2^3 - R_1^3\right)\cos(EL)d\theta d\phi \quad \text{where } R_2 = R_1 + 15 \text{ (km)} \qquad (A8)$$

References

Abel W. G. and Newell R. E. (1969) 'Measurements of afternoon radio aurora at 1295MHz' J. Geophys. Res. 74 231-245

André D. (1983) 'The dependence of the relative backscatter cross-section of 1-m density fluctuations in the auroral electrojet on the angle between electron drift and radar wave vector' J. Geophys. Res. 88 8043-8049

Axford W. I. and Hines C. O. (1961) 'A unifying theory of high-latitude geophysical phenomena and geomagnetic storms' Can. J. Phys. 39 1433-1464

Baker K. B., Greenwald R. A., Ruohoniemi J. M., Dudeney J. R., Pinnock M., Mattin N. and Leonard J. M. (1989) 'PACE Polar Anglo-American Conjugate Experiment' EOS 70 785-799

Baker K. B. and Wing S. (1989) 'A new magnetic coordinate system for conjugate studies at high latitudes' J. Geophys. Res. 94 9139-9143

Balsley B. B. and Farley D. T. (1971) 'Radar studies of the equatorial electrojet at 3 frequencies' J. Geophys. Res. 76 8341-8351

Balsley B. B. and Farley D. T. (1973) 'Radar observations of two-dimensional turbulence in the equatorial electrojet' J. Geophys. Res. 78 7471-7479

Banks P. M., Doupnik J. R., Akasofu S.-I. (1973) 'Electric field observations by incoherent scatter radar in the auroral zone' J. Geophys. Res. 78 6607-6622

Banks P. M. and Kockarts G. (1973) 'Aeronomy' Academic Press

Baron M. J. and Wand R. H. (1983) 'F-region ion temperature enhancements resulting from Joule heating' J. Geophys. Res. 88 4114-4118

Berkner L. V. and Wells H. W. (1937) 'Abnormal ionization of the E-region of the ionosphere' TMAE 42 73-76

Beynon W. J. G. and Williams P. J. S. (1978) 'Incoherent scatter radio waves from the ionosphere' Rep. Prog. Phys. 41 909-947

Bleaney B. I. and Bleaney B. (1976) 'Electricity and magnetism' Oxford University Press

Booker H. G. (1956) 'A theory of scattering by non-isotropic irregularities with application to radar reflections from the aurora' J. Atmos. Terr. Phys. 8 204-221

Booker H. G., Gartlein C. W. and Nichols B. (1955) 'Interpretation of radio reflections from the aurora' J. Geophys. Res. 60 1-22

Bowles K. L. (1954) 'Doppler shifted radio echoes from aurora' J. Geophys. Res. 59 553-555

Bowles K. L., Balsley B. B. and Cohen R. (1963) 'Field aligned irregularities identified with acoustic plasma waves' J. Geophys. Res. 68 2485-2501

Bowles K. L. and Cohen R. (1962) 'A study of radio wave scattering from Sporadic E near the magnetic equator' Ionospheric Sporadic E (Pergamon Press ed. Smith and Matsushita) 51-77

Bowles K. L., Cohen R., Ochs G. R. and Balsley B. B. (1960) 'Radar echoes from field-aligned ionization above the magnetic equator and their resemblance to auroral echoes' J. Geophys. Res. 65 1853-1855

Breit G. and Tuve M. A. (1926) 'A test of the existence of the conducting layer' Phys. Rev. 28 554-575

Budden K. G. (1966) 'Radio waves in the ionosphere' Cambridge University Press

Buneman O. (1963) 'Excitation of field aligned sound waves by electron streams' Phys. Rev. Letts. 10 285-287

Burrage M. (1988) 'Radar studies of high latitude convection flows' Phd Thesis Leicester University

Caudal G., Alcayde D., Holt J., Beaujardiere O. De la, Lejeune G. (1984) 'Simultaneous measurements of the electrodynamic parameters of the auroral ionosphere by the EISCAT, Chatanika and Millstone Hill radars' Annales Geophys. 2 369-375

Chapman S. (1952) 'The geometry of radio echoes from aurora' J. Atmos. Terr. Phys. 3 1-29

Cohen R. and Bowles K. L. (1967) 'Secondary irregularities in the equatorial electrojet' J. Geophys. Res. 72 885-894

Currie B. W., Forsyth P. A. and Vawter F. E. (1953) 'Radio reflections from aurora' J. Geophys. Res. 58 179-200

Debye P. and Hückel E. (1923) 'Theory of electrolytes' Phys. Zeits. 24 185-206 and 305-325

Dungey J. W. (1961) 'Interplanetary magnetic fields and the auroral zones' Phys. Rev. Letts. 6 47-48

Dupree T. H. (1966) 'A perturbation theory for strong plasma turbulence' Phys. Fluids 9 1773-1782

Dyce R. (1955) 'Auroral echoes observed north of the auroral zone on 51.9 MC/SEC' J. Geophys. Res. 60 317-323

Ecklund W. L., Balsley B. B. and Carter D. A. (1977) 'A preliminary study of F region plasma drifts and E region irregularity drifts in the auroral zone' J. Geophys. Res. 82 195-197

Egan R. D. (1960) 'Anisotropic field-aligned ionization irregularities in the Ionosphere near the magnetic equator' J. Geophys. Res. 65 2343-2358

Evans J. (1969) 'Theory and practice of ionosphere study by Thomson scatter radar' Proc. IEEE 57 496-530

Farley D. T. (1963) 'A plasma instability resulting in field-aligned irregularities in the ionosphere' J. Geophys. Res. 68 6083-6097

Farley D. T. and Fejer B. G. (1975) 'The effect of the gradient drift term on Type 1 electrojet irregularities' J. Geophys. Res. 80 3087-3090

Farley D. and Providakes J. (1989) 'The variation with Te and Ti of the velocity of unstable ionospheric two-stream waves' J. Geophys. Res. 94 15415-15420

Fejer B. G. and Kelley M. C. (1980) 'Ionospheric irregularities' Rev. of Geophys. Sp. Phys. 18 401-454

Fejer B. G., Providakes J. F. and Farley D. T. (1984) 'Theory of plasma waves in the auroral E region' J. Geophys. Res. 89 7487-7494

Fejer B. G., Providakes J. F., Farley D. T. and Swartz W. E. (1986) 'Auroral E-region plasma waves and elevated electron temperatures' J. Geophys. Res. 91 13583-13592

Fejer B. G., Reed R. W., Farley D. T., Swartz W. E. and Kelley M. C. (1984) 'Ion cyclotron waves as a possible source of resonant auroral radar echoes' J. Geophys. Res. 89 187-194

Freeman M. P., Ruohoniemi J. M., Greenwald R. A. (1991) 'The determination of time-stationary 2-d convection patterns with single station radars' J. Geophys. Res. 96 15735-15749

Greenwald R. A. (1992) 'Global SuperDARN network will image high latitude convection' STEP Vol. 2 No. 9 2-6

Greenwald R. A., Baker K. B., Hutchins R. A. and Hanuise C. (1985) 'An HF phased-array radar for studying small-scale structures in the high-latitude ionosphere' Rad. Sci. 20 63-79

Greenwald R. A., Weiss W., Nielsen E. and Thomson N. R. (1978) 'STARE: A new radar auroral backscatter experiment in northern Scandinavia' Rad. Sci. 13 1021-1039

Haldoupis C., Prikryl P., Sofko G. J. and Koehler J. A. (1985) 'Evidence for 50MHz bistatic radio observations of electrostatic ion cyclotron waves in the auroral plasma' J. Geophys. Res. 90 10983-10990

Haldoupis C. and Schlegel K. (1990) 'Direct comparison of 1-m irregularity phase velocities and ion acoustic speeds in the auroral E-region ionosphere' J. Geophys. Res. 95 18989-19000

Haldoupis C., Schlegel K. and Nielsen E. (1992) 'On Type 3 auroral VHF coherent radar backscatter' J. Geophys. Res. 97 4109-4120

Haldoupis C. and Sofko G. J. (1979) 'VHF double-peak spectra in the morning sector of radio aurora' PSS 27 233-241

Haldoupis C., Sofko G. J., Koehler J. A. and Danskin D. W. (1991) 'A new look at Type 4 echoes of radar aurora' J. Geophys. Res. 96 11353-11362

Hanuise C. and Crochet M. (1981a) '5-50m wavelength plasma instabilities in the equatorial electrojet 1. Cross-field conditions' J. Geophys. Res. 86 3561-3566

Hanuise C. and Crochet M. (1981b) '5-50m wavelength plasma instabilities in the equatorial electrojet 2. Two-stream conditions' J. Geophys. Res. 86 3567-3572

Hanuise C., Villain J. P., Gresillon D., Cabrit B., Greenwald R. A. and Baker K. B. (1993) 'Interpretation of HF radar ionospheric Doppler spectra by collective wave scattering theory' Annales Geophys. 11 29-39

Harang L. and Landmark B. (1954) 'Radio echoes observed during aurorae and geomagnetic storms using 35 and 74 Mc/s waves simultaneously' J. Atmos. Terr. Phys. 4 322-338

Harang L. and Stoffregen W. (1938) 'Scattered reflections of radio waves from a height of more than 1000km' Nature 142 832-832

Heelis R. A. and Hanson W. B (1976) 'Ion convection velocity reversals in the dayside cleft' J. Geophys. Res. 81 3803-3809

Hedin A. E. (1987) 'MSIS-86 Thermospheric Model' J. Geophys. Res. 92 4649-4662

Heppner J. P. (1972) 'The Harang discontinuity in auroral belt ionospheric currents' Geofys. Publ. (Norway) 29 105-120

Holzhauer E. an Massig J. H. (1978) 'An analysis of optical mixing in plasma scattering experiments' Plasma Physics 20 867-877

Johnson R. M. and Virdi T. S. (1991) 'High latitude lower thermospheric neutral winds at EISCAT and Sondrestrom during LTCS 1' J. Geophys. Res. 96 1099-1116

Jones G. O. L., Winser K. J. and Williams P. J. S. (1986) 'Measurements of plasma velocity at different heights along a magnetic field line' J. Atmos. Terr. Phys.. 48 887-892

Kamide Y. and Baumjohann W. (1993) 'Magnetosphere - Ionosphere coupling' Springer-Verlag

Kelley M. C. (1989) 'The Earth's Ionosphere' Academic Press

Kofman W. and Nielsen E. (1990) 'STARE and EISCAT measurements: evidence for the limitation of STARE Doppler velocity observations by the ion acoustic velocity' J. Geophys. Res. 95 19131-19135

Kustov A., Uspensky M., Kangas J., Huuskonen A. and Nielsen E. (1989) 'On the threshold electric field for the ~1-m auroral irregularity appearance' J. Geophys. Res. 94 12043-12048

Leadabrand R. L., Schlobohm J. C. and Baron M. J. (1964) 'Simultaneous very high frequency and ultra high frequency observations of the aurora at Fraserburgh, Scotland' J. Geophys. Res. 70 4235-4284

Leonard J. M. (1991) 'The phenology of Antarctic F-region irregularities' Mphil Dissertation, British Antarctic Survey and Leicester University

Manson A. H., Meek C. E., Schminder R., Kürschner D., Clark R. R., Müller H. G., Vincent R. A., Phillips A., Fraser G. J., Singer W. and Kazimirovsky E. S. (1990) 'Tidal winds from the MLT global radar network during the first LTCS campaign - September 1987' J. Atmos. Terr. Phys. 52 175-183

Matsushita S. (1951) 'Intense Es ionization near the magnetic equator' JGGE 3 44-46

Mattin (1994) Phd thesis in preparation

Mattin N. and Jones T. B. (1986) 'SABRE observations of E-region vertical velocity structures' J. Atmos. Terr. Phys. 48 625-632

Mattin N. and Jones T. B. (1987) 'Propagation angle dependence of radar auroral E-region irregularities' J. Atmos. Terr. Phys. 49 115-121

McCrea I. W., Schlegel K., Nygrén T. and Jones T. B. (1991) 'COSCAT, a new auroral radar facility on 930 MHz - system description and first results' Annales Geophys. 9 461-469

McNamara A. G. (1955) 'Double-Doppler radar investigations of aurora' J. Geophys. Res. 60 257-269

Moorcroft D. R. (1987) 'Estimates of absolute scattering coefficients of radar aurora' J. Geophys. Res. 92 8723-8732

Moorcroft D. R. and Tsunoda R. T. (1978) 'Rapid scan Doppler velocity maps of the UHF diffuse radar aurora' J. Geophys. Res. 83 1482-1492

Moore R. K. (1951) 'A VHF propagation phenomena associated with aurora' J. Geophys. Res. 56 97-106

Moore R. K. (1952) 'Theory of radio scattering from the aurora' IRE Trans. PG AP-3 217-229 joint URSI-IRE meeting

Nielsen E., Güttler W., Thomas E. C., Stewart C. P., Jones T. B. and Hedberg A. (1983) 'SABRE : A new radar auroral backscatter experiment' Nature 304 712-714

Nielsen E., Haldoupis C. I., Fejer B. G. and Ierkic H. M. (1984) 'Dependence of auroral power spectra variations upon electron drift velocity in the eastward electrojet' J. Geophys. Res. 89 253-260

Nielsen E. and Schlegel K. (1983) 'A first comparison of STARE and EISCAT electron drift velocity measurements' J. Geophys. Res. 88 5745-5750

Nielsen E. and Schlegel K. (1985) 'Coherent radar Doppler measurements and their relationship to the ionospheric electron drift velocity' J. Geophys. Res. 90 3498-3504

Nishida A. (1982) 'Magnetospheric plasma physics' Center for Academic Publications Japan

Oksman J., Uspensky M. V., Starkov G. V., Stepanov G. S. and Vallinkoski M. (1986) 'The mean fractional electron density fluctuation amplitude derived from auroral backscatter data' J. Atmos. Terr. Phys. 48 107-113

Ossakow S. L. and Chaturvedi P. K. (1979) 'Current convective instability in the diffuse aurora' GRL 6 323-334

Pfaff R. F., Sahr J., Providakes J. F., Swartz W. E., Farley D. T., Kintner P. M., Häggström I., Hedberg A., Opgenoorth H., Holmgren G., McNamara A., Wallis D., Whalen B., Yau A., Watanabe S., Creutzberg F., Williams P., Nielsen E., Schlegel K., Robinson T. R. (1992) 'The E-region rocket/radar instability study (ERRRIS) scientific objectives and campaign overview' J. Atmos. Terr. Phys. 54 779-808

Prikryl P. and Cogger L. L. (1992) 'Statistical analysis of the spatial relationship between the radio and optical aurora. Further evidence for refraction' Rad. Sci. 27 469-479

Prikryl P., Koehler J. A., Sofko G. J., McEwen D. J. and Steele D. (1987) 'Ionospheric ion cyclotron wave generation inferred from coordinated Doppler radar, optical and magnetic observations' J. Geophys. Res. 92 3315-3331

Ratcliffe J. A. (1972) 'An introduction to the ionosphere and magnetosphere' Cambridge University Press

Rishbeth H. (1988) 'Basic physics of the ionosphere: a tutorial review' Journal of the institution of electronic and radio engineers 58 S207-S223

Rishbeth H. and Garriot O. K. (1969) 'Introduction to ionospheric physics' Academic Press

Rishbeth H. and Williams P. J. S. (1985) 'The EISCAT ionospheric radar: the system and its early results' QJR astr. soc. 26 478-512

Robinson T. R. (1993) 'Simulation of convection flow estimation errors in VHF bistatic auroral radar systems' Annales Geophys. 11 1033-1050

Robinson T. R. (1986) 'Towards a self-consistent non-linear theory of radar auroral backscatter' J. Atmos. Terr. Phys. 48 417-422

Robinson T. R. and Honary F. (1990) 'A resonance broadening kinetic theory of the modified two-stream instability: Implications for radar auroral backscatter experiments' J. Geophys. Res. 95 1073-1085

Salah J. F., Johnson R. M. and Tepley C. A. (1991) 'Coordinated incoherent scatter radar observations of the semidiurnal tide in the lower thermosphere' J. Geophys. Res. 96 1071-1080

Schlegel K. (1983) 'Interpretation of auroral radar experiments using a kinetic theory of the two-stream instability' Rad. Sci. 18 108-118

Schlegel K. and St-Maurice J. P. (1981) 'Anomalous heating of the polar E region by unstable plasma waves. 1. Observations' J. Geophys. Res. 86 1447-1452

Schlegel K., Thomas E. C. and Ridge D. (1986) 'A statistical study of auroral radar spectra obtained with SABRE' J. Geophys. Res. 91 13483-13492

Seyler C. F. and Providakes J. (1987) 'Particle and fluid simulations of resistive current-driven electrostatic ion cyclotron waves' Phys. Fluids 30 3113-3128

St-Maurice J.-P. and Hanson W. B. (1982) 'Ion frictional heating at high latitudes and its possible use for an in situ determination of neutral thermospheric winds and temperatures' J. Geophys. Res. 87 7580-7602

St.-Maurice J.-P. and Schunk R. W. (1977) 'Ion velocity distributions in the high latitude ionosphere' Planet. Space Sci. 25 243-260

St.-Maurice J.-P. and Schunk R. W. (1979) 'Auroral ion velocity distributions for a polarisation collision model' Rev. Geophys. Space Phys. 17 99-134

Sudan R. N. (1983) 'Unified theory of Type (I) and Type (II) irregularities in the equatorial electrojet' J. Geophys. Res. 88 4853-4860

Sudan R. N., Akinrimisi J. and Farley D. T. (1973) 'Generation of small-scale irregularities in the equatorial electrojet' J. Geophys. Res. 78 240-248

Tetenbaum D., Avery S. K. and Riddle A. C. (1986) 'Observations of mean winds and tides in the upper mesosphere during 1980-1984 using the Poker Flat, Alaska, MST radar as a meteor radar' J. Geophys. Res. 91 14539-14555

Tsunoda R. T. (1975) 'Electric field measurements above a radar scattering volume producing 'diffuse' auroral echoes' J. Geophys. Res. 80 4297-4306

Tsunoda R. T., Presnell R. I., Kamide Y. and Akasofu S.-I. (1976) 'Relationship of radar aurora, visual aurora and auroral electrojets in the evening sector' J. Geophys. Res. 81 6005-6015

Villain J. P., Caudal G. and Hanuise C. (1985) 'A Safari-EISCAT comparison between the velocity of F-region small-scale irregularities and the ion drift' J. Geophys. Res. 90 8433-8443

Villain J. P., Greenwald R. A., Baker K. B. and Ruohoniemi J. M. (1987) 'HF radar observations of E-region plasma irregularities produced by oblique electron streaming' J. Geophys. Res. 92 12327-12342

Villain J. P., Greenwald R. A. and Vickrey J. F. (1984) 'HF ray tracing at high latitudes using measured meridional electron density distributions' Rad. Sci. 19 359-374

Villain J. P., Hanuise C., Greenwald R. A., Baker K. B. and Ruohoniemi J. M. (1990) 'Obliquely propagating ion acoustic waves in the auroral E-region: Further evidence of irregularity production by field-aligned electron streaming' J. Geophys. Res. 95 7833-7846

Waldock J. A., Jones T. B. and Nielsen E. (1985) 'Statistics of 1-m wavelength plasma irregularities and convection in the auroral E region' Rad. Sci. 20 709-717

Walker A. D. M., Greenwald R. A., Stuart W. F. and Green C. A. (1979) 'STARE auroral radar observations of Pc5 geomagnetic pulsations' J. Geophys. Res. 84 3373-3388

Weinstock J. and Sleeper A. M. (1972) 'Non-linear saturation of Type (I) irregularities in the equatorial electrojet' J. Geophys. Res. 77 3621-3629

Whitehead J. D. (1983) 'On reducing the inherent noise in the double-pulse Doppler technique' Rad. Sci. 18 93-94

Williams P. J. S., Jones B. and Jones G. O. L. (1992) 'The measured relationship between electric field strength and electron temperature in the auroral E-region' J. Atmos. Terr. Phys. 54 741-748

Zarnitskiy Yu F. (1989) 'The origin of Type (IV) auroral radio reflections' Geomagn. Aeron. 29 142-144